New windows onto the stellar population at the Galactic Centre: Multi-wavelength and time-domain studies

Aurelia Teresa Gallego Calvente

Universidad de Granada
Instituto de Astrofísica de Andalucía
Consejo Superior de Investigaciones Científicas

New windows onto the stellar population at the Galactic Centre: multi–wavelength and time-domain studies

Universidad de Granada

Programa de Doctorado en Física y Matemáticas

Tesis Doctoral

Memoria presentada al Departamento de Física Teórica y del Cosmos de la Universidad de Granada para optar al grado de **Doctor en Astrofísica**

por

Aurelia Teresa Gallego Calvente

Director

Dr. Rainer Schödel

06 de Mayo de 2021
Granada, España

Esta tesis ha sido aprobada por el director de la misma:

Dr. R. Schödel

del Instituto de Astrofísica de Andalucía (IAA-CSIC).

This thesis has been approved by the supervisor:

Dr. R. Schödel

from the Institute of Astrophysics of Andalusia (IAA-CSIC).

Declaración

La doctoranda **Aurelia Teresa Gallego Calvente** y el director de la tesis **Dr. Rainer Schödel**, garantizamos, al firmar esta tesis doctoral, que el trabajo ha sido realizado por la doctoranda bajo la dirección del director de la tesis y, hasta donde nuestro conocimiento alcanza, en la realización del trabajo se han respetado los derechos de otros autores a ser citados cuando se han utilizado sus resultados o publicaciones.

*The doctoral candidate **Aurelia Teresa Gallego Calvente** and the thesis supervisor **Dr. Rainer Schödel** guarantee, by signing this doctoral thesis, that the work has been done by the doctoral candidate under the direction of the thesis supervisor and, as far as our knowledge reaches, in the performance of the work, the rights of other authors to be cited (when their results or publications have been used) have been respected.*

Aurelia Teresa Gallego Calvente
La doctoranda / *The doctoral candidate*

Dr. Rainer Schödel
El director / *The thesis supervisor*

Granada, 06 de Mayo de 2021.

Prólogo

Figure 1: Quintuplet and Arches clusters in the infrared. Images credits: ESA/NASA Hubble Space Telescope.

EL Universo sólo tiene tres respuestas:

1. Sí.

2. Todavía no.

3. Tengo algo mejor para ti.

Agradecimientos

Esta aventura de querer ser astrónoma se asentó en mis pensamientos allá por tercero de carrera de Ciencias Físicas. Mucho antes, las historias que de las estrellas le contaba el abuelo del que, por aquel entonces, era mi novio, detonaron este impulso. Treinta años después, finaliza este camino. En todos y cada uno de los pasos que he dado para llegar hasta aquí, me siento agradecida infinitamente por todas las personas que he conocido, que me han apoyado, y de todos los sitios en los que he trabajado agradezco lo mucho aprendido. Desde que fuera animadora científica en el Parque de las Ciencias de Granada donde, con mi compañero Roberto, hacíamos unas Noches de Observación exquisitas, hablando sobre todo de nuestra maravillosa Luna, recorriendo cada noche por la línea del terminador sus tranquilos y serenos mares, aunque con alguna crisis, deteniéndonos en sus muchos cráteres, llegando a los Montes Alpinos, bañándonos en el mar de las lluvias y, finalmente, descansando en la bahía del arcoiris, "porque siempre detrás de la lluvia viene el arcoiris..."; como profesora en el Instituto público de Educación Secundaria Sáinz de Andino, de la provincia de Cádiz; empezando a formarme profesionalmente en el Instituto de Radioastronomía Milimétrica (IRAM) de Granada; trabajando para y aprendiendo del excelente profesional y mejor persona Lucas Lara Garrido (donde quiera que estés, aquí mi pequeño homenaje); divulgando Astronomía entre escolares, desde niños de guardería hasta niveles de Bachillerato, en el *Observatori Astronòmic* de la *Universitat de València* donde mis extraordinarios compañeros, Miquel, Lupe, Sofía, Marianna, Lara, y muchos otros nos acogieron con los brazos abiertos hasta formar una pequeña gran familia; y, finalmente, en el Instituto de Astrofísica de Andalucía (IAA-CSIC) que ya es mi segunda casa.

Me gustaría escribir un agradecimiento especial a mi director de tesis, Rainer Schödel, por darme la oportunidad de cumplir este sueño, confiar en mi, por su paciencia infinita, su comprensión, compartir su enorme talento (no en vano es una de las personas más inteligentes que conozco), por corregir mis errores y ser como es, una excelente persona.

No tengo palabras para dar las gracias a mi gran amiga, compañera de risas, llantos, debates científicos, de conversaciones vitales, mi colega y `mentora` María Passas Varo porque sin su apoyo incondicional y sus ánimos constantes no habría llegado hasta aquí. ¡MIL GRACIAS MARÍA! ¿Qué vamos a terminar hoy?

A mi pareja, Francisco Peregrín González, que contrariamente a lo que suele suceder, ha hecho posible que este último tramo de la tesis haya sido uno de los

momentos más felices de mi vida. Y los que nos quedan. Los iremos cultivando poco a poco.

No quiero olvidarme de todos los miembros, pasados y presentes, de mi Grupo de Investigación del Centro Galáctico, ni del director del Instituto de Astrofísica de Andalucía, Antxón Alberdi Odriozola. Gracias por vuestra enorme ayuda, ánimos constantes, contínuos consejos, supervisión y por estar siempre ahí cuando lo he necesitado.

También estoy muy agradecida a todos mis compañeros del IAA, desde el personal de limpieza, mantenimiento, administración, Centro de Cálculo, pre-docs, post-docs, a mis compañeros de despacho y, a veces, también de fatigas, y a todo el personal científico y técnico que siempre me ha ayudado.

Por supuesto, una parte fundamental de este logro se lo debo a mis padres, Jesús y Rosa, por motivarme a llegar más y más alto, enseñarme la importancia del trabajo bien hecho, y darme la mejor educación posible. Seguro que ven en mí algo que no pudieron lograr y que ahora a través mío por fin han conseguido. Agradezco a mis hermanas, Esperanza y Rosa María, aguantar mis locuras y hacerme en definitiva mucho más fuerte.

Finalmente, a quien estoy más agradecida es a esas dos personas que me ayudan a recordar mi verdadera pasión, quienes me dan fuerza para lograr todo lo que me proponga, a mi bonita familia de todos los días, a mis hijas, Rita y Sofía, a ellas les dedico esta tesis.

Aurelia Teresa Gallego Calvente
Granada, Marzo 2021.

ACKNOWLEDGMENTS
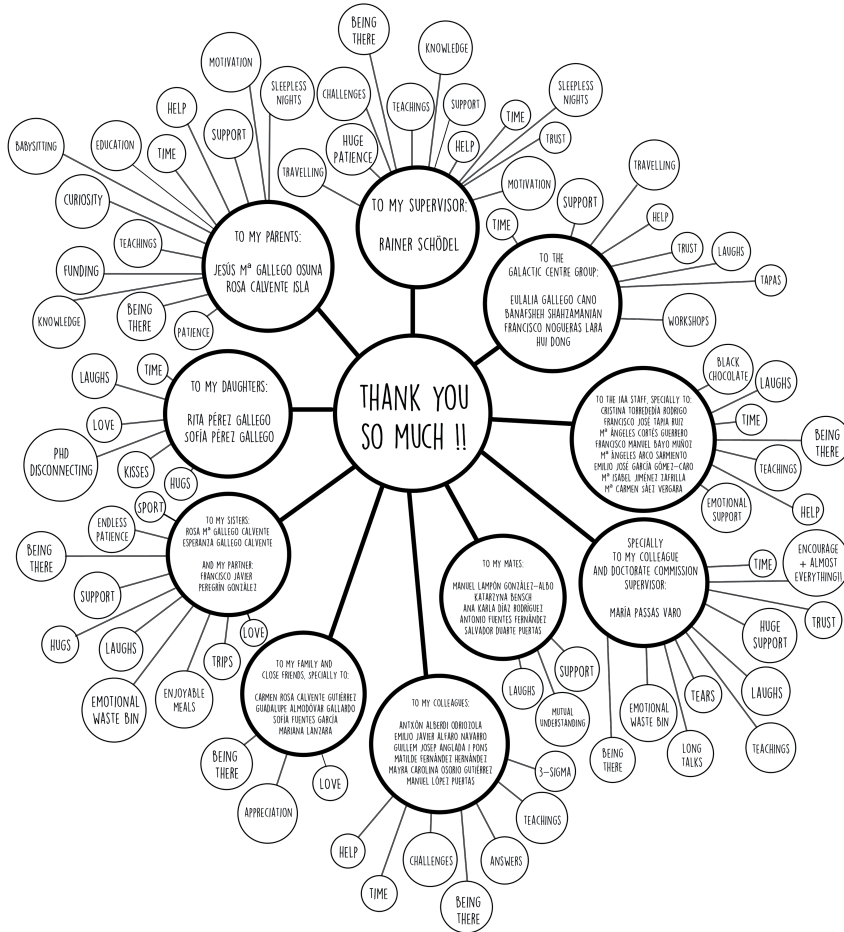
Resumen

El centro de nuestra galaxia, la Vía Láctea, será siempre de nuestro interés debido a que su proximidad lo convierte en un laboratorio ideal para poder estudiar fenómenos que luego se pueden extrapolar a otras galaxias. Sin embargo, el estar abarrotado de estrellas hace muy difícil su completa observación y, además, el medio interestelar entre la Tierra y el centro Galáctico es opaco para algunas longitudes de onda, como por ejemplo para la luz visible. Por ello, es cada vez más relevante estudiar el Universo a diferentes frecuencias y en diferentes épocas para poner de manifiesto todos sus aspectos.

De entre todos los distintos tipos de estrellas que conocemos, las *estrellas masivas* son de especial interés debido a varios hechos fundamentales. En primer lugar, su alta masa (comúnmente aceptada mayor a ocho veces la masa de nuestro Sol), que hace que tengan una temperatura central muy elevada y, por lo tanto, una gran luminosidad, da lugar a que estas estrellas evolucionen más rápidamente y vivan menos tiempo que las estrellas de menor masa. Excitan y enriquecen químicamente el medio interestelar en el que se encuentran a través de una intensa radiación ionizante, fuertes vientos y, en particular, al morir en una explosión que se determina como *supernova*. Además, dan origen a objetos de alta energía como estrellas de neutrones o agujeros negros.

Por otro lado, y precisamente por su elevada masa, son raras y difíciles de observar ya que cuanto más masiva es una estrella en menos cantidad se encuentra y, al formarse en las regiones más densas de las nubes moleculares, se hallan envueltas por una gran cantidad de polvo y gas molecular durante las fases iniciales de su vida hasta que llegan a la secuencia principal. A través de estudios observacionales se ha demostrado que la tasa de formación estelar por intervalo de masa depende fundamentalmente de la masa. Esta dependencia se conoce como *función inicial de masa* (IMF, por sus siglas en inglés). Pues bien, para masas mayores a una masa solar, la IMF puede aproximarse a una ley de potencias con la masa como base y el exponente, para estrellas masivas y de masa intermedia, igual a -2.35 (IMF de Salpeter). En entornos extremos como es el caso del centro Galáctico, con fuerzas de marea muy intensas, un campo magnético tremendo, temperaturas muy elevadas, enormes turbulencias en el medio interestelar, una densidad estelar

muy extrema y una radiación ultravioleta importante, este exponente puede pasar a un valor diferente, como el valor de -1.8 encontrado observacionalmente para el cúmulo de Arches (Hosek et al., 2019), lo que puede indicar que en este entorno se forman relativamente más estrellas masivas que en la vecindad solar.

Otra característica notable que presentan es su alta fracción de multiplicidad, es decir, suelen formar sistemas múltiples (alrededor del 91% de acuerdo con Sana et al. 2014), lo que debe también tenerse en cuenta al analizar su evolución y en el extremo final de la función inicial de masa.

Para estudiarlas, el centro Galáctico es un lugar excepcional por ser el único núcleo galáctico y el entorno de condiciones físicas más extremas que podemos examinar a escalas de miliparsecs.

Así pues, considerando además que las nubes moleculares en las que se forman se encuentran a distancias mayores a 1 Kpc de nosotros, para estudiar las estrellas masivas necesitaremos instrumentos con la mayor sensibilidad y la mejor resolución posibles.

El objetivo de esta tesis es el estudio de las estrellas masivas pertenecientes a dos de los cúmulos más emblemáticos del centro Galáctico, los cúmulos de Arches y Quintuplet, ambos situados a unos 30 parsecs en proyección de Sagittarius A*, el agujero negro central de la Vía Láctea, utilizando técnicas de muy alta resolución angular radio interferométricas. Estas técnicas nos permiten la observación de objetos lejanos separados por una distancia angular muy pequeña, sintetizando una apertura equivalente a la distancia de separación de pares de antenas, apertura que no sería posible conseguir con un único radio telescopio.

Debido a que la extinción interestelar en esta región es muy elevada, los estudios observacionales de estos dos cúmulos se han visto limitados fundamentalmente a observaciones en el infrarrojo cercano, con espectroscopía y fotometría, por ser el rango óptico prácticamente inaccesible y estar el infrarrojo medio limitado por la resolución angular y/o la sensibilidad de los instrumentos en un enclave muy poblado de estrellas. Dada la baja estadística de observaciones en radio de los vientos ionizados de las estrellas masivas y la existencia de ellas en los cúmulos de Arches y Quintuplet, este trabajo es un nuevo paso hacia la comprensión de este tipo de estrellas y de los cúmulos que las contienen.

Todos los estudios que aquí se presentan se han realizado gracias a la utilización del radio interferómetro *Karl G. Janksy Very Large Array* (JVLA) operado por el *Na-*

tional Radio Astronomy Observatory (NRAO)[1]. En este trabajo se ha obtenido: a) un nuevo censo, en ambos cúmulos, del número de estrellas masivas observadas en longitudes de onda de radio centimétricas, b) los flujos y posiciones de las mismas, c) las tasas de pérdida de masa estimadas, d) una valoración de su posible multiplicidad en base al índice espectral calculado, e) una evaluación de la variabilidad, y finalmente, f) una estimación, entre unos ciertos límites, de la edad y/o masa de los cúmulos, así como de la función inicial de masa en base, precisamente, al número de radio fuentes detectadas.

Esta tesis esta compuesta de seis capítulos. En el primero de ellos se da una breve introducción sobre la ciencia que hay en la misma. En el segundo capítulo se exponen los principios de la radio interferometría, haciendo hincapié en los aspectos fundamentales que han dado lugar a este trabajo. En los capítulos tres y cuatro se presentan los principales tópicos de investigación de esta tesis. Éstos incluyen los datos, el análisis y los resultados descritos en una publicación arbitrada y en una que será enviada de forma inminente. Finalmente, los capítulos cinco y seis presentan las conclusiones generales y las futuras líneas de investigación de esta tesis.

---

[1]The NRAO is a facility of the National Science Foundation (NSF) operated under cooperative agreement by Associated Universities, Inc.

Summary

The centre of our galaxy, the Milky Way, will always be of interest to us since its proximity makes it an ideal laboratory to study phenomena that can be later extrapolated to other galaxies. However, the overcrowded state of stars makes its complete observation very difficult and, in addition, the interstellar medium between the Earth and the Galactic centre is opaque for some wavelengths, such as for visible light. Therefore, it is increasingly relevant to study the Universe at different frequencies and at several times to reveal all its aspects.

Of all the different types of stars known, *massive stars* are of special interest because of a number of fundamental facts. In the first place, their high mass (commonly accepted greater than eight times the mass of our Sun), which makes them have a very high central temperature and, consequently, great luminosity, gives rise to these stars to evolve more rapidly and live shorter than lower mass stars. They stirring gand enriching the interstellar medium in which they are found through intense ionising radiation, strong winds and, in particular, by dying in an explosion that is determined to be a supernova. Furthermore, they give rise to high-energy objects such as neutron stars or black holes.

On the other hand, and precisely because of their high mass, they are rare and difficult to observe since the more massive a star is, the less quantity it is and, as it forms in the densest regions of molecular clouds, it is surrounded by a large amount of dust and molecular gas during the initial phases of their life until they reach the main sequence. Through observational studies it has been shown that the star formation rate per mass interval is fundamentally dependent on mass. This dependency is known as the *initial mass function* (IMF). So, for masses greater than a solar mass, the IMF can be approximated to a power law with the mass as the base and the exponent, for massive stars and intermediate mass, equal to -2.35 (Salpeter's IMF). In extreme environments such as the Galactic centre, with very intense tidal forces, a tremendous magnetic field, very high temperatures, enormous turbulence in the interstellar medium, a stellar density very extreme and significant ultraviolet radiation, this exponent may change to a different value, such as the value -1.8 found observationally for the Arches cluster (Hosek et al., 2019), which may indicate that relatively more massive stars are formed in this environment than in the solar neighbourhood.

Another notable characteristic that they present is their high multiplicity fraction, that is in other words, they tend to form multiple systems (about 91% according to Sana et al. 2014), which must also be taken into account when analysing its evolution and in the final end of the IMF.

The Galactic centre is an exceptional place to study them because it is the only galactic nucleus and the environment fo the most extreme physical conditions that we can examine at milliparsec scales.

Thus, considering also that the molecular clouds in which they are formed are at distances greater than 1 kpc from us, to study massive stars we will need instruments with the highest possible sensitivity and angular resolution.

The objective of this thesis is the study of the massive stars belonging to two of the most emblematic clusters of the Galactic centre, the Arches and Quintuplet clusters, both located about 30 parsecs in projection of Sagittarius A*, the central black hole of the Milky Way, using very high angular resolution radio interferometric techniques. These techniques allow us to observe distant objects separated by a very small angular distance, synthesising an aperture equivalent to the distance between pairs of antennas, an aperture that would not be possible to achieve with a single dish radio telescope.

Due to the very high extinction in this region, the observational studies of these two clusters have been mainly limited to observations in the near infrared, with spectroscopy and photometry, as the optical range is practically inaccesible and the mid-infrared is limited due to the angular resolution and/or the sensitivity of the instruments in an enclave heavily populated with stars. Given the low statistics of radio observations of the ionised winds of massive stars and the existence of them in the Arches and Quintuplet clusters, this work is a new step towards understanding this type of stars and the clusters that contain them.

All the studies presented here have been carried out using the *Karl G. Janksy Very Large Array* (JVLA) radio interferometer operated by the *National Radio Astronomy Observatory* (NRAO)[2]. In this work, we have obtained: a) a new census, in both clusters, of the number of massive stars observed in centimetre radio wavelengths, b) their fluxes and positions, c) estimated mass-loss rates, d) an assessment of their possible multiplicity based on the calculated spectral index, e) an assessment of variability, and finally, f) an estimate, within certain limits, of the age and/or mass of the clusters, as well as the IMF based, precisely, on the number of radio sources detected.

---

[2]The NRAO is a facility of the National Science Foundation (NSF) operated under cooperative agreement by Associated Universities, Inc.

This thesis is composed of six chapters. In the first one, a brief introduction is given about the science that is in it. In the second chapter, the principles of radio interferometry are exposed, emphasising the fundamental aspects that have given rise to this work. In chapters three and four, the main research topics of this thesis are presented. These include the data, analysis, and results described in a peer-reviewed publication and in one to be submitted imminently. Finally, chapters five and six present the general conclusions and future lines of research of this thesis.

Contents

List of Figures

List of Tables

GLOSSARY

- **ASIAA:** Academia Sinica Institute of Astronomy and Astrophysics

- **ASTRON:** Netherlands Institute for Radio Astronomy

- **CASA:** Common Astronomy Software Applications package

- **CASS:** CSIRO division for Astronomy and Space Science

- **CSIRO:** Commonwealth Scientific and Industrial Research Organisation

- **CWB:** Colliding wind binary

- **EM:** Electromagnetic

- **ESO:** European Southern Observatory

- **FoV:** Field of view

- **FWHM:** Full Width at Half Maximum

- **GC:** Galactic center. This term refers to the center of the Milky Way.

- **GTC/CIRCE:** Gran Telescopio CANARIAS / Canarias InfraRed Camera Experiment

- **HAWK-I:** High Acuity Wide field K-band Imager / ESO Paranal instrument

- **HST:** Hubble Space Telescope

- **HST/NICMOS:** Hubble Space Telescope / Near Infrared Camera and Multi-Object Spectrometer

- **HST/WFC3:** Hubble Space Telescope / Wide Field Camera 3

- **IMF:** Initial mass function

- **ISM:** Interstellar medium

- **JVLA:** Karl Guthe Jansky Very Large Array

- **KMOS:** K-band Multi Object Spectrograph

- **NACO:** Nasmyth Adaptive Optics System (NAOS) Near-Infrared Imager and Spectrograph (CONICA) / ESO VLT instrument

- **NAOJ:** National Astronomical Observatory of Japan

- **NCP:** North Celestial Pole

- **NICMOS:** Near Infrared Camera and Multi-Object Spectrometer

- **NIR:** Near-infrared

- **NOT:** Nordic Optical Telescope

- **NRAO:** National Radio Astronomy Observatory

- **PMS:** Post Main Sequence

- **PSF:** Point Spread Function

- **RLF:** Radio Luminosity Function

- **RMS:** Root Mean Square

- **Sgr A*:** Sagittarius A*

- **SF:** Star Formation

- **SINFONI:** Spectrograph for INtegral Field Observations in the Near Infrared

- **SKA-MID:** Square Kilometre Array at mid-frequency

- **S/N:** Signal-to-noise ratio

- **VLA:** Very Large Array

- **VLT:** Very Large Telescope

- **VLT/KMOS:** Very Large Telescope / K-band Multi Object Spectrograph

- **VLT/SINFONI:** Very Large Telescope / Spectrograph for INtegral Field Observations in the Near Infrared

- **WCR:** Wind-wind collision region

- **WFC3:** Wide Field Camera 3

- **YSO:** Young Stellar Object

1

Introduction

Stars release energy not only in the form of electromagnetic radiation but also as particles. This flow of particles is named *stellar wind*. The two most important features of a stellar wind from an observational standpoint are the amount of mass that the star loses per unit of time, that is, the *mass-loss rate*, and the velocity of the stellar wind at a large distance from the star, known as *terminal velocity*.

One could say that the study of stellar winds started when the first astronomer famous for his false nose made of gold and silver (or more possibly of brass), discovered the so-called "Tycho" supernova in 1572. After having passed through several milestones, like the detection of the solar wind by the Mariner 2 probe in 1967, or the development of a radiation-driven wind model by Lucy & Solomon in 1970, currently one of the frontiers of stellar wind research is understanding the mass-loss mechanisms and wind properties of massive stars.

We know that the mass of a star is the most relevant parameter in its life. In fact, the initial mass of a star determines its energy output as a function of time, its evolution and final fate.

1.1. Massive stars

Typically, a star is defined as a *massive star* when it has at least eight times the mass of the Sun ($M_\star > 8\,M_\odot$). Such stars end their lives as supernovae. Stars with masses

1

1

between two and eight solar masses ($2\,M_\odot \leq M_\star \leq 8\,M_\odot$) are considered stars of intermediate-mass. If their mass lies in the range one half and two ($0.5\,M_\odot \leq M_\star \leq 2\,M_\odot$), stars are classified as low-mass stars and, finally, stars with masses between eight hundredths and one half ($0.08\,M_\odot \leq M_\star \leq 0.5\,M_\odot$) are placed in the category of very low-mass stars. The lower limit $0.08\,M_\odot$ is the minimum mass required to sustain nuclear fusion, that is, to reach the H-burning state. This implies that these stars will become true main sequence stars, while those below that limit (but more massive than thirteen Jupiter masses) will burn only deuterium for a while and will be called *brown dwarfs*.

Stars are usually classified according to their spectral characteristics. The modern classification system is the so-called MKK system (from the authors' initials, William Wilson Morgan, Philip C. Keenan, and Edith Kellman). Table 1.1 lists some of the defining characteristics for various spectral types. There can be seen that this classification is related to the observed surface temperature where the hottest most massive stars are type O, being the next class type B, and so on. A star classified as "OB" would be a star where the quality of the available spectrum is such that the two respective sub-types cannot be differentiated. Table 1.2 shows the luminosity classes. The star's observed properties, the absolute magnitude and/or the luminosity and the spectral type and/or the temperature, are frequently recorded in the Hertzsprung-Russell (HR) diagram (see Figure 1.1) representing a major step for astronomers towards an understanding of stellar evolution.

Stars are born when a cold, dense, molecular cloud starts to collapse due to its own gravity, breaking into small clumps. Each clump begins to attract the surrounded material. Finally a core of gas is formed, becoming a proto-star which accretes material at the same time as it reduces its size and progresses towards the *Main Sequence* (MS). There, the proto-star will begin to burn hydrogen.

Observational studies have shown that the fragmentation of molecular clouds results in far more low mass stars being formed than high mass ones. This result indicates that the number of stars that form per mass interval strongly depends on the mass, as shown in Figure 1.2. This dependence is known as the *initial mass function* (IMF). Although the IMF may depend on the local environment, most observations have shown that its shape at masses above one solar mass can be very well approximated by a power law that is approximately dN/dm $\sim$ m$^{-2.35}$ (Salpeter IMF; see Figure 1.3). Even in regions with a probably top-heavy mass function (such as the Galactic centre, Hußmann et al. 2012; Hosek et al. 2019; Lu et al. 2013; Bartko et al. 2010) this function is still steep (e.g. dN/dm $\sim$ m$^{-1.8}$, Hosek et al. 2019). This results in few massive stars being born.

If we continue focusing our attention just on massive stars, we can see that they are localised in the upper left region of the HR diagram. They are characterised by a high temperature that leads to a high luminosity, and as a consequence they have a very short life. They undergo a very fast evolution, being their lives of the order

Table 1.1: Harvard spectral classification.

Spectral type	Characteristics
O	Hottest blue-white stars with few lines
	Strong He II absorption (sometimes emission) lines.
	He I absorption lines becoming stronger.
B	Hot blue-white
	He I absorption lines strongest at B2.
	H I (Balmer) absorption lines becoming stronger.
A	White
	Balmer absorption lines strongest at A0, becoming weaker later.
	Ca II absorption lines becoming stronger.
F	Yellow-white
	Ca II lines continue to strengthen as Balmer lines continue to weaken.
	Neutral metal absorption lines (Fe I, Cr I).
G	Yellow
	Solar-type spectra.
	Ca II lines continue becoming stronger.
	Fe I, other neutral metal lines becoming stronger.
K	Cool orange
	Ca II H and K lines strongest at K0, becoming weaker later.
	Spectra dominated by metal absorption lines.
M	Cool red
	Spectra dominated by molecular absorption bands,
	especially titanium oxide (TiO) and vanadium oxide (VO).
	Neutral metal absorption lines remain strong.
L	Very cool, dark red
	Stronger in infrared than visible.
	Strong molecular absorption bands of metal hydrides (CrH, FeH), water
	(H_2O), carbon monoxide (CO), and alkali metals (Na, K, Rb, Cs).
	TiO and VO are weakening.
T	Coolest, Infrared
	Strong methane (CH_4) bands but weakening CO bands.

Note. Based on Table 1 by Carroll & Ostlie (2014) from Chapter 8, *"The Classification of Stellar Spectra"*, listing some of the defining criteria for various spectral types. The term *metal* is used to indicate any element heavier than helium.

of some millions of years instead of the billions that stars similar to our Sun live. They are of vital importance to understanding star formation and galaxy evolution because of their key role in stirring and enriching the ISM through intense ionising radiation, stellar winds, and supernovae, and also as source of high-energy objects in a galaxy such as neutron stars or black holes.

Massive stars are commonly classified in the following types:

1

Table 1.2: MKK, also known as Yerkes, luminosity classes.

Luminosity class	Type of star
0 or Ia+	Hypergiants or extremely luminous supergiants
Ia	Luminous supergiants
Iab	Intermediate-size luminous supergiants
Ib	Less luminous supergiants
II	Bright giants
III	Normal giants
IV	Subgiants
V	Main-sequence stars (dwarfs)
sd (prefix) or VI	Subdwarfs
D (prefix) or VII	White dwarfs

Note. Based on Table 3 by Carroll & Ostlie (2014) from Chapter 8, *"The Classification of Stellar Spectra"*, listing the luminosity classes.

- OB   They are of spectral type O or B. For O-stars, there are detailed spectral sub-types, depending on their mass and evolutionary state (see Table A.1 in the Appendix).

- RSG   Red supergiants are very red massive stars with relatively narrow absorption lines in their spectra. They are cool, post-main-sequence (PMS) stars.

- LBV   Luminous blue variables are clearly evolved, PMS stars. They present a huge variability. Their visual spectra show a extremely strong emission lines of the prototype star P Cygni.

- WR   Wolf-Rayet stars exhibit emission lines mainly of He. There are two main sub-types:

    - *WN sub-type*, with strong lines of He and nitrogen (N). These, in turn, could be of early type (WNE) or of late type (WNL). An "h" suffix is used to indicate emission lines due to H.

    - *WC sub-type*, with lines of He, carbon (C) and oxygen (O). WCE indicating early type and WCL for late type can also be found.

The upper region of the HR diagram also contains blue supergiant stars (BSG) which are hot, luminous PMS stars, often referred to as OB supergiants.

Considering different ranges of masses for massive stars, next we show a general evolutionary scheme for them, ending all the paths in a supernova (SN) explosion:
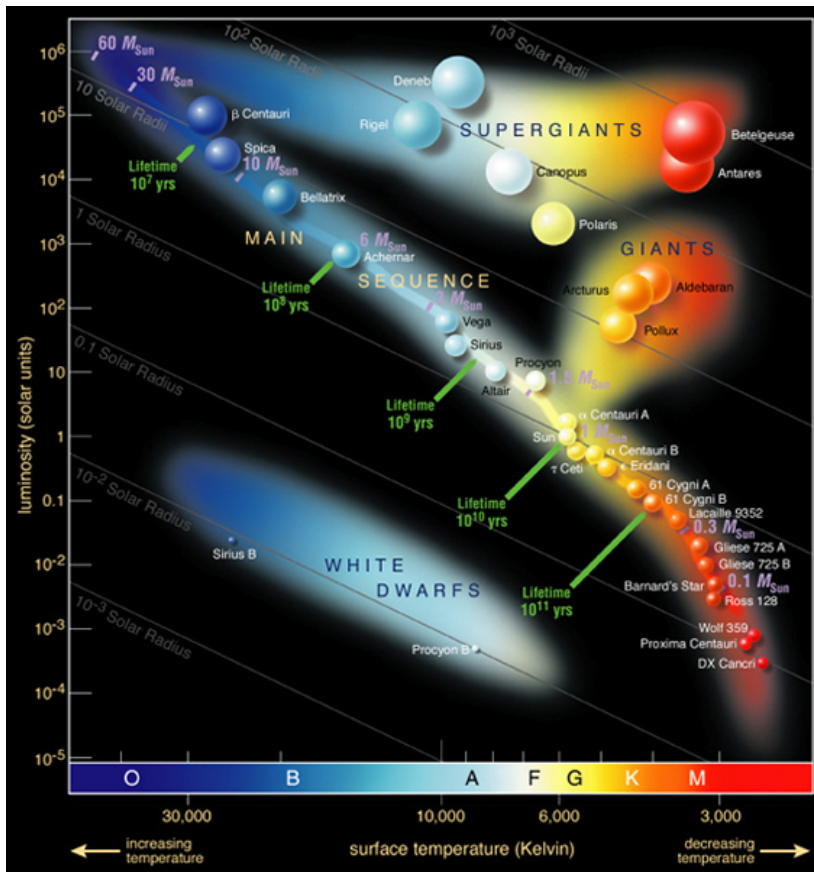
Figure 1.1: The Hertzsprung-Russell (HR) diagram. This diagram relates the spectral type and the surface temperature (both showed at the axis of abscissas) with absolute magnitude or luminosity (in the ordinate axis). The crosswise lines indicate lines of constant radius. Credits: European Southern Observatory (ESO) (http://www.eso.org/public/images/).

$$M_\star > 85\,M_\odot : \quad \text{O} \to \text{Of} \to \text{LBV} \to \text{WN} \to \text{WC} \to \text{SN}$$
$$40\,M_\odot < M_\star < 85\,M_\odot : \quad \text{O} \to \text{Of} \to \text{WN} \to \text{WC} \to \text{SN}$$
$$25\,M_\odot < M_\star < 40\,M_\odot : \quad \text{O} \to \text{RSG} \to \text{WN} \to \text{WC} \to \text{SN}$$
$$20\,M_\odot < M_\star < 25\,M_\odot : \quad \text{O} \to \text{RSG} \to \text{WN} \to \text{SN}$$
$$10\,M_\odot < M_\star < 20\,M_\odot : \quad \text{O} \to \text{RSG} \to \text{BSG} \to \text{SN}$$

If the initial mass of the star is not too large ($< 25\,M_\odot$), the stellar remnant of the SN in the inner core will stabilize and become a *neutron star*. However, if the initial mass is much larger the collapse will be completed, and a *black hole* will be formed.

1
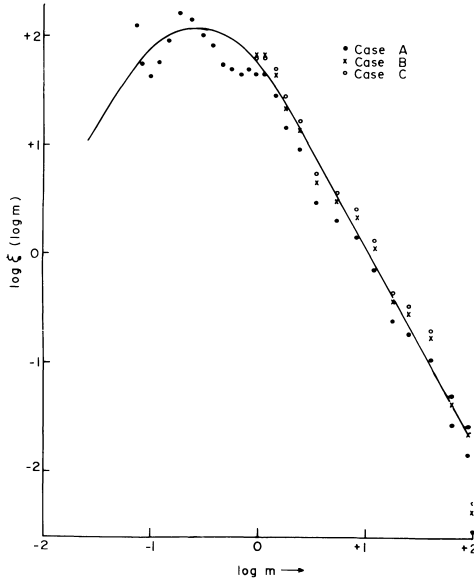
Figure 1.2: The initial mass function, ξ, of main sequence stars of the disc population around the Sun. A single power law seems to fit from $m \simeq 1.5$ to about $m \simeq 100$. Credits: Rana (1987).
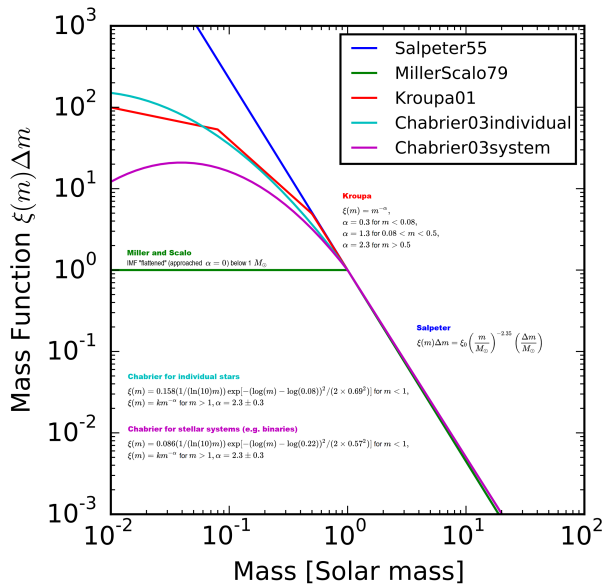
Figure 1.3: Salpeter, Miller & Scalo, Kroupa, and Chabrier proposed IMFs. Credits: Figure based on the main figure by Johannes Buchner published in the free media repository Wikimedia Commons, licensed under the Creative Commons Attribution-Share Alike 4.0 International license.

Another striking feature of massive stars is their high fraction of multiplicity ($\sim 91\,\%$ according to Sana et al. 2014), which must therefore be taken into account when studying their evolution and the heavy end of the IMF.

1.2. Winds from massive stars

Massive stars produce strong stellar winds. In 1975 Panagia & Felli and Wright & Barlow derived the radio continuum flux density that would arise from the free-free thermal emission of a spherically expanding ionised stellar wind envelope of a star undergoing mass loss, with an electron density profile $n_e \propto r^{-2}$ (being r the distance from the central star), solving the equation of radiative transfer. They determined that the measured radio flux can be related to the properties of the stellar wind by the expression

$$\left[\frac{S_\nu}{mJy}\right] = (5.34 \times 10^{-4})^{-4/3} \left[\frac{\dot{M}}{M_\odot\, yr^{-1}}\right] \left[\frac{v_\infty}{km\, s^{-1}}\right]^{-4/3} \left[\frac{d}{kpc}\right]^{-2} \left[\frac{\nu}{Hz}\right]^{2/3} \left[\frac{\mu^2}{Z^2 \gamma g_\nu}\right]^{-2/3},$$

$$(1.1)$$

being S_ν the flux density in milli-Janskys, v_∞ the terminal velocity of the stellar wind in kilometers per second, ν the observed frequency in Hertz, and d the distance to the observer in kiloparsecs. The parameters μ, Z, and γ are the mean molecular weight, the mean ionic charge, and the mean number of electrons per ion, respectively. If A_i, M_i, and Z_i are the fractional abundance, the molecular weight, and the ionic charge of the ith atomic/ionic species, then μ, Z, and γ can be defined as

$$\mu = \frac{\sum A_i M_i}{\sum A_i}, \quad Z = \frac{\left(\sum A_i Z_i^2\right)^{1/2}}{\sum A_i}, \quad \gamma = \frac{\sum A_i Z_i}{\sum A_i},$$

$$(1.2)$$

In addition, the free-free Gaunt factor, g_ν, can be obtained by means of the expression

$$g_\nu = 9.77 \cdot \left(1 + 0.13 \cdot \log \frac{T_e^{3/2}}{Z\nu}\right),$$

$$(1.3)$$

with T_e as the electron temperature of the wind in Kelvins. Then, the characteristic thermal radio spectrum follows a power-law with frequency, $S_\nu \propto \nu^\alpha$, where the slope of the power-law, α, is the termed the *spectral index*. At centimetre wavelengths $g_\nu \propto \nu^{-0.1}$ and therefore $\alpha \approx 0.6$. Values of α greater than 0.6 are explained as deviations from the previous assumptions, such as the presence of condensations (*clumps*) that produce a non-standard electron density profile ($n_e \propto r^{-s}$, with

$s \neq 2$) and/or changes in the ionisation state due to shocks, as it is discussed in the next paragraph.

Particle acceleration in shocks can change the observed spectral index of stellar winds. Typical scenarios are

- The supersonic ionised wind shell around a star encounters dense interstellar medium near the star. However, typically the region around observed radio stars has already been swept clear of such material.

- The stellar wind suffers instabilities that produce internal shocks.

- Binary stars: Most massive stars are born as part of binaries or higher multiples. If both stars in a binary are sufficiently evolved to produce strong stellar winds, then a shock will be produced in the wind colliding region.

Figure 1.4 illustrates these scenarios.
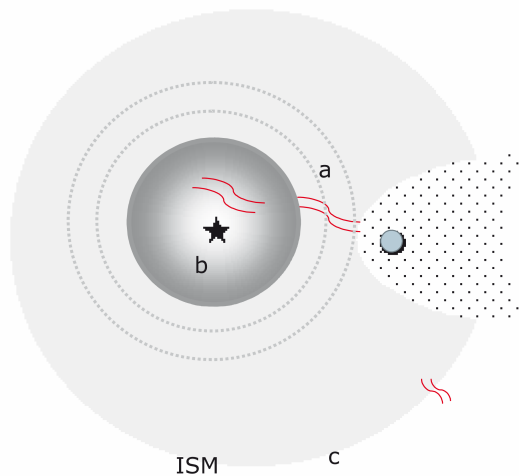
Figure 1.4: Possible regions for shock-mediated particle acceleration in massive star winds: a) wind-wind collision regions in binaries or higher multiples; b) instabilities within the stellar wind of a single star; c) terminal shock region if the stellar winds hits nearby dense ISM. Credits: Benaglia (2010).

Flat to inverted spectra ($\alpha \lesssim 0$) can be found in binaries as result from the contribution of non-thermal emission in colliding wind regions, provided this emission is not absorbed by the surrounding ionised wind, which is optically thick (Benaglia, 2010; Montes et al., 2015). Thus, identifying binaries through radio observations should be typically limited to the detection of wide binaries with periods of one year or longer (Sanchez-Bermudez et al., 2019). In the case of short-period ($P \sim< 1$ yr)

colliding wind binaries (CWBs), the stars are too close and the wind–wind collision region (WCR) is likely to lie within the optically thick region of the large scale wind that surrounds the entire system. Therefore, in these systems, only the free-free thermal emission from the unshocked winds is thought to be detected, thereby masking any effect of their binarity. However, in some short-period systems (depending on the geometry of the binary and of its interacting winds), emission from the shock region may escape, contributing to a composite spectrum with a flat spectral index at certain orbital phases in systems with significant eccentricity. This non-thermal emission can appear to be modulated by the orbital motion of the system (only if the orbit is non-circular), resulting in variability of the total spectrum with a periodicity related with the orbital period.

Due to these mechanisms, radio observations can provide essential information about the wind properties, mass loss, and multiplicity of massive stars.

1.3. The Galactic centre

The center of the Milky Way is of special importance for studies of massive stars. The Galactic center (GC) contains a massive black hole, Sagittarius A* (Sgr A*), and a stellar nucleus and it is orders of magnitude closer than any comparable target. The GC proper is delimited by the nuclear bulge (NB), a flattened, possibly disklike stellar structure with a radius of 230 pc and a scale height of 45 pc (Launhardt et al., 2002). Although the NB occupies less than 1% of the Milky Way's volume, it emits on the order of 10% of its total Lyman continuum flux, which is produced by a high number of massive, hot stars (e.g. Figer et al., 2004; Mauerhan et al., 2010; Dong et al., 2011). Likewise, the NB is characterised by the most extreme conditions in the Galaxy: a tidal field so intense that even massive, young star clusters dissolve into the background in less than 10 Myr, extreme stellar densities ($10^{5\cdots7}$ pc^{-3}), high turbulence and temperature of the ISM, a strong magnetic field ($>10\%$ of the Galaxy's magnetic energy concentrated in $<0.05\%$ of its volume), and intense UV radiation (e.g. Genzel et al., 2010).

Furthermore, the GC is one of the very few environments where we have strong evidence for a top-heavy IMF (in the Arches, Quintuplet and the Central Parsec clusters: e.g. Paumard et al. 2006; Bartko et al. 2010; Lu et al. 2013). These three known massive, young clusters lie within 30 pc in projection of Sgr A*. Additionally, apparently isolated massive young stars, massive young stellar objects (YSOs) and H II regions bear witness to recent or currently ongoing massive star formation (SF) throughout the NB (e.g. Yusef-Zadeh et al., 2009; Mauerhan et al., 2010; Nandakumar et al., 2018; Shahzamanian et al., 2019). Therefore, the GC is the Milky Way's most important star forming region, and it is the only galactic nucleus and the most extreme astrophysical environment that we can examine on scales of milli-parsecs.

However, there are some unique observational challenges for studying the ste-

llar population of the GC. Interstellar extinction is extremely high ($A_V > 30$ mag) and also variable on arcsecond scales (e.g. Scoville et al., 2003; Schödel et al., 2010; Fritz et al., 2011; Nogueras-Lara et al., 2018, 2019a, 2020). Therefore, even in the near-infrared ($A_K \approx 2.5$ mag), stellar colours are dominated by reddening. Additionally, sub-arcsecond angular resolution (at least as good as about 0.2″) is needed to overcome the high source crowding and to reliably study individual stars, which requires the use of the Hubble Space Telescope, or speckle or adaptive optics techniques from the ground.

In this thesis we study two emblematic massive clusters, Arches and Quintuplet, looking at their compact sources by means of radio interferometric techniques. The high sensitivity delivered by the large bandwidth of the Karl G. Janksy Very Large Array (JVLA) of the National Radio Astronomy Observatory (NRAO)[1] opened us a new observing window onto massive stars in the GC through sensitive, high-angular resolution radio observations. The pickup of the thermal and non-thermal emission from the ionised gas in the winds of young, massive stars provides a way to identify massive cluster members that is fully independent and complementary to NIR observations.

Past radio observations of massive stars lacked the sensitivity to reach beyond at most a few kiloparsecs. Because of the rareness and large mean distances of massive stars and clusters, researchers could were therefore only able to study a limited sample of such targets (Lang et al., 2001, 2005; Benaglia, 2010; Yusef-Zadeh et al., 2015).

With this work we have increased the number of known radio stars in the clusters, tried to discern the multiplicity or not of massive stars on the basis of their spectral indices, estimated the mass-loss rates and used the number of stars as a new tool for constraining the age and/or mass of the clusters and also their mass function.

In addition to this brief introduction, this thesis is composed of six more chapters. The second chapter provides an overview of radio interferometry. From chapter three to four, the main research topics of the present thesis are described. The third chapter is dedicated to Arches cluster, and it includes the data and analysis presented in a peer-reviewed publication. The fourth chapter refers to Quintuplet, and contains its data and an analysis similar to the Arches one.

Finally, chapters five and six describe the general conclusions and future continuation of the presented research, respectively.

---

[1] The NRAO is a facility of the National Science Foundation (NSF) operated under cooperative agreement by Associated Universities, Inc. The NSF is an independent federal agency created by the U.S.A. Congress in 1950 "to promote the progress of science; to advance the national health, prosperity, and welfare; to secure the national defense..."

2

Radio interferometry

He aquí mi secreto. Es muy simple: no se ve bien sino con el corazón.
Lo esencial es invisible a los ojos.

El Principito
Antoine de Saint-Exupéry

I n Astronomy we intend to map the distribution of the emission on the sky from objects that are located far, far away. We actually try to image the brightnes distribution from these objects, not just their global properties as the total flux. The *Flux* is related to the power we are getting from them. The *Brightness* is the distribution of that power as a function of the position. Hence measuring the brightness means make a detailed map of its distribution.

From the earliest time in radioastronomy, single dish antennas were used. Nowadays most observations are carried out with interferometers in order to get the best angular resolution.

2.1. Why do we need interferometry?

The *angular resolution* makes reference in radio astronomy to the ability of a radio telescope to separate two objects that are located at a small angular distance. Radio telescopes coherently sum electric fields over an aperture of size D, that is, the antenna size. Therefore, considering the wave nature of light and the phenomenon of diffraction through a circular aperture into account, and according to the Rayleigh

criterion[1], the angular resolution is given by:

$$\theta_{[radians]} = 1.22 \, \frac{\lambda}{D} \tag{2.1}$$

where λ is the wavelength of the light and D the diameter of the circular aperture. Considering more convenient units for radio astronomy, θ can be expressed as follows:

$$\theta_{[arcsec]} \approx 2.5 \, \frac{\lambda_{[cm]}}{D_{[Km]}} \tag{2.2}$$

being λ the wavelength of the observations and D the diameter of a single dish antenna.

According to these equations, to obtain 1 arcsecond resolution at a wavelength of 21 cm, we would require an aperture of approximately 53 Km!. The construction of such a radio telescope is not feasible, but we could synthesise an aperture of that size with pairs of antennas. Then, the angular resolution limited by the Rayleigh criterion lead us to develop the technique of synthesising a larger aperture through combinations of separated pairs of antennas, what is known as *aperture synthesis*.

2.2. Some basic concepts

Considering a simple assumption, the antenna of a radio telescope acts as a collector of radio waves and put them in phase at its focus, in the same way as a curved mirror can focus visible light to a point. In other words, a parabolic dish coherently sums electromagnetic (EM) fields at the focus, as we mentioned in previous section. This is a great way of collecting a lot of energy and put it in phase in one place where we could locate a receiver. If we had several antennas, each one with its receiver, we could add the EM signals as voltages preserving the amplitudes and phases, finally getting a virtual focus or a "correlation" receiver that would give an output proportional to the average of the voltages from all antennas. That is a key point in interferometry.

2.2.1. A two-element simplified interferometer

Let us consider the most basic interferometer, just to illustrate the relation between the characteristics of the correlator product and the brightness distribution of the emitting source. As a first attempt, we are assuming several simplifications: our interferometer is fixed (there is no rotation or motion), it works with quasi-monochromatic radiation (i.e., responds only to radiation in a very narrow band), without any frequency conversions, and with single polarization; additionally, there are not distortions on the wave front due to the atmosphere, ... and, finally, we

---

[1]The Rayleigh criterion states that two point sources can be distinguished when the principal diffraction maximum of the Airy disk of one image coincides with the first minimum of the Airy disk of the other.

assume an idealised electronic (perfectly linear, identical for all the elements of the interferometer, no added noise, ...).
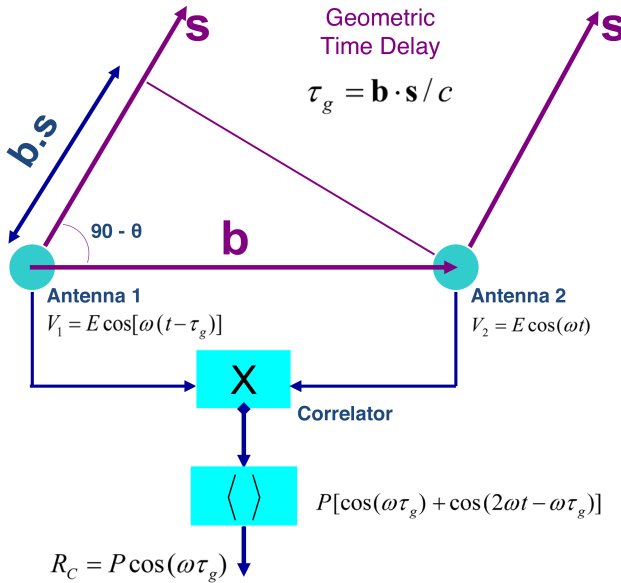
Figure 2.1: Geometry of a two-element interferometer. The radio source under observation is in the direction given by the unit vector **s**. The baseline vector **b** connects the phase centres of the two antennas. The signal arrives at the second antenna delayed by the geometrical time delay τ_g. Credit: Based on a figure by and with permission from Rick Perley (NRAO, EE.UU.)

Figure 2.1 illustrates this simple case: a two-element interferometer. Considering the phase centres of the two antennas connected by the baseline vector **b**, and the radio source under observation in the direction given by the unit vector **s**, the time delay, τ_g can be obtained as

$$\tau_g = \frac{\mathbf{b} \cdot \mathbf{s}}{c} \tag{2.3}$$

where c is the velocity of the light.

The two signals from the same wave front that arrive to the pair of antennas are converted to voltages that are fed to a correlator which multiplies these voltages allowing for the time delay correction in order to obtain the interferometric fringes. Then, the correlator time averages the signal and gives the final output. The averaged product, R_C, is dependent on the receiver power, $P = E^2/2$, and the geometric delay, τ_g, and hence on the baseline orientation and source direction:

$$R_C = P \, cos(\omega\tau_g) = P \, cos\left(2\pi \, \frac{\mathbf{b} \cdot \mathbf{s}}{\lambda}\right) \tag{2.4}$$

Here, $\omega\tau_g$ is the phase difference associated with the time delay between the antennas.

The correlator output voltage will be a function of the observing time if the source itself is variable. The intensity of the correlated signal will depend on the antennas separation and the antenna gains, but these gains can be calibrated.

To illustrate the response, we could expand $\mathbf{b} \cdot \mathbf{s}/\lambda$ in one dimension as follows:

$$\frac{\mathbf{b} \cdot \mathbf{s}}{\lambda} = u \, cos(\alpha) = u \, sin(\theta) = ul \tag{2.5}$$

measuring the baseline length in number of wavelenghts, $u = \mathbf{b}/\lambda$, which is the inverse of the instantaneous angular resolution, α the observing angle of the interferometer, and θ its complementary angle, resulting in $l = cos(\alpha) = sin(\theta)$.

Thus, the "cosine" response can be written as

$$R_C = P \, cos(\omega\tau_g) = P \, cos\left(2\pi \, \frac{\mathbf{b} \cdot \mathbf{s}}{\lambda}\right) = P \, cos(2\pi ul) \tag{2.6}$$

The sinusoids that represent the interference of the wave fronts represent the *interferometric fringes*, characterized by an amplitude and a phase, and form a response pattern. The patterns are modulated in amplitude and phase by the antennas that impose their own patterns just for not having isotropic responses (there is a dependence on the angle on the sky).

Similarly, the response from an extended source is obtained by adding the responses of each of the individual sources in which the extended source can be divided, taken into account the difference of delay due to the different position in the sky of each of the individual sources. If we suppose that the emission is spatially incoherent, the correlator output voltage will be the flux understood as the spatial integration of the brightness, modulated by the cosinusoidal interferometer pattern. In this way, we find a link between the brightness on the sky to something we can measure, R_C, the interferometer response.

In summary, we could say that the interferometer casts a cosinusoidal pattern on the sky, and we obtain a response which is some function of the source brightness distribution and the fringe separation and orientation.

Nevertheless, since the cosine fringe pattern is even, the response of our interferometer to the odd brightness distribution will be none, or what is the same, the cosine correlator is blind to odd structure.

To solve this problem, we generate a "sine" pattern by inserting 90 degree phase shift in one of the signal paths

$$R_S = P \ sin(\omega\tau_g) \tag{2.7}$$

and we define a complex function, the complex visibility, V(b), which is a function of the baseline length and relative orientation with respect to the source, from the two independent correlator outputs R_C and R_S.

$$V = R_C - iR_S = A \ e^{-i\phi} = \int\int I_\nu(s) \ e^{-2\pi i\nu \mathbf{b} \cdot \mathbf{s}/c} \ d\Omega, \tag{2.8}$$

where $A = \sqrt{R_C^2 + R_S^2}$, $\phi = tan^{-1}\left(\dfrac{R_S}{R_C}\right)$ and $I_\nu(s)$ represents the intensity of the source.

Under some circumstances, this is a 2-D Fourier transform, giving us a well established way to recover I(s) from V(b).

The general picture presented so far describes an ideal case, but real sensors (antennas) have a directional voltage gain pattern that attenuates the actual sky brightness distribution. Additionally, we really should take into account the effects from a finite bandwidth, observations off the meridian, the Earth rotation, the atmosphere, the electronic, ... but we will not describe them in this PhD.

2.2.2. The *(u,v)* plane

The response functions we have seen in subsection 2.2.1 depend on two fundamental vectors: the baseline, **b**, defining the vector that joins the phase center of the antennas, and the unit vector, **s**, specifying the source direction on the sky.

Thus, the coordinate system most generally used for synthesis imaging is a Cartesian coordinate system (u, v, w) to describe the baselines (see Figure 2.2). The baseline vector is specified by these three coordinates measured as the inverse of the instantaneous angular resolution, whereas the unit direction vector is defined by its projections, (l, m, n), on the (u, v, w) axes, which are called the *direction cosines*. Generally, "w" is arranged to point to the source (phase tracking centre) and the plane (u, v) is tangential to Earth surface and is oriented so the "v" axis points towards the north celestial pole (NCP), and "u" towards the East. The direction cosines "l" and "m" increase to the East and North, respectively.

In this coordinate system, formally in two dimensions, not considering the w coordinate,

$$I_\nu(l, m) = \int\int V_\nu(u, v) \ e^{-i2\pi(ul+vm)} \ du \ dv, \tag{2.9}$$
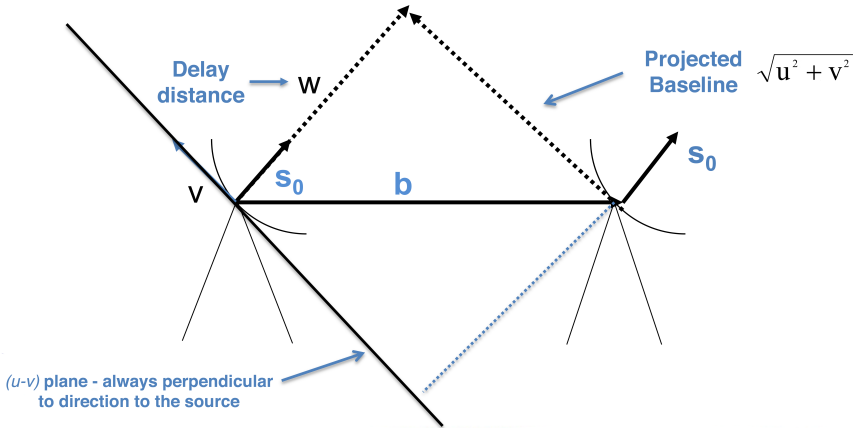
Figure 2.2: General coordinate system. Credit: Reprinted with permission from the 16th Synthesis Imaging Workshop at NRAO.

which is, in physical optics, known as the *Van Cittert-Zernicke Theorem* [2]. The brightness distribution is the Fourier transform of the visibility function, which is what the interferometer is measuring and is the result of the correlation. We should perform the Fourier inversion to obtain the brightness distribution. This inversion is actually done through the process of "*Imaging*". In this thesis, it has been used the Common Astronomy Software Applications package (CASA)[3] to process data, including fringe-fitting, calibration and imaging.

An interferometer, at any time, measures the visibility function at a given time for a baseline coordinate (u, v). Then the distribution of the antennas of the array and the number of antennas will have an important effect on the number of points where the visibility is measured. All the points for which the visibility is measured form the $u-v$ plane and defines the sampling of the source visibility. The greater the number of antennas, the more baselines between them will be available, creating a more complete effective coverage of the $u - v$ plane. If we only observe a few seconds with a two-element interferometer, such as that illustrated in Figure 2.1, we will produce a $u - v$ plane with only two points. If the source is circumpolar and we observe around 12 hours instead, the rotation of the Earth will have the effect of increasing the coverage, with the appearance of an elliptical coverage (this is known as Earth's rotation synthesis). Positioning of the array elements in

---

[2]The Van Cittert-Zernicke Theorem states that the Fourier Transform of the spatial coherence function of an incoherent source is equal to its complex visibility.

[3]CASA is developed by an international consortium of scientists based at the National Radio Astronomical Observatory (NRAO), the European Southern Observatory (ESO), the National Astronomical Observatory of Japan (NAOJ), the Academia Sinica Institute of Astronomy and Astrophysics (ASIAA), the CSIRO division for Astronomy and Space Science (CASS), and the Netherlands Institute for Radio Astronomy (ASTRON) under the guidance of NRAO.

HA = -2h   HA = 0h   HA = 2h

Coverage over
all four hours.
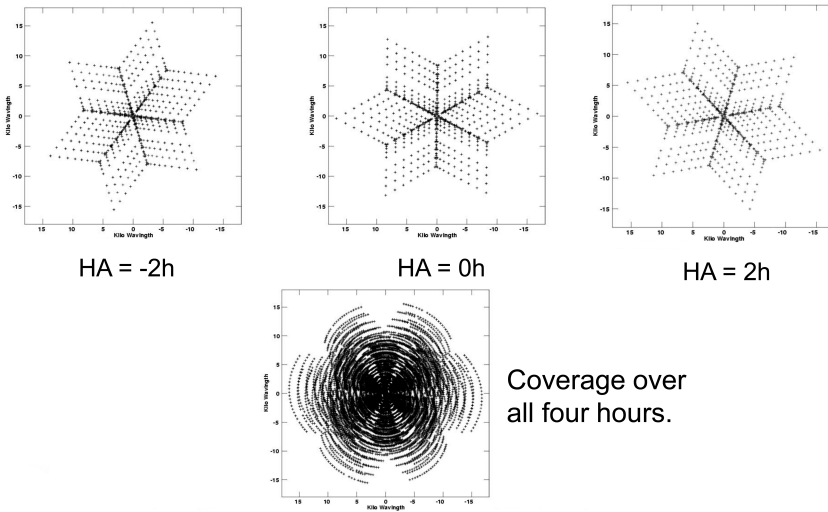
Figure 2.3: Sample VLA (u, v) plots for 3C147 ($\delta = 50$). Snapshot $u - v$ coverage for HA = -2, 0, +2 (with 26 antennas). Credit: Rick Perley (NRAO, EE.UU.)

two dimensions in a "Y" or a spiral configuration will increase the $u - v$ coverage over the effective telescope area, improving the angular resolution and sensitivity of the interferometer. Figure 2.3 shows the $u - v$ plane coverage over four hours of observation over the standard calibrator 3C147 ($\delta = 50$) of the Y shaped array using 26 antennas at the Very Large Array (VLA).

Note that if the target source is a *point source* [4], the interferometer response will be the same for every time and baseline. For an extended source or in order to image diffuse emission, a large number of baselines along a long observing time, with different orientations in the $u - v$ plane, will be required to better define the source structure, that will be partially resolved depending on the instantaneous baseline length.

2.3. The Very Large Array interferometer

The Very Large Array was formally inaugurated in 1980. Operated by the National Radio Astronomy Observatory (NRAO)[5], it is situated on the plains of San Agustin near Socorro, New Mexico (U.S.A). Consisting of 28 antennas (including the one as a spare) mounted over rails in an iconic "Y" shape, it was the largest connected radiointerferometer in the world in those days. Each antenna has a dish size of 25 meters and can be moved independently by transporter along the rails laid out in

---

[4]A *point source* is an object much smaller than the interferometric beam.
[5]The NRAO is a facility of the National Science Foundation (NSF) operated under cooperative agreement by Associated Universities, Inc.

the "Y" pattern. The angular resolution of the VLA is modified by changing the array configuration, i.e. the positions of the dishes. For example, if we are observing at the same frequency and keeping in mind the equation 2.1, it is necessary to increase the separation between the antennas or, in other words, increase the baseline, to improve it. The maximum distance between the antennas is 36 Km in the A configuration and the minimum 1 Km in D configuration.

Figure 2.4: An aerial view of the Very Large Array showing the iconic VLA's Y-shape that give its highest resolution capability. Credit: NRAO/AUI/NSF

2.3.1. Upgrade and renaming: the Karl Guthe Janksy Very Large Array

Just with the aim to update the old 1970's technology of the VLA, improvements were made in the quality of the receivers, bandwidth, frequency coverage, among others, optimizing its sensitivity and spectral resolution.

The Expanded Very Large Array (EVLA), currently renamed as Karl G. Janksy Very Large Array (JVLA), improved the continuum sensitivity by, at least, up to an order of magnitude by increasing the bandwidth from the VLA's 100 MHz per polarization to 8 GHz per polarization, offering a complete frequency coverage from 1 to 50 GHz (in the old VLA was only 21%), and the implementation of a new correlator that can process the large bandwidth with a minimum of 16,384 spectral channels per baseline.

A comparison of some of the JVLA performance parameters with those of the original VLA is provided in Table 2.1. It should be pointed out that the continuum sensitivity is better by a factor of ten.

The new high sensitivity delivered by the large bandwidth of the JVLA opens a

Table 2.1: Overall JVLA Performance Goals

Parameter	VLA	JVLA	Factor[a]
Continuum Sensitivity (1-σ, 9 hr)	10 μJy	1 μJy	10
Maximum Band Width in each polarization	0.1 GHz	8 GHz	80
Number of frequency channels at max. Band Width	16	16384	1024
Maximum number of frequency channels	512	4194304	8192
Coarsest frequency resolution	50 MHz	2 MHz	25
Finest frequency resolution	381 Hz	0.12 Hz	3180
Number of full-polarization sub-correlators	2	64	32
Log (Frequency Coverage over 1−50 GHz)	22%	100%	5

[a] The "Factor" gives the factor by which the JVLA parameter will be an improvement over the equivalent VLA parameter.
Source: JVLA Website (https://science.nrao.edu/facilities/vla/docs/manuals/oss2013B/intro/project).

new observing window onto massive stars in the Galactic centre (GC) through sensitive, high-angular resolution radio observations. In this work, we took advantage of this enhancement, demonstrating the new possibilities that the JVLA is offering, using it as a precursor of future high sensitivity radio interferometers as the SKA or the next generation VLA.

2.3.2. The Next Generation Very Large Array – ngVLA
The next-generation VLA (ngVLA) is a future centimeter-to-millimeter wave interferometer that will be built as the legacy of the JVLA, the VLBA, and complementary to ALMA.

The ngVLA will consist of 244 dishes of 18 m diameter. Of these, 214 will be concentrated in an extension reaching up to ~1,000 km baselines and will comprise the main array. The remaining 30 (18 m) antennas will be distributed as very long baselines up to 9,000 km, and are referred to as the Long Baseline Array (LBA). Additionally, 19 dishes of 6 m will make up a Short Baseline Array (SBA).

The ngVLA dishes will not be movable, so different angular scales will be achieved using sub-array selection and different weighting schemes. It will also extend the operational frequency range covering from 1.2 to 116 GHz (25–0.26 cm). It will cover the frequency range between those covered by ALMA at (sub-)mm wavelengths, and the future Square Kilometre Array at mid-frequency (SKA1-MID) and longer (decimetric) wavelengths.

The ngVLA will open a new window to the Universe through ultra-sensitive imaging of thermal line and continuum emission down to milliarcsecond resolution, as well as unprecedented broad band high-angular-resolution continuum polarimetric imaging of non-thermal processes.

3

The Arches cluster

3.1. Introduction

The Arches cluster is the densest known star cluster in our galaxy. It contains more than 100 O-stars and has a total mass of one to a few $\times 10^4 \, M_\odot$. It thus belongs to a small handful of young, massive, starburst-like clusters known in the Milky Way (in addition to, e.g. NGC3603, Quintuplet, or Westerlund 1 and 2). Located at a projected distance of $\sim 26 \, pc$ to the northeast of Sgr A*, or approximately $11'$ in angular distance, it was discovered by Tetsuya Nagata in 1995 and, independently, by Angela Cotera in 1996. The cluster was formed between 2 and 4 Myr ago (e.g. Figer et al., 1999a,b; Najarro et al., 2004; Clarkson et al., 2012; Clark et al., 2018a, 2019) and has a half-light radius of $r_h \approx 0.48 \, pc$ (Hosek et al., 2015).

Lang et al. (2005) carried out a multi-frequency, multi-configuration, and multi-epoch study of the Arches cluster with the Very Large Array (VLA), reaching 1σ flux uncertainties of $\sim 30 \, \mu Jy$ at 8.5 GHz. They detected ten compact sources in the Arches cluster that could all be associated with massive, young stars detected in the NIR. All but the brightest of these sources (AR1) were unresolved and their spectral indices were consistent with stellar wind sources, which were used to estimate their mass-loss rates. Roughly half of the sources showed indications of moderate variability in their work.

3
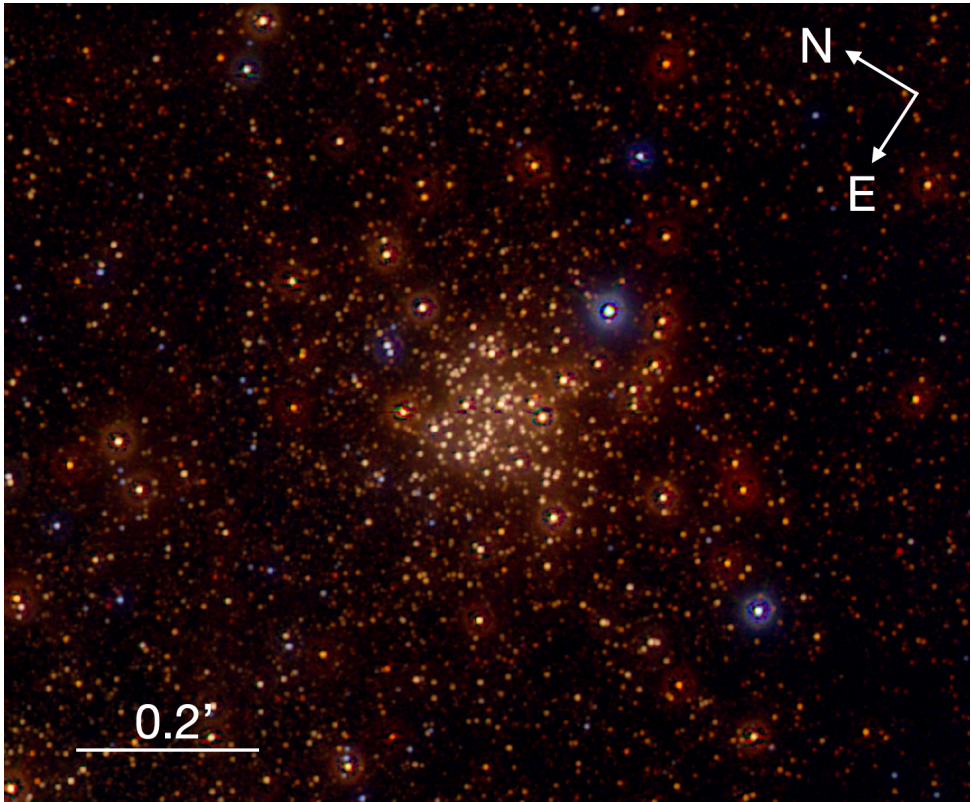
Figure 3.1: JHKs false colour image of the Arches cluster from the GALACTICNUCLEUS survey. Credits: Nogueras-Lara et al. (2018, 2019a), publications in which the author of this thesis, Aurelia Teresa Gallego Calvente, is co-author.

We revisited the Arches cluster aiming to measure up the thermal and non-thermal emission from the ionised gas in the winds of the young, massive stars, taking advantage of the significantly increased sensitivity of the JVLA since previous observations were performed by Lang et al. (2005).

Clark et al. (2018a, 2019) recently provided the spectral classifications for 88 Arches cluster members based on a new multi-epoch NIR spectroscopic survey of the cluster obtained with the integral field spectrograph SINFONI mounted on the Very Large Telescope (VLT) along with photometry from the Hubble Space Telescope Wide Field Camera 3 (HST/WFC3). Their sample of the most massive stars in the Arches cluster is roughly three times larger than the one presented previously by Martins et al. (2008). We use this spectroscopic work as a source of information on the properties of the stars that we detect at radio wavelengths.

3.2. Observations and imaging

We observed the radio continuum emission from the Arches cluster using the JVLA of NRAO. The position α, $\delta_{(J2000)}$ = $17^h\,45^m\,50.49^s$, $-28°\,49'\,19.92''$ was taken as phase centre. There are three epochs of X-band (3.0 cm or a representative frequency of 10 GHz) and one of C-band (5.0 cm or 6 GHz) observations. Details are listed in Table 3.1.

Table 3.1: Observational properties

Observation date	Band[a]	JVLA configuration	On source time (minutes)
Oct 04, 2016	X	A	55
Oct 26, 2016	X	A	55
Apr 11, 2018	X	A	55
Jun 10, 2018	C	A	74

[a] Frequency range of 4-8 GHz for C-band and 8-12 GHz for X-band. Therefore, the total bandwidth was 4 GHz on each band. The number of spectral windows was 32 and the number of channels 64 in both cases.

All observations were acquired in the A configuration to achieve the highest angular resolution. This configuration also helped us to filter out part of the extended emission from the Arched Filaments (G0.10+0.08), a very extended H II region in which the Arches cluster is embedded.

At all frequencies, J1744−3116 was used as a phase calibrator and J1331+305 (3C286) as a band-pass and flux density calibrator. For C- and X-bands, we required a sensitivity of 3.0 μJy beam^{-1}. Raw data were processed automatically through the JVLA calibration pipeline performing an initial flagging and calibration. Extra flagging was necessary to remove the lost or corrupted data. We performed standard data reduction using the Common Astronomy Software Applications package, CASA.

Images were created with CASA using the classical task `clean` in interactive mode. We also tested a more advanced form of imaging, `multi-scale clean`, to distinguish between the point sources and the extended emission. `Multi-scale clean` involves the use of multiple scales by means of an extension of the classical `clean` algorithm assuming the sky is composed of emission at different angular scales. Its use did not improve the quality of the image. We also probed various other options for the task `clean` including wide-field, multi-term, multi-frequency synthesis and with w-projection without resulting in any significant improvements. Additionally, we checked different weighting schemes to correct for visibility sampling effects. Natural weighting produced an optimum image with the lowest noise (highest signal-to-noise ratio (S/N)). The gain parameter, which sets the fraction of the flux density in the residual image that is removed and placed into the clean model at each minor cycle iteration, was set to 0.05, which helped us to deal with the diffuse emission present in our target. The visibility data sets from

2016 were cleaned in two ways, separately and concatenated. In the first case, self-calibration could not be applied, possibly because this method requires sufficient S/N at each solution interval. In the second case (2016 data sets concatenated), self-calibration was applied just in phase, just in amplitude, and in phase and amplitude simultaneously. The best image resulted from applying one cycle of phase self-calibration to correct for antenna-based phase errors selecting interactively the brightest compact sources as input model, as well as amplitude self-calibration (the latter with no changes in the flux density of the compact sources). The off-source root mean square (rms) noise level reached in the final image with this procedure was $2.5 \, \mu$Jy beam^{-1}. Self-calibration could not be applied to the 2018 single data sets either. The off-source thermal noise reached in this epoch was 4.0 and $4.7 \, \mu$Jy beam^{-1} for X- and C-bands, respectively. All the final images were primary beam corrected to account for the change in sensitivity across the primary beam. Table 3.2 summarises the properties of the final images.

Table 3.2: Properties of the images

Epoch	Band	Frequency [a] (GHz)	Synthesised beam (arcsec × arcsec)	P. A. [b] (degrees)	rms noise [c] (μJy beam^{-1})	(u, v) cut-off (kλ)	Θ_{LAS} [d] (arcsec)
2016	X	10.0	0.48 × 0.18	20.84	2.5	150	5.3
2018	X	10.0	0.46 × 0.17	−17.33	4.0	150	5.3
2018	C	6.0	0.62 × 0.28	2.82	4.7	100	8.9

[a] Representative frequency, in Gigahertz.
[b] The position angle (P. A.) of the fitted major axis for the synthesised beam, in degrees.
[c] Off-source root mean square noise level reached.
[d] Largest Angular Scale, Θ_{LAS}: Scale at which severe attenuation of large-scale structure occurs (in arcseconds).

As the cluster is located in an extended H II region and the primary beam sizes at 5 and 3 cm were relatively large (approximately 5′ and 8′, respectively), a spatial frequency cut-off was also required in order to resolve the diffuse emission and detect the compact sources with high S/N. Considering that the field of view (FoV) is of the order of $\theta(\mathrm{PB}) = 42 \, \nu_{\mathrm{GHz}}^{-1}$ in arcminutes (i.e. 8.4 and 4.2 arcminutes at C- and X- bands respectively), the Central Parsec Cluster and Sgr A* are not within the FoV at any frequency. Thus, no flux from Sgr A* is bleeding into the target fields. Nevertheless, we verified via large FoV imaging that Quintuplet was within the FoV for both epochs but does not contribute significantly to the flux density. Therefore, we are certain that no flux from nearby bright regions leaked into the FoV of our reconstructed images. Table 3.2 also lists the cut-offs made to the data in the (u, v) plane and the scale at which severe attenuation of large-scale structure occurs.

3.3. Results

3.3.1. Point source detection and calibration

The positions and flux densities of the detected radio sources were taken from the final primary-beam-corrected images using the `CASA-imfit` task which fits elliptical 2D Gaussians to interactively selected polygon regions around source candidates. The task provided us with estimations of the positions of the maxima, the total flux densities, and the errors of these values taking the quality of the fit and the image rms into account. Uncertainties in positions were calculated by adding in quadrature a systematic error of 0.05″(Dzib et al., 2017) to the formal error of the fit, $0.5\,\theta$/SNR (Reid et al., 1988), where θ is the source size convolved with the beam and SNR the S/N.

$$\sigma_{position} = \sqrt{\left(\frac{\theta}{2 \cdot SNR}\right)^2 + (0.05'')^2} \qquad (3.1)$$

The systematic error accounts for the thermal noise and uncertainties introduced by the phase calibration process. In the determination of the flux-density uncertainties, we also considered the percentage in the calibration error of the peak flux densities at the frequencies observed (Perley & Butler, 2013), S_ν, and a factor, F, that takes into account whether a source is resolved or unresolved.

$$\sigma_{flux} = \sqrt{(F \cdot RMS)^2 + (0.15 \cdot S_\nu)^2}, \qquad (3.2)$$

where $F = \sqrt{\frac{Area_{source}}{Area_{beam}}}$.

With these premises, 18 and 15 sources were detected above five times the off-source rms noise level at 10 GHz and 6 GHz, respectively.

The 2016 X-band image has the highest S/N of all images and provides the most complete list of point sources. The presence of ionised gas in clouds of variable compactness, as well as artefacts introduced by the brightest radio sources into the images, can give rise to point sources that are either spurious or related to features within the extended emission. We therefore compared the positions of the radio point sources detected in the 2016 X-band image with the positions of stars in an HST/WFC3 F153M image of the Arches cluster (Hosek et al., 2015) and eliminated all radio sources that did not show unambiguous coincidence (within less than half of the NIR and radio beam full width at half maxima). The radio stars are labelled in the NIR image of the Arches cluster shown in Fig. 3.2. Point sources were selected interactively in the 2016 radio image, restricting ourselves to those at $5\,\sigma$ above the off-source rms noise level. Within the approximately $2.1' \times 2.3'$ WFC3 image there
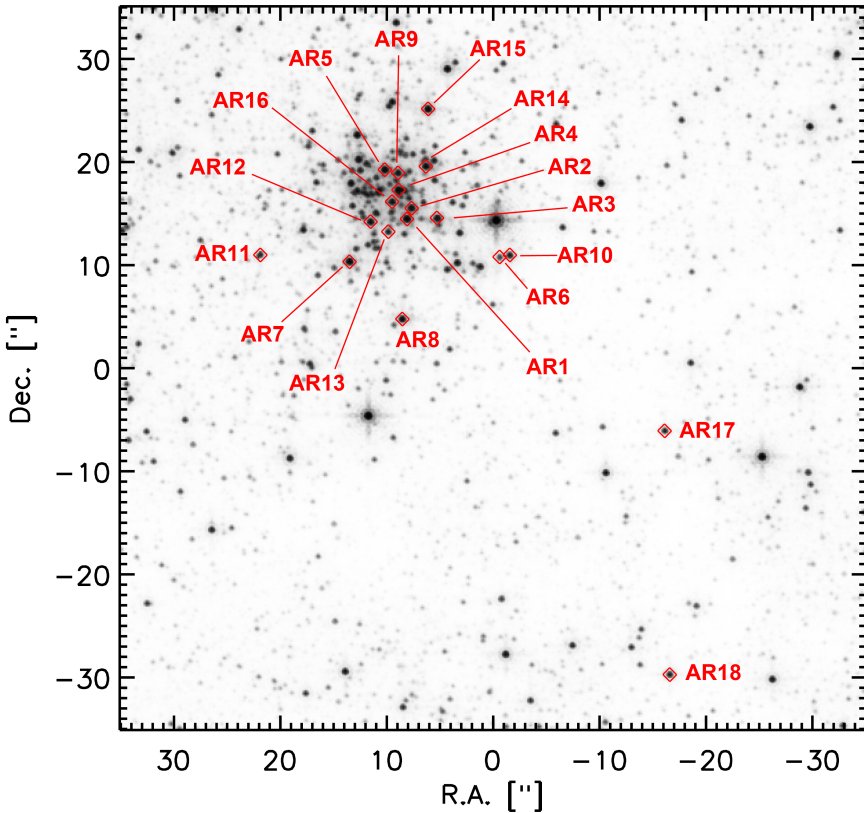
Figure 3.2: HST/WFC3 F153M image of the Arches cluster with identified radio stars labelled.

are 18 of a total of 23 5σ radio detections that clearly coincide with stars. With the 2018 data, we only detected the radio stars with the 5σ criterion (almost all the stellar point sources identified in 2016) and no spurious sources.

Figure 3.3 shows a closeup onto the 2016 X-band image and a closeup onto the 2018 C-band image of the Arches cluster with all radio stars labelled. Sources AR1-10 were reported by Lang et al. (2005). Sources with higher numbers are our new detections.

When comparing the flux densities from our 2016 and 2018 X-band images, we noted an offset of a factor of about two between the epochs. As the observations by Lang et al. (2005) were done at 8.5 GHz, very close in frequency to our 10 GHz observations, we can compare our measurements with theirs to infer the systematic errors. Table 3.3 lists the measured flux densities for the point sources in the X-band image of the 2018 epoch along with the 8.5 GHz fluxes of Lang et al. (2005), where available. We should mention that this factor of about two between our 2016 and 2018 epochs is not due to a problem in the absolute flux density calibration
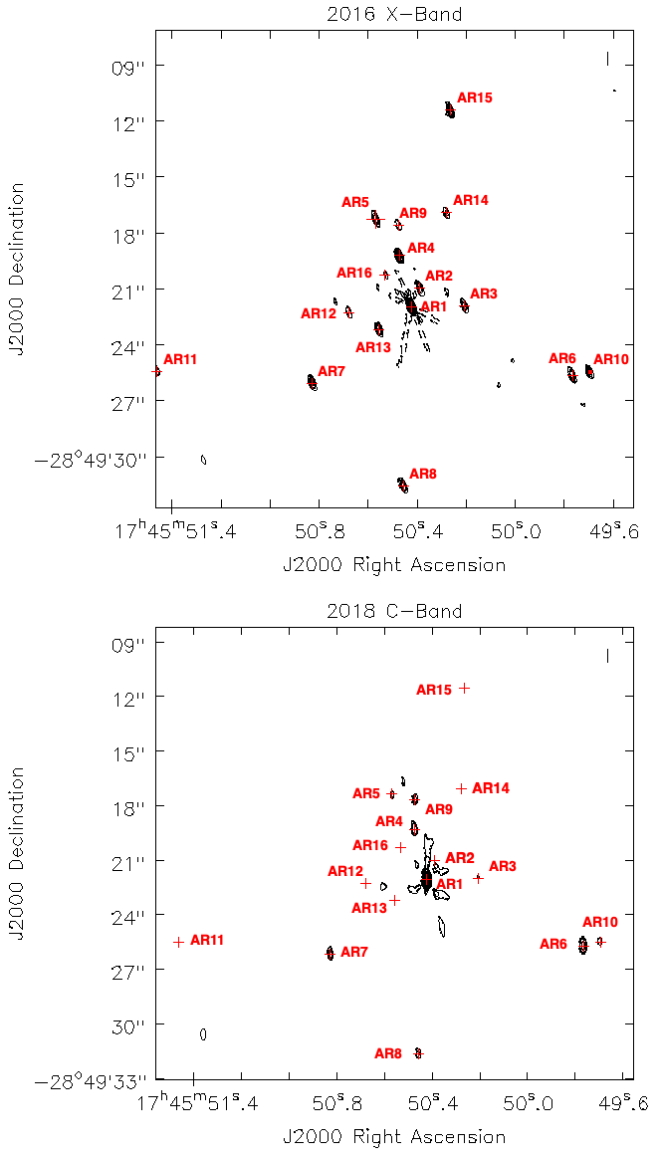
Figure 3.3: Top: Closeup onto the Arches cluster from the 2016 X-band image not corrected for primary beam attenuation. The clean beam is $0.48'' \times 0.18''$, P.A. = 20.84°. The off-source rms noise level is $2.5\,\mu\mathrm{Jy\,beam^{-1}}$. The contour levels represent -1, 1, 3, 5, 10, 15, 25, 35, 45, 55, and 60 times the off-source rms noise level multiplied by 5. Bottom: Closeup onto the Arches cluster showing most of the detected sources from the 2018 C-band image not corrected for primary beam attenuation. The resolution is $0.62'' \times 0.28''$, P.A. = 2.82°. The off-source rms noise level is $4.7\,\mu\mathrm{Jy\,beam^{-1}}$. The contour levels represent 3, 5, 10, 15, 25, 35, 45, 55 and 60 times the off-source rms noise level multiplied by 3.

of the observations, because the flux density for the amplitude calibrator is the same for both epochs. We can also discard that it is related with the self-calibration procedure, because it does not change the flux density of the compact sources. We performed several tests, obtaining images with and without self-calibration, and concatenating or treating the 2016 data sets separately, but the results were the same. We also used different options for the `clean` algorithm, including wide-field clean, or multi-term multi-frequency synthesis with identical finding. We could not identify the cause of this systematic error in our data reduction, but performed a secondary calibration as follows.

First, we noted that the 2018 X-band fluxes of the radio stars AR1, AR2, AR4, AR6, AR7, and AR8 (see fifth column in Table 3.3) agreed well within their 1σ uncertainties with the 8.5 GHz flux densities (fourth column) reported by Lang et al. (2005), assuming typical values for the spectral index, which indicated that the flux calibration of the 2018 image was the correct one. Subsequently we determined a secondary flux calibration factor for the 2016 X-band data by computing the weighted mean of the flux ratios of the previously mentioned sources between the two epochs. It was 1.8 ± 0.1. We cross checked this calibration factor in two ways: On the one hand, we followed the previous procedure, but excluded all sources labelled as variable by Lang et al. (2005). With the remaining sources, AR2, AR6, and AR7, we obtained a mean flux ratio of 1.95 ± 0.17. On the other hand, we computed the weighted mean of the flux ratios of all stars detected in the 2016 and 2018 X-band images, except AR9, AR13, and AR15, which proved to be significant outliers. We found a calibration factor of 1.8 ± 0.1. After these consistency checks we applied a correction factor of 1.8 ± 0.1 to the 2016 X-band data. The re-calibrated 2016 flux densities are listed in the last column of Table 3.3.

3.3.2. Flux densities and spectral indices

The X- and C-band flux densities for all radio stars measured in our 2016 and 2018 data are listed in Table 3.4 (after secondary calibration of the 2016 X-band data, see above; the uncertainty of the calibration factor was included in the uncertainty of the reported flux densities).

Assuming the relation $S_\nu \propto \nu^\alpha$, we inferred the spectral indices of the detected radio sources from their observed X- and C-band flux densities in 2018 using the expression

$$\alpha = \frac{\log(S_{\nu_\mathrm{C}}/S_{\nu_\mathrm{X}})}{\log(\nu_\mathrm{C}/\nu_\mathrm{X})}, \tag{3.3}$$

given that only two frequencies were available. When three frequencies are available, the spectral index is usually obtained using a linear regression fit weighting each data point by its error. We derived the corresponding uncertainties to α (equa-

Table 3.3: Detected point sources in the two X-band epochs and their flux density comparison to point sources at 8.5 GHz reported by Lang et al. (2005).

Source	R.A. [a] (J2000.0)	Dec. [a] (J2000.0)	$S_{8.5\,GHz}$ (mJy)	$S_{X,\,2018}$ (mJy)	$S_{X,\,2016,\,re\text{-}calibrated}$ (mJy)
AR1	17 45 50.42 ± 0.05	−28 49 21.95 ± 0.05	1.90 ± 0.05 [b]	2.1 ± 0.3	2.2 ± 0.5
AR2	17 45 50.39 ± 0.05	−28 49 20.93 ± 0.05	0.25 ± 0.03	0.24 ± 0.04	0.23 ± 0.05
AR3	17 45 50.21 ± 0.05	−28 49 21.91 ± 0.05	0.12 ± 0.03 [b]	0.18 ± 0.03	0.17 ± 0.03
AR4	17 45 50.47 ± 0.05	−28 49 19.19 ± 0.05	0.34 ± 0.03 [b]	0.38 ± 0.06	0.37 ± 0.08
AR5	17 45 50.57 ± 0.05	−28 49 17.23 ± 0.05	0.16 ± 0.03	0.21 ± 0.03	0.24 ± 0.05
AR6	17 45 49.76 ± 0.05	−28 49 25.62 ± 0.05	0.25 ± 0.03	0.28 ± 0.04	0.22 ± 0.04
AR7	17 45 50.83 ± 0.05	−28 49 26.05 ± 0.05	0.23 ± 0.03	0.24 ± 0.04	0.25 ± 0.05
AR8	17 45 50.45 ± 0.05	−28 49 31.56 ± 0.05	0.16 ± 0.03 [b]	0.20 ± 0.03	0.22 ± 0.05
AR9	17 45 50.47 ± 0.06	−28 49 17.55 ± 0.06	0.15 ± 0.04	0.22 ± 0.03	0.06 ± 0.01
AR10	17 45 49.69 ± 0.05	−28 49 25.45 ± 0.05	0.06 ± 0.03	0.14 ± 0.02	0.16 ± 0.03
AR11	17 45 51.46 ± 0.05	−28 49 25.40 ± 0.05		0.08 ± 0.01	0.06 ± 0.01
AR12	17 45 50.68 ± 0.06	−28 49 22.25 ± 0.06		0.07 ± 0.01	0.07 ± 0.02
AR13	17 45 50.55 ± 0.05	−28 49 23.18 ± 0.05		0.16 ± 0.03	0.23 ± 0.05
AR14	17 45 50.28 ± 0.05	−28 49 16.90 ± 0.05		0.05 ± 0.01	0.09 ± 0.02
AR15	17 45 50.26 ± 0.05	−28 49 11.40 ± 0.05		0.10 ± 0.02	0.27 ± 0.06
AR16	17 45 50.53 ± 0.07	−28 49 20.26 ± 0.07			0.04 ± 0.01
AR17	17 45 48.60 ± 0.05	−28 49 42.27 ± 0.05		0.22 ± 0.03	0.23 ± 0.05
AR18	17 45 48.56 ± 0.05	−28 50 05.65 ± 0.05		0.17 ± 0.03	0.18 ± 0.04

[a] Units of right ascension are hours, minutes, and seconds, and units of declination are degrees, arcminutes, and arcseconds. Errors are in seconds and in arcseconds, respectively.

[b] Variable radio source according to Lang et al. (2005).

Table 3.4: JVLA flux densities of the compact sources detected in these observations.

Source Name [a]	Near-IR Counterpart [b]	Positions in X band (J2000.0) [c] R.A.	Dec.	Flux density (mJy) X-Band (2016)	X-Band (2018)	C-band (2018)	α	Spectral type
AR1	F6, Dong80 [d]	17 45 50.42 ± 0.05	−28 49 21.95 ± 0.05	2.2 ± 0.5	2.1 ± 0.3	2.1 ± 0.2	−0.0 ± 0.3	WN8-9h [f]
AR2	F8, Dong84	17 45 50.39 ± 0.05	−28 49 20.93 ± 0.05	0.23 ± 0.05	0.24 ± 0.04	0.14 ± 0.02	1.1 ± 0.4	WN8-9h [f]
AR3	F1, Dong85 [d]	17 45 50.21 ± 0.05	−28 49 21.91 ± 0.05	0.17 ± 0.03	0.18 ± 0.03	0.12 ± 0.01	0.8 ± 0.4	WN8-9h [f]
AR4	F7, Dong83	17 45 50.47 ± 0.05	−28 49 19.19 ± 0.05	0.37 ± 0.08	0.38 ± 0.06	0.28 ± 0.03	0.6 ± 0.4	WN8-9h [f]
AR5	F4, Dong81	17 45 50.57 ± 0.05	−28 49 17.23 ± 0.05	0.24 ± 0.05	0.21 ± 0.03	0.15 ± 0.02	0.7 ± 0.4	WN7-8h [f]
AR6	F19	17 45 49.76 ± 0.05	−28 49 25.62 ± 0.05	0.22 ± 0.04	0.28 ± 0.04	0.43 ± 0.04	−0.8 ± 0.3	O4-5 Ia [f]
AR7	F3, Dong82	17 45 50.83 ± 0.05	−28 49 26.05 ± 0.05	0.25 ± 0.05	0.24 ± 0.04	0.18 ± 0.02	0.6 ± 0.4	WN8-9h [f]
AR8	F5, Dong17 [d]	17 45 50.45 ± 0.05	−28 49 31.56 ± 0.05	0.22 ± 0.05	0.20 ± 0.03	0.16 ± 0.02	0.4 ± 0.4	WN8-9h [f]
AR9	F18, Dong83	17 45 50.47 ± 0.05	−28 49 17.55 ± 0.05	0.06 ± 0.01	0.22 ± 0.03	0.28 ± 0.03	−0.5 ± 0.3	O4-5 Ia+ [f]
AR10	F2, Dong18	17 45 49.69 ± 0.05	−28 49 25.45 ± 0.05	0.16 ± 0.03	0.14 ± 0.02	0.12 ± 0.01	0.3 ± 0.3	WN8-9h [f]
AR11	Dong79	17 45 51.46 ± 0.06	−28 49 25.40 ± 0.06	0.06 ± 0.01	0.08 ± 0.01	0.047 ± 0.008	1.0 ± 0.4	WN7 [g]
AR12	F14, Dong88	17 45 50.68 ± 0.05	−28 49 22.25 ± 0.05	0.07 ± 0.02	0.07 ± 0.01	< 0.025 [e]	> 2.0	WN8-9h [f]
AR13	F26	17 45 50.55 ± 0.05	−28 49 23.18 ± 0.05	0.23 ± 0.05	0.16 ± 0.03	< 0.020 [e]	> 4.1	O4-5 Ia [f]
AR14	F12, Dong87	17 45 50.28 ± 0.05	−28 49 16.90 ± 0.05	0.09 ± 0.02	0.05 ± 0.01	0.056 ± 0.009	−0.2 ± 0.5	WN7-8h [f]
AR15	F9, Dong86	17 45 50.26 ± 0.05	−28 49 11.40 ± 0.05	0.27 ± 0.06	0.10 ± 0.02	0.09 ± 0.01	0.2 ± 0.4	WN8-9h [f]
AR16	F16	17 45 50.53 ± 0.07	−28 49 20.26 ± 0.07	0.04 ± 0.01	< 0.037 [e]	< 0.023 [e]	> 0.9	WN8-9h [f]
AR17	Dong19	17 45 48.60 ± 0.05	−28 49 42.27 ± 0.05	0.23 ± 0.05	0.22 ± 0.03	0.15 ± 0.02	0.7 ± 0.4	WN8-9h [g]
AR18	Dong96	17 45 48.56 ± 0.05	−28 50 05.65 ± 0.05	0.18 ± 0.04	0.17 ± 0.03	0.11 ± 0.01	0.9 ± 0.4	Ofpe/WN9 [g]

[a] Nomenclature for cluster members adopted by Lang et al. (2001, 2005).

[b] Stellar identification as listed in Clark et al. (2018a) and Dong et al. (2011).

[c] Units of right ascension are hours, minutes, and seconds, and units of declination are degrees, arcminutes, and arcseconds. Errors are in seconds and in arcseconds, respectively.

[d] Variable radio source according to Lang et al. (2005).

[e] Upper limits of the undetected sources fixed from the peak of the unresolved emission.

[f] Spectral classification by Clark et al. (2018a).

[g] Spectral classification as listed in Table 3 of Dong et al. (2011).

tion 3.3 above) from standard error propagation as

$$\sigma\alpha = \frac{1}{\log\left(\nu_\mathrm{C}/\nu_\mathrm{X}\right)} \times \sqrt{\left(\frac{\sigma S_{\nu_\mathrm{X}}}{S_{\nu_\mathrm{X}}}\right)^2 + \left(\frac{\sigma S_{\nu_\mathrm{C}}}{S_{\nu_\mathrm{C}}}\right)^2} , \tag{3.4}$$

where terms preceded by σ refer to the standard deviation. The computed spectral indices and their uncertainties are listed in the second to last column of Table 3.4.

3.3.3. Mass-loss rates

Most methods to estimate the mass-loss rate (in ultraviolet, optical, or infrared regimes) suffer from the uncertainty that the derived rates depend on non-observable parameters. Nevertheless, observations of radio continuum radiation yield mass-loss rates based only on observable quantities: the radio flux density, the terminal velocity of the stellar wind, and the distance to the star. The mass-loss rates in solar masses per year can be written, in accordance with Panagia & Felli (1975) and Wright & Barlow (1975), as

$$\left[\frac{\dot{M}}{\mathrm{M_\odot\,yr^{-1}}}\right] = 5.34 \times 10^{-4} \left[\frac{S_\nu}{\mathrm{mJy}}\right]^{3/4} \left[\frac{\nu_\infty}{\mathrm{Km\,s^{-1}}}\right] \left[\frac{d}{\mathrm{kpc}}\right]^{3/2} \left[\frac{\nu}{\mathrm{Hz}}\right]^{-1/2} \left[\frac{\mu^2}{Z^2 \gamma g_\nu}\right]^{1/2} , \tag{3.5}$$

where S_ν is the flux density in milli-Janskys, ν_∞ is the terminal velocity of the stellar wind in kilometers per second, ν is the observed frequency in Hertz, and d is the distance to the observer in kiloparsecs ($\sim$ 8 kpc in our case). The parameters μ, Z, and γ are the mean molecular weight, the mean ionic charge, and the mean number of electrons per ion. We adopted the values of ν_∞ from Table 2 by Martins et al. (2008) and from their He/H values we calculated μ using the approximation

$$\mu = \frac{\sum_j n_j A_j}{\sum_j n_j} , \tag{3.6}$$

where n_j is the number density of atoms of type j, and A_j is the mass number. We only considered H and He, neglecting any other metals in the winds, and so the expression can be simplified as

$$\mu = \frac{1 + 4 \cdot \mathrm{He/H}}{1 + \mathrm{He/H}} , \tag{3.7}$$

where He/H is the ratio of H to He given in Table 2 by Martins et al. (2008). We note that AR6, AR11, AR17, and AR18 are not included in Table 2 by Martins et al. (2008), and so we adopted values of stars of similar type. Z and γ are parameters

that depend on the ionisation conditions in the wind, which leads to $Z = \gamma = 1$ in a radio-emitting region of WR stars (see Leitherer et al., 1997).

The free-free Gaunt factor, g_ν, can be obtained by means of the expression

$$g_\nu = 9.77 \cdot \left(1 + 0.13 \cdot \log \frac{T_e^{3/2}}{Z\nu} \right), \tag{3.8}$$

using the approximation by Leitherer & Robert (1991), where T_e is the electron temperature of the wind in kelvins. We assumed $T_e = 10^4$ K (deviations from this temperature had only minor effects on g_ν).

The distance of Sgr A* is known to $< 0.5\%$ (e.g. Abuter et al., 2019). As concerns the line-of-sight distance of Arches with respect to Sgr A*, we can assume that it is located within the circum molecular zone, that is $r <= 200$ pc. Therefore, assuming a 200 pc uncertainty on the distance of Sgr A* and a 200 pc uncertainty of Arches relative to Sgr A*, we get a relative uncertainty of 0.4%. This uncertainty is systematic in the sense that it affects all sources in Arches in the same way. The distribution of sources within Arches is irrelevant because we are dealing with at most a few parsecs difference. Hence, the uncertainty of d can be neglected. For the remaining parameters, we estimated the uncertainties using the same criteria as in Leitherer et al. (1997). A 10% for v_∞, and also a 10% for the free-free Gaunt factor. The assumed uncertainties for Z, γ, and μ are ± 0.08 dex. Therefore, according to the standard error propagation and defining $k = 5.34 \times 10^{-4}$, the uncertainties were obtained from

$$\alpha(\dot{M}) = \left[\frac{9}{16} \left(\frac{\dot{M}}{k \cdot S_\nu} \right)^2 (\alpha\,S_\nu)^2 + \left(\frac{\dot{M}}{k \cdot v_\infty} \right)^2 (\alpha\,v_\infty)^2 + \right.$$
$$+ \frac{9}{4} \left(\frac{\dot{M}}{k \cdot d} \right)^2 (\alpha\,d)^2 + \frac{1}{4} \left(\frac{\dot{M}}{k \cdot \nu} \right)^2 (\alpha\,\nu)^2 +$$
$$+ \left(\frac{\dot{M}}{k \cdot \mu} \right)^2 (\alpha\,\mu)^2 + 4 \left(\frac{\dot{M}}{k \cdot Z^2} \right)^2 (\alpha\,Z)^2 +$$
$$\left. + \frac{1}{4} \left(\frac{\dot{M}}{k \cdot \gamma} \right)^2 (\alpha\,\gamma)^2 + \frac{1}{4} \left(\frac{\dot{M}}{k \cdot g_\nu} \right)^2 (\alpha\,g_\nu)^2 \right]^{1/2}, \tag{3.9}$$

where terms preceded by σ also refer to the standard deviation, and we obtained a typical error of one order of magnitude less than the corresponding $\dot{M}$.

With these premises, we derived mass-loss rates corresponding to the observed flux densities at 6 and 10 GHz assuming that the observed radio emission is due to free-free emission from ionised extended envelopes with a steady and completely ionised wind, with a volume filling factor of $f = 1$, and an electron density profile of

Table 3.5: Radio mass-loss rates in the C-band (2018) and in the two X-band epochs (2016/2018).

Source	He/H [a] (#)	v_∞ [a] (Km/s)	μ [b] (#)	$\dot{M}_{2018}$ 6.0 GHz	$\dot{M}_{2016}$ 10.0 GHz	$\dot{M}_{2018}$ 10.0 GHz	$\dot{M}_{Lang\,2001}$ 8.5 GHz	$\dot{M}_{Lang\,2005}$ 22.5 GHz [c]	$\dot{M}_{Martins\,2008}$ IR K-Band [d]
AR1	0.2	1400	1.5	2.1×10^{-4}	2.1×10^{-4}	2.0×10^{-4}	2.4×10^{-4}	3.1×10^{-4}	7.6×10^{-5}
AR2	1.0	1000	2.5	3.2×10^{-5}	4.6×10^{-5}	4.9×10^{-5}	3.9×10^{-5}	4.6×10^{-5}	1.0×10^{-4}
AR3	0.1	1400	1.3	2.1×10^{-5}	2.7×10^{-5}	2.8×10^{-5}	4.5×10^{-5}	2.7×10^{-5}	6.3×10^{-5}
AR4	0.3	1300	1.7	4.7×10^{-5}	5.9×10^{-5}	5.9×10^{-5}	5.1×10^{-5}	6.2×10^{-5}	7.9×10^{-5}
AR5	0.4	1400	1.9	3.6×10^{-5}	5.0×10^{-5}	4.6×10^{-5}	4.2×10^{-5}	2.7×10^{-5}	1.4×10^{-4}
AR6	0.1	2400	1.3	9.2×10^{-5}	5.5×10^{-5}	6.8×10^{-5}	1.1×10^{-4}	7.2×10^{-5}	
AR7	0.6	800	2.1	2.6×10^{-5}	3.3×10^{-5}	3.2×10^{-5}	3.4×10^{-5}	3.4×10^{-5}	7.9×10^{-5}
AR8	0.8	900	2.3	3.0×10^{-5}	3.7×10^{-5}	3.4×10^{-5}	3.2×10^{-5}	3.3×10^{-5}	7.3×10^{-5}
AR9	0.1	2150	1.3	5.9×10^{-5}	2.0×10^{-5}	5.1×10^{-5}		4.1×10^{-5}	1.4×10^{-5}
AR10	0.35	1400	1.8	2.9×10^{-5}	3.5×10^{-5}	3.2×10^{-5}		2.7×10^{-5}	6.0×10^{-5}
AR11	0.4	1400	1.9	1.4×10^{-5}	1.9×10^{-5}	2.1×10^{-5}			
AR12	0.1	1400	1.3		1.4×10^{-5}	1.3×10^{-5}			3.2×10^{-5}
AR13	0.1	2600	1.3		6.3×10^{-5}	4.8×10^{-5}			6.0×10^{-6}
AR14	0.2	1500	1.5	1.4×10^{-5}	2.1×10^{-5}	1.4×10^{-5}			5.7×10^{-5}
AR15	0.1	1800	1.3	2.1×10^{-5}	4.9×10^{-5}	2.4×10^{-5}			5.4×10^{-5}
AR16	0.1	1400	1.3		9.0×10^{-6}				2.5×10^{-5}
AR17	0.4	1300	1.9	3.3×10^{-5}	4.6×10^{-5}	4.4×10^{-5}			
AR18	0.4	1300	1.9	2.6×10^{-5}	3.9×10^{-5}	3.6×10^{-5}			

Notes. The typical error is one order of magnitude less than the corresponding $\dot{M}$. It is shown a comparison to estimations made by Lang et al. from their 8.5 GHz observations (Lang et al., 2001) and their 22.5 GHz observations (Lang et al., 2005), both re-scaled for taking into account their assumed $v_\infty = 1000\,\mathrm{Km\,s^{-1}}$, and a comparison to estimations made by Martins et al. (2008), also re-scaled considering their clumping factor value of 0.1. All mass-loss rates, $\dot{M}$, are in units of $M_\odot\,\mathrm{yr^{-1}}$.

[a] Wind parameters from Table 2 by Martins et al. (2008).

[b] Mean molecular weight determined using the equation (5) from this paper.

[c] Derived from the 22.5 GHz flux density for AR1, AR2, AR4, AR7 and AR8 sources, and from the 8.5 GHz flux density for the others, as described in Table 5 by Lang et al. (2005).

[d] Infrared K-band obtained with the integral field spectrograph SINFONI on the VLT by Martins et al. (2008). The typical error provided is $\pm 0.2\,\mathrm{dex}$ on $\log \dot{M}$.

$n_e \propto r^{-2}$. In the case of non-thermal contributions, our values, shown in Table 3.5, represent upper limits to the true mass-loss rates.

Table 3.5 also shows the estimations done by Lang et al. from their 8.5 GHz observations (Lang et al., 2001) and their 22.5 GHz observations (Lang et al., 2005), and the estimations done by Martins et al. (2008). Lang et al. assumed a terminal velocity of the wind of 1000 Km s^{-1} for all sources, and Martins et al. adopted a volume filling factor of 0.1. Therefore, in order to compare our data with their data, we re-scaled Lang's values multiplying them by $v_\infty/1000$, where v_∞ are the values adopted in our work, and we multiplied Martins' mass-loss rates by $1/\sqrt{0.1}$ (see Abbott et al., 1981) considering the clumpling factor.

3.4. Discussion and conclusions

3.4.1. Properties of the sources

All detected sources are young, massive stars that have evolved off the main sequence, with the great majority identified as Wolf-Rayet stars of type WNh (see Table 3.4), a classification that Figer et al. (1999b, 2002) and recently Clark et al. (2018a) have assigned to most of the Arches cluster members.

Even though the uncertainties on the inferred spectral indices are relatively high, we can say that the stars AR2, AR3, AR4, AR5, AR7, AR11, AR15, AR17, and AR18 have spectral indices consistent with thermal emission from ionised stellar winds. Small deviations from the canonical value can arise from changes in the ionisation fraction along the emitting regions and/or wind structures such as clumps and/or shocks resulting from internal instabilities. The stars AR1, AR6, and AR9 have flat or inverted spectral indices, which may indicate that they are CWBs. AR10 has an inverted spectrum and is a confirmed CWB (see Lohr et al., 2018). Ambiguous cases are the stars AR8 and AR14. No measurements of α are available for the stars AR12, AR13, and AR16 because they are only detected in a single band.

AR1 and AR4 are associated with X-ray sources, where the emission is suggested to arise in shocks in their winds (Lang et al., 2005; Law & Yusef-Zadeh, 2004). Such shocks may arise in CWBs. The flat radio spectrum of AR1 (this work and Lang et al. 2005) supports this interpretation, but the close-to-thermal spectrum of AR4 (this work and Lang et al. 2005) does not provide any evidence for a CWB. Possibly, AR4 is a binary that is too tight to be identified as such by radio observations, as explained in the introduction (see section 1.2). We find no significant variability of AR1 and AR4, as could be expected for highly eccentric CWBs observed at significantly different phases of their orbits. The nature of the X-ray emission in both sources requires further investigation.

As we have two epochs with X-band measurements, we can probe variability. AR16 is the weakest stellar source detected by our observations. It lies near the crowded centre of the cluster and close to the brightest source, AR1. Its non-

detection in 2018 is therefore probably rather due to the lower quality of the 2018 data than to variability. In order to have been detectable in the 2018 data its flux would have had to increase by a factor of three in brightness (0.012 *vs.* 0.04 mJy). From the 17 sources detected in two epochs, only AR9 and AR15 display unambiguous variability with more than 5σ significance. In particular, source AR9 is labelled as a new detection in Lang et al. (2005), as compared to Lang et al. (2001). Therefore, its variability can be considered to be firmly established. We note that AR9 has a negative spectral index, and so binarity and its associated orbital motion are possible causes for its radio variability. The X-band fluxes of the other sources agree within 1σ (12 sources) or 2σ (3 sources). Lang et al. (2005) mark the four sources AR1, AR3, AR4, and AR8 as potentially variable. When we compare our measurements with theirs (propagating the 10 GHz flux densities to 8.5 GHz with the help of the measured spectral indices), we do not find any signs for variability within the uncertainties on our measurements. In conclusion, if we omit the ambiguous case of AR16, we find that only 2 of the 17 radio stars, or less than 15%, display significant variability. The radio emission therefore appears to be stable on timescales of a few to ten years.

3.4.2. Number of detected sources

All but two of the 18 radio stars detected by our study lie within a projected radius of about $R = 12.5''$ —or 0.5 pc at the distance of the GC— of the centre of the Arches cluster. It is possible that the sources far from the centre, AR17 and AR18, also originated in the cluster, a hypothesis that could be tested with proper motion measurements.

Within $R = 0.5$ pc we detect six more sources than the previous study by Lang et al. (2005). The faintest source reported by Lang et al. (2005) is AR10 as a 2σ detection with 0.06 mJy at 8.5 GHz. With the spectral indices estimated here (or assuming a flat spectral index as a conservative estimate where no measurement is available) we can estimate the 8.5 GHz flux density of the new sources found by our work. The sources AR11 (0.06 mJy), AR12 (≤ 0.07 mJy), AR14 (≤ 0.09 mJy), and AR16 (≤ 0.04 mJy) therefore probably escaped from previous detection because of the lower sensitivity of the observations. AR15 is clearly identified as a variable source by our observations (see previous subsection 3.4.1). Also, AR11 and AR15 lie outside of the FoV shown in Figure 6 of Lang et al. (2005). The relatively bright source AR13 should have been detected by Lang et al. (2005). Its non-detection may be due to variability, possibly combined with its closeness to the brightest source, AR1, which may lead to it being confused with side lobes from this source.

Does the number of detected radio sources correspond to our expectations? First of all, we detect all spectroscopically classified WR stars in the cluster (see Clark et al., 2018a). Our sample of these sources of strong ionised winds is therefore complete. The faintest source detected by the highest quality observations of our

work is AR16 with a 10 GHz flux density of 0.04 ± 0.01 mJy. Its mass-loss rate is approximately $9.0 \times 10^{-6}\,M_\odot\,\mathrm{yr}^{-1}$ or about $2.8 \times 10^{-6}\,M_\odot\,\mathrm{yr}^{-1}$ if we assume a volume filling factor of 0.1 for the stellar wind and a wind velocity of $v_\infty = 1400\,\mathrm{km\,s}^{-1}$, which are typical values for our sources.

We can estimate the number of stars with a wind mass-loss rate at or above this value by combining estimates of the age, mass, and initial mass function (IMF) of the Arches cluster with isochrones of stellar evolutionary codes. For the IMF we assume a one-segment power-law IMF, using either the standard Salpeter exponent of -2.35 or the observationally motivated top-heavy value of -1.8 (Hosek et al., 2019). The latter value is also in good agreement with the observational value of the present day mass function of the cluster within about $R = 0.5$ pc of its centre (Stolte et al., 2005). All stars that are clearly associated with the cluster, namely AR1 to AR16, are located within a projected radius of $R \approx 0.5$ pc of the cluster centre. Following Clarkson et al. (2012) and Hosek et al. (2019), we can estimate the cluster mass within this area to $1 \times 10^4\,M_\odot$ with an approximate uncertainty of 30%. Using PARSEC (release v1.2S + COLIBRI S_35, Bressan et al., 2012a; Chen et al., 2014a, 2015b; Tang et al., 2014a; Marigo et al., 2017a; Pastorelli et al., 2019a) and MIST (Dotter, 2016; Choi et al., 2016; Paxton et al., 2011a, 2013, 2015) theoretical isochrones for solar metallicity we can estimate the number of stars with a mass-loss rate of $\gtrsim 9.0 \times 10^{-6}\,M_\odot\,\mathrm{yr}^{-1}$ ($\gtrsim 2.8 \times 10^{-6}\,M_\odot\,\mathrm{yr}^{-1}$ for a 0.1 volume filling factor) in this area.

Table 3.6 lists this number for the two IMF slopes assumed here, for five different cluster ages, for the two theoretical models, and for assuming volume filling factors of 1 and 0.1. In each case, the numbers are the means and standard deviations from 100 runs of a Monte Carlo simulation. The numbers for MIST and PARSEC agree within their estimated uncertainties. The assumed volume filling factor has little impact at ages of 4 and 5 Myr, but can increase the numbers of detected stars considerably at lower ages.

Comparing the numbers in Table 3.6 with the number of detected radio stars in our observations, either 16 or 18, the latter if we assume that AR17 and AR18 may be high-mass stars that escaped from the cluster, we can see that an age as old as 5 Myr can be safely ruled out. The numbers clearly also require a top-heavy IMF; they indicate an age of the cluster in the range $2-4$ Myr. This agrees well with the observational values of the age range: from 3.7 ± 0.2 Myr (Hosek et al., 2019) and 3.7 ± 0.7 Myr (Schneider, 2014) on the high end, to lower estimates of around $2.0-3.3$ Myr (e.g. Clark et al., 2018a; Lohr et al., 2018).

Our age estimation is relatively crude because it relies on various assumptions —among others the validity of theoretical codes for the post-main sequence evolution of massive stars— and ignores complications such as the influence of stellar multiplicity on stellar evolution. Nevertheless, our estimate shows that the number of radio stars can be used as a tool to constrain the age or mass of a cluster and also

its mass function. We also show that the theoretical models appear to satisfactorily represent mass-loss rates of massive stars.

3

Table 3.6: Expected number of stars detected at 10 GHz within cylindrical beam of $R = 0.5$ pc, assuming a mass of 1×10^4 M$_\odot$, a volume filling factor of 1, different ages and two different slopes α_{IMF} of the initial mass function. The numbers in brackets correspond to the assumption of a volume filling factor of 0.1 for the stellar wind.

Age (Myr)	2	3	4	5
PARSEC				
$\alpha_{IMF} = -2.35$	1.4 ± 1.2 (7.7 ± 2.6)	4.7 ± 2.0 (6.4 ± 2.3)	5.6 ± 2.7 (5.9 ± 2.7)	3.4 ± 1.7 (5.6 ± 2.4)
$\alpha_{IMF} = -1.8$	5.7 ± 2.1 (26.2 ± 4.8)	17.6 ± 4.0 (22.6 ± 4.6)	15.3 ± 3.7 (16.2 ± 3.9)	7.9 ± 2.8 (12.8 ± 3.4)
MIST				
$\alpha_{IMF} = -2.35$	2.5 ± 1.7 (8.1 ± 3.2)	5.8 ± 2.4 (9.6 ± 3.5)	3.3 ± 2.0 (3.5 ± 2.0)	3.1 ± 1.8 (3.1 ± 1.8)
$\alpha_{IMF} = -1.8$	9.6 ± 3.1 (27.1 ± 4.5)	20.6 ± 4.2 (31.4 ± 5.3)	10.1 ± 3.1 (10.5 ± 3.1)	7.8 ± 2.9 (7.9 ± 2.8)

4

The Quintuplet cluster

*Lo que embellece al desierto –dijo el principito–
es que esconde un pozo en cualquier parte...*

El Principito
Antoine de Saint-Exupéry

4.1. Introduction

The Quintuplet cluster is a young, massive stellar cluster in the Galactic centre region, along with the Arches and the Central Parsec clusters. Separated by just a few arcminutes from the Arches cluster, the Quintuplet cluster is located at a projected distance of approximately 30 pc (or 12.5′ in angular distance) to the northeast of Sg A*, the black hole and the centre of our Galaxy.

It owes its name to five prominent infrared-bright sources, named Q1, Q2, Q3, Q4 and Q9 by Figer et al. (1999b) (see figure 4.1).

The Quintuplet cluster has a similar mass as the Arches cluster, about $1 - 2 \times 10^4\,M_\odot$ (Figer et al., 1999b; Rui et al., 2019), but is considered to be roughly 1 Myr older than the former (Arches: $2.5 - 4$ Myr, Quintuplet: $3 - 5$ Myr; Figer et al., 1999b; Clark et al., 2018a; Clark et al., 2018b; Schneider, 2014), which is reflected in its larger core radius – probably a sign of its ongoing dissolution in the GC tidal field (Rui et al., 2019) – and its content of more evolved stars than the Arches (Clark et al., 2018b).

Lang et al. (2005) carried out a multi-frequency, multi-configuration, and multi-epoch study of the Arches and Quintuplet clusters with the VLA. They identified ten more or less compact radio sources. The majority of them had rising indices as

expected for young massive stars with powerful stellar winds and a few of them had clear near-infrared counterparts.

In this chapter, we study the Quintuplet from our own observations obtained with the JVLA taking advantage of its significantly increased sensitivity in comparison with the old VLA.
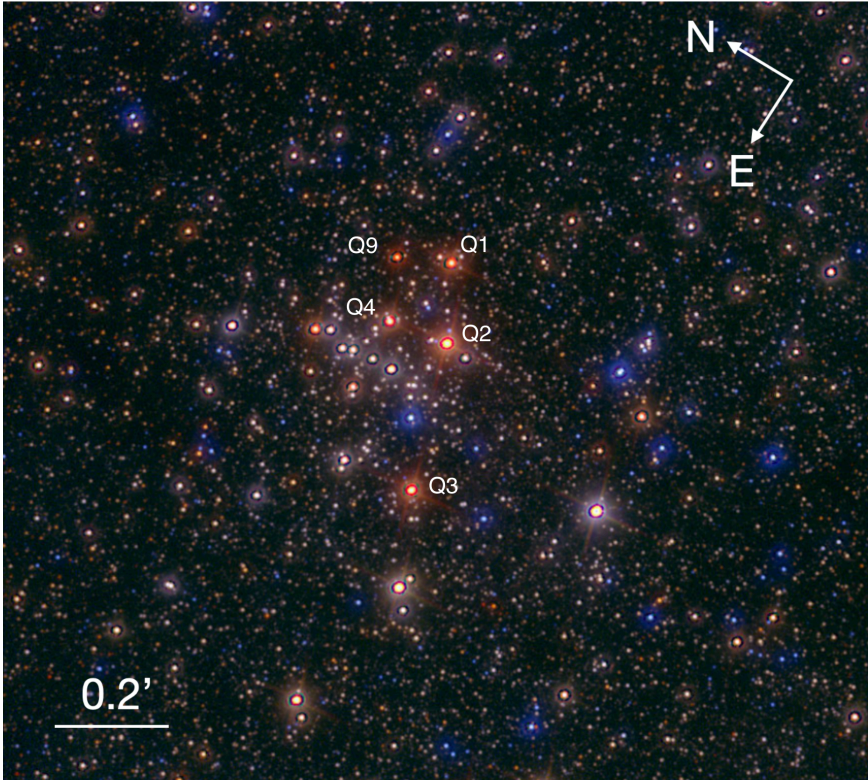

Figure 4.1: GALACTICNUCLEUS region corresponding to the Quintuplet cluster. Credits: Nogueras-Lara et al. (2018, 2019a), publications in which the author of this thesis, Aurelia Teresa Gallego Calvente, is co-author.

4.2. Observations and imaging

We observed the radio continuum emission from the Quintuplet cluster using the JVLA of NRAO in 2016 and 2018. We obtained data in four epochs, two of them in 2016 and the other two in 2018. In 2016 we obtained data just in the X-band (3.0 cm or a representative frequency of 10 GHz), and in 2018 in the C- (5.0 cm or 6 GHz) and X-bands. The phase centre was taken at the position α, $\delta_{(J2000)}$ = $17^h 46^m 15.26^s$, $-28° 49' 33.0''$. All the observations were done in the A configuration of the JVLA to achieve the highest angular resolution. This configuration also helped

Table 4.1: Observational properties

Observation date	Band [a]	JVLA configuration	On source time (minutes)
Oct 04, 2016	X	A	55
Oct 27, 2016	X	A	55
Mar 24, 2018	X	A	55
Jun 10, 2018	C	A	74

[a] Frequency range of $8 - 12$ GHz for X-band and $4 - 8$ GHz for C-band. Therefore, the total bandwidth was 4 GHz on each band. The number of spectral windows was 32 and the number of channels 64 in both cases.

4

us to filter out part of the extended emission that surrounds the Quintuplet cluster whose center is located at a few arcminutes to the southeast of the Sickle H II region (G0.18−0.04) and at approximately 10″ due north of the Pistol (G0.15−0.05) H II region. Table 4.1 gives all the details of the observations.

J1744−3116 was used as phase calibrator and J1331+305 (3C286) as band-pass and flux density calibrator at all frequencies. The raw data were processed automatically performing an initial flagging and calibration through the JVLA calibration pipeline. Extra flagging was necessary to remove the lost or corrupted data.

A very bright source was present in the FoV in both bands. This source is located at $\alpha, \delta_{(J2000)} = 17^h\, 46^m\, 21.04^s, -28° 50' 03.11''$. We identified it as SgrA−N3 using the VizieR Catalogue Service[1]. We carried out data reduction with CASA as follows.

We used the task `tclean` to create a model for the intense source in order to, later on, self-calibrate on this source. The $u - v$ range was constrained to frequencies greater than 200 kλ to filter out some of the extended emission near and around the target field. These two steps, that is model generation and calibration of the time-dependent antenna-based gains on the bright source, were repeated several times, thereby iteratively changing the parameter that controls the solution interval, `solint`, in the `gaincal` task. An improvement of 15% in the dynamic range was achieved through this iterative approach. We inserted the final model by means of the task `ft` from CASA. Since the diffraction pattern of the bright (~ 40 mJy) SgrA-N3 source interfered with our aim to detect faint sources, we subtracted it in the Fourier plane. Subsequently, we cleaned our new visibility data set, stored in a new table as a `Measurement Set` (`MS`), using `tclean` in interactive mode. We chose the interactive mode because the subtraction of SgrA-N3 was not completely perfect and the restriction of the $u - v$ range did not entirely remove the extended emission.

We tried to improve the images in all epochs through testing the more advanced form of imaging `multi-scale clean`, that distinguishes scales between point sources and extended emission. Its use did not improve the quality of the final

---

images. Additionally, we probed different weighting schemes to correct for visibility sampling effects. The natural weighting scheme resulted in the images with the highest signal-to-noise. The gain parameter in the clean algorithm was set to 0.05, which helped with dealing with the remnants of the diffuse emission. With this procedure we reached an off-source rms noise level of $4.3\,\mu$Jy beam^{-1} in the 2016 X-band image. The off-source thermal noise reached in the 2018 epochs was 5.7 and $6.6\,\mu$Jy beam^{-1} for X- and C-bands, respectively.

All the images were primary beam corrected to account for the change in sensitivity across the primary beam. Table 4.2 summarises the properties of the final images.

Table 4.2: Properties of the images

Epoch	Band	Frequency [a] (GHz)	Synthesised beam (arcsec × arcsec)	P. A. [b] (degrees)	rms noise [c] (μJy beam^{-1})	(u, v) cut-off (kλ)	Θ_{LAS} [d] (arcsec)
2016	X	10.0	0.47 × 0.15	25.29	4.3	200	5.3
2018	X	10.0	0.41 × 0.16	−6.84	5.7	200	5.3
2018	C	6.0	0.62 × 0.21	19.97	6.6	200	8.9

[a] Representative frequency, in Gigahertz.
[b] The position angle (P. A.) of the fitted major axis for the synthesised beam, in degrees.
[c] Off-source root mean square noise level reached.
[d] Largest Angular Scale, Θ_{LAS}: Scale at which severe attenuation of large-scale structure occurs (in arcseconds).

4.3. Results

4.3.1. Point source detection and flux density

Point sources were selected interactively in the cleaning procedure, as we specified in section 4.2, restricting ourselves to those at above five times the off-source rms noise level.

We used the image-plane component fitting (`imfit`) task from CASA that takes into account the quality of the fit and each image rms, to estimate the positions of the maxima, the total flux densities, and the errors of these values over the final primary-beam-corrected images for all bands in all epochs. We added in quadrature to the formal error of the fit, $0.5\,\theta/$SNR (Reid et al., 1988), a systematic error of 0.05″(Dzib et al., 2017), to get the uncertainties in positions. In the formal error, θ is the source size convolved with the beam and SNR the S/N (review equation 3.1). The systematic error address the thermal noise and uncertainties introduced by the phase calibration process.

Likewise, we considered the percentage in the calibration error of the peak flux densities at the frequencies observed (Perley & Butler, 2013) and the factor that notes whether a source is resolved or unresolved to evaluate the flux-density uncertainties

(revisit equation 3.2).

This process led us to detect 29 and 28 point sources above $5\,\sigma$ at 10 GHz and 6 GHz, respectively. Figure 4.2 shows a closeup onto the 2016 X-band image and a closeup onto the 2018 C-band image of the cluster, both images corrected for primary beam attenuation, with radio stars labelled. We note that some of the detected point sources lie outside of the field-of-view shown in the Figure.

The 2016 X-band image turned out to be the image with the highest S/N, so it provides the most complete list of point sources. Besides the rms noise, there is systematic noise present in the radio image, caused by remnant side lobes of SgrA-N3, because it could not be removed from the image perfectly, as well as from all the other sources, due to the limited (u, v) space coverage that resulted from the short integration time. Also, the Quintuplet region is full of ionised gas in clouds of variable compactness. The systematic noise and the ionised gas can give rise to numerous spurious detections, even at $5\,\sigma$ above the rms noise. Therefore, we compared the positions of detected radio point sources in our 2016 X-band image with the positions of stars on an HST/WFC3 F153M image of the Quintuplet cluster (Rui et al., 2019), downloaded from the HST archive[2]. All radio stars must necessarily be very bright infrared sources (massive, young stars) that care detected at S/N ratios exceeding a few times 100. Only sources coincident within 0.05'' with the position of stars detected in the NIR were accepted as real. The tagged HST/WFC3 F153M image is shown in Fig. 4.3.

Finally, we matched our sources with the ones provided by (Clark et al., 2018b, Tables A.1 and A.2), based on HST/NICMOS+WFC3 photometry and VLT/SINFONI+ KMOS spectroscopy for ~ 100 and 71 cluster members, respectively. In this way we could obtain the spectral type of the radio stars.

Lang et al. in 2005 reported nine compact radio sources and the Pistol Star. They referred to the former as QR1−QR9. QR1−3 were interpreted as the first detections of embedded massive stars in the Quintuplet cluster. As we can observe in Fig. 4.3, those sources have no bright, stellar NIR counterparts, as was clearly indicated by Lang et al. (2005) as well. To further investigate these sources, we superposed the HST/WFC3 F153M image from HST archive with a Paschen α image by Dong et al. (2011), see Figure 4.4. From this figure we can see that QR1−3 are not stellar sources but related to ionised gas clouds that have similar appearance as many other such objects in this region.

Considering this finding, we have renamed the Quintuplet cluster members to reassign a number to the detected radio sources from #1 to #29. We do not use the prefix QR used by Lang et al. (2005) to avoid confusion between the old QR1−3 and the new 1−3 numbered members. We confirm seven sources reported by Lang

---

[2]Based on observations made with the NASA/ESA Hubble Space Telescope, obtained from the data archive at the Space Telescope Science Institute. STScI is operated by the Association of Universities for Research in Astronomy, Inc. under NASA contract NAS 5-26555.
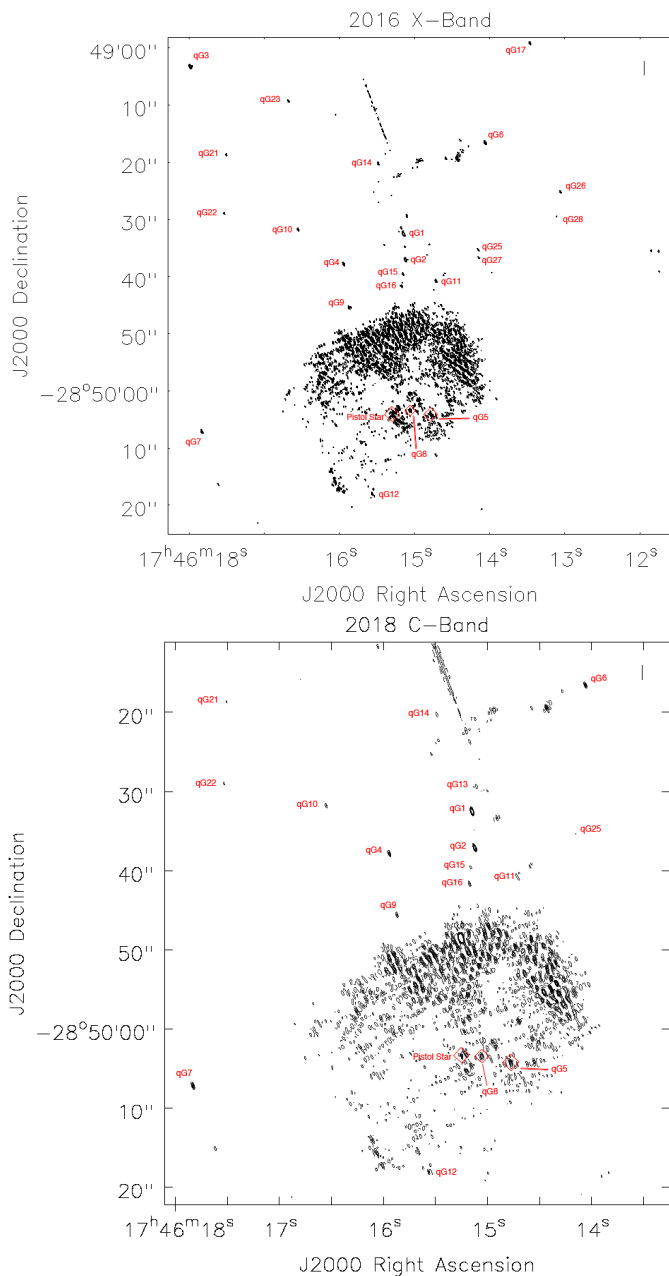
Figure 4.2: Top: Closeup onto the Quintuplet cluster from the 2016 X-band image corrected for primary beam attenuation. The clean beam is $0.47'' \times 0.15''$, P.A. = 25.29°. The off-source rms noise level is $4.3\,\mu$Jy beam^{-1}. The contour levels represent -1, 1, 2, 3, 4, 5, and 6 times $5\,\sigma$. Bottom: Closeup onto the Quintuplet cluster showing most of the detected sources from the 2018 C-band image corrected for primary beam attenuation. The resolution is $0.41'' \times 0.16''$, P.A. = −6.84°. The off-source rms noise level is $5.7\,\mu$Jy beam^{-1}. The contour levels represent -1, 1, 2, 3, 4, 5, and 6 times $5\,\sigma$.
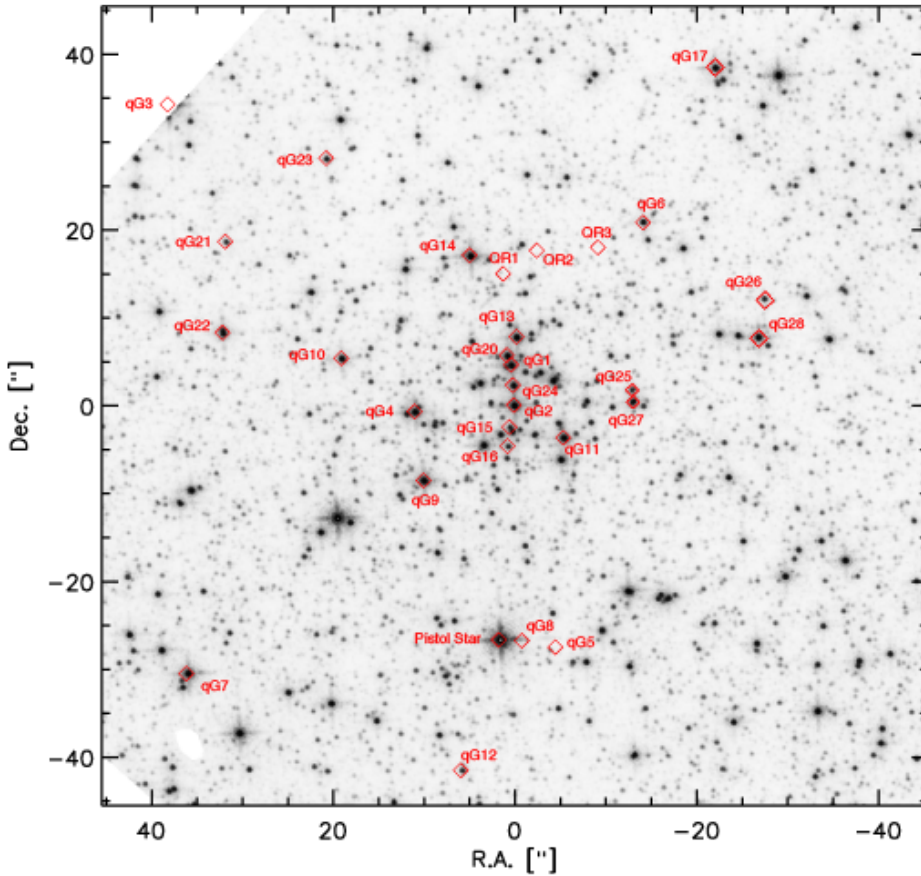
Figure 4.3: HST/WFC3 F153M image of the Quintuplet cluster with identified radio stars labelled.

et al. (2005) as radio stars (QR4, QR5, QR6, QR7, QR8, QR9, Pistol Star). With a total of 29 sources reported here, this work quadruples the number of known radio stars associated with the Quintuplet cluster.

Table 4.3 shows the new and the old nomenclature, the identified NIR counterparts as listed in Clark et al. (2018b), determined positions, the X- and C-band flux densities for all radio sources measured in our 2016 and 2018 data sets or the upper limits of the undetected sources, and the spectral classification according to Clark et al. (2018b).

4.3.2. Spectral indices

We calculated the spectral indices (or otherwise their limits) of the radio stars, as well as the corresponding uncertainties using their measured X- and C-band fluxes. We proceeded as described in Gallego-Calvente et al. (2021). The spectral indices
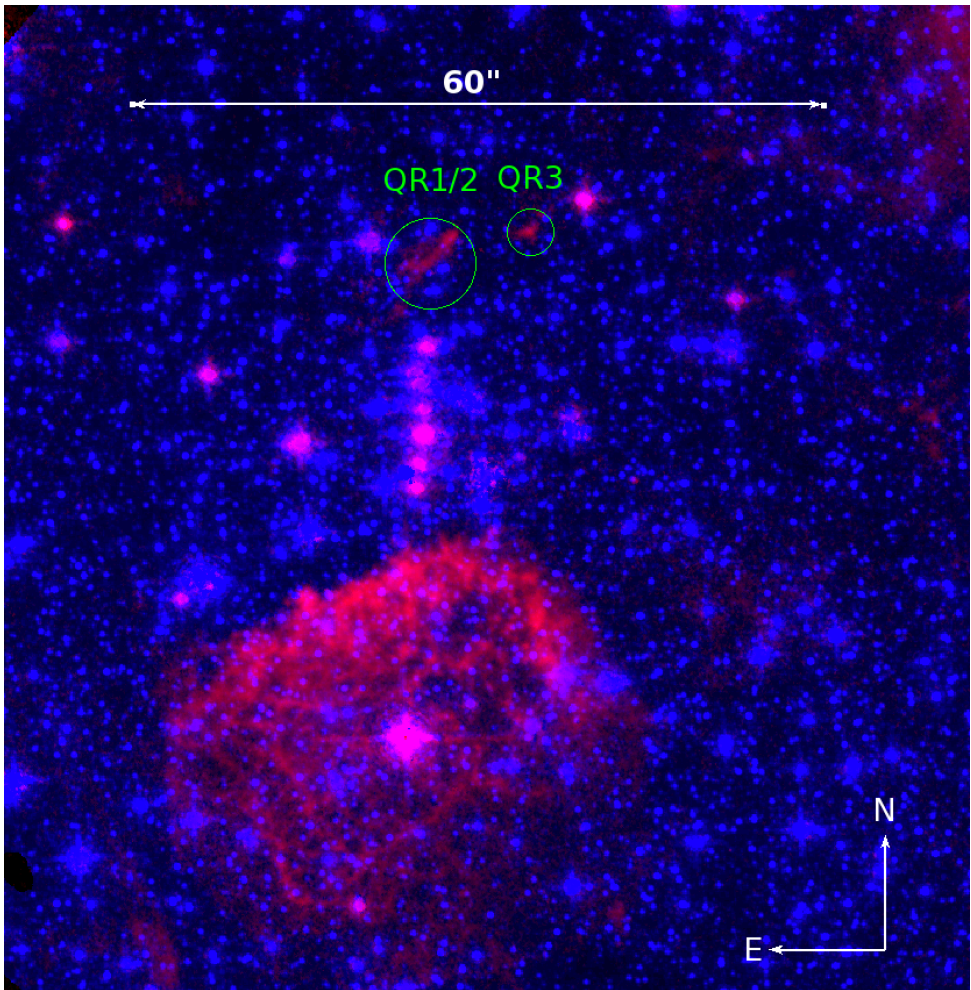
Figure 4.4: Composition of the HST/WFC3 F153M image from HST archive with a Paschen α image by Dong et al. (2011). BLue: HST WFC3 F153M; Red: HST NIC3 Paschen α. QR1−3 sources by Lang et al. (2005) are encircled.

are listed in column 8 of Table 4.3.

4.3.3. Mass-loss rates

We determined the mass-loss rates for the detected radio stars following the recipe described in Gallego-Calvente et al. (2021) and in chapter 3 of this PhD. We derived mass-loss rates corresponding to the observed flux densities at 6 and 10 GHz assuming that the observed radio emission is due to free-free emission from ionised extended envelopes with a steady and completely ionised wind, with a volume filling

Table 4.3: JVLA flux densities of the compact sources of the Quintuplet cluster from these observations.

Source name	Near-IR counterpart [b]	Positions in X band (J2000.0) [c]		Flux density (mJy) [d]			α	Spectral type [f]
		R.A.	Dec.	X-Band (2016)	X-Band (2018)	C-band (2018)		
qG1 (QR6 [a])	qF257, LHO096	17 46 15.14 ± 0.01	−28 49 32.46 ± 0.01	1.1 ± 0.1	0.49 ± 0.05	0.45 ± 0.05	0.2 ± 0.3	B1-2 Ia+
qG2 (QR5 [a])	qF241, LHO071	17 46 15.12 ± 0.01	−28 49 37.00 ± 0.01	0.50 ± 0.05	0.52 ± 0.05	0.34 ± 0.03	0.8 ± 0.3	WN11h
qG3 (QR9 [a])	qF362	17 46 17.98 ± 0.01	−28 49 03.20 ± 0.01	0.40 ± 0.04	0.50 ± 0.05	0.17 ± 0.02	2.1 ± 0.3	LBV
Pistol Star [a]	qF134	17 46 15.24 ± 0.01	−28 50 03.37 ± 0.01	0.26 ± 0.03	0.34 ± 0.03	0.10 ± 0.01	2.4 ± 0.3	LBV
qG4	qF240, LHO067	17 46 15.94 ± 0.01	−28 49 37.73 ± 0.01	0.23 ± 0.02	0.21 ± 0.02	0.14 ± 0.02	0.8 ± 0.3	WN10h
qG5		17 46 14.77 ± 0.01	−28 50 04.20 ± 0.01	0.23 ± 0.02	0.19 ± 0.02	0.30 ± 0.03	−0.9 ± 0.3	<B0 I
qG6 (QR8 [a])	qF320, LHO158	17 46 14.05 ± 0.01	−28 49 16.47 ± 0.01	0.22 ± 0.02	0.22 ± 0.02	0.16 ± 0.02	0.6 ± 0.3	WN9h
qG7		17 46 17.83 ± 0.01	−28 50 07.16 ± 0.01	0.17 ± 0.02	0.18 ± 0.02	0.20 ± 0.02	−0.2 ± 0.3	O7-8 Ia+/WNLh
qG8		17 46 15.05 ± 0.01	−28 50 03.47 ± 0.01	0.15 ± 0.02	0.23 ± 0.02	0.20 ± 0.02	0.3 ± 0.3	WC8-9(d? (+OB)
qG9	qF211, LHO019	17 46 15.87 ± 0.01	−28 49 45.46 ± 0.01	0.12 ± 0.01	0.10 ± 0.01	0.09 ± 0.01	0.2 ± 0.3	WC9d (+OB)
qG10	qF256, LHO099	17 46 16.55 ± 0.01	−28 49 31.73 ± 0.01	0.12 ± 0.01	0.09 ± 0.01	0.060 ± 0.009	0.8 ± 0.4	WN8-9ha
qG11 (QR7 [a])	qF231, LHO042	17 46 14.71 ± 0.01	−28 49 40.65 ± 0.01	0.10 ± 0.01	0.070 ± 0.009	0.09 ± 0.01	−0.5 ± 0.3	WC9d(+OB)
qG12		17 46 15.56 ± 0.01	−28 50 18.05 ± 0.01	0.10 ± 0.01	0.17 ± 0.02	0.07 ± 0.01	1.7 ± 0.4	O7-8 Ia
qG13 (QR4 [a])	qF270S, LHO110	17 46 15.10 ± 0.01	−28 49 29.31 ± 0.01	0.09 ± 0.01	0.08 ± 0.01	0.060 ± 0.009	0.6 ± 0.4	B1-2 Ia+/WNLh
qG14	qF307A, LHO146	17 46 15.48 ± 0.01	−28 49 20.17 ± 0.01	0.09 ± 0.01	0.09 ± 0.01	0.07 ± 0.01	0.5 ± 0.4	B1-2 Ia+
qG15	qF235N, LHO047	17 46 15.15 ± 0.02	−28 49 39.47 ± 0.02	0.080 ± 0.009	0.08 ± 0.01	0.050 ± 0.009	0.9 ± 0.4	WC8(d? +OB?)
qG16	qF235S, LHO034	17 46 15.17 ± 0.01	−28 49 41.61 ± 0.01	0.080 ± 0.009	0.10 ± 0.01	0.09 ± 0.01	0.2 ± 0.3	WC8(d? +OB?)
qG17	qF381	17 46 13.45 ± 0.01	−28 48 59.12 ± 0.01	0.074 ± 0.008	0.07 ± 0.03	0.040 ± 0.008	1.1 ± 0.9	B0-1 Ia+/WNLh
qG18	qF353E	17 46 11.13 ± 0.01	−28 49 05.85 ± 0.01	0.072 ± 0.008	0.07 ± 0.03	0.030 ± 0.008	2 ± 1	WN6
qG19		17 46 16.50 ± 0.01	−28 48 44.08 ± 0.01	0.060 ± 0.007	0.060 ± 0.009	0.08 ± 0.01	−0.6 ± 0.4	

Continued on next page...

[a] Nomenclature for cluster members adopted by Lang et al. (2005).

[b] Stellar identification as listed in Clark et al. (2018b) according to Figer et al. (1999b) and Liermann et al. (2009).

[c] Units of right ascension are hours, minutes, and seconds, and units of declination are degrees, arcminutes, and arcseconds. Errors are in seconds and in arcseconds, respectively.

[d] Flux densities measured from images corrected for primary beam attenuation.

[e] Upper limit of the undetected source was fixed as 2 times the off-source rms noise level.

[f] Spectral classification by Clark et al. (2018b).

Table 4.3: – continued from previous page

Source name	Near-IR counterpart [b]	Positions in X band (J2000.0) [c]		Flux density (mJy) [d]			α	Spectral type [f]
		R.A.	Dec.	X-Band (2016)	X-Band (2018)	C-band (2018)		
qG20	LHO100	17 46 15.18 ± 0.02	−28 49 31.39 ± 0.02	0.060 ± 0.007	0.023 ± 0.006	0.04 ± 0.01	−1.1 ± 0.7	B2-3Ia⁺
qG21	qF309	17 46 17.50 ± 0.02	−28 49 18.61 ± 0.02	0.050 ± 0.007	0.050 ± 0.008	0.04 ± 0.01	0.4 ± 0.6	WC8-9(d? +OB?)
qG22	qF274	17 46 17.53 ± 0.02	−28 49 28.87 ± 0.02	0.050 ± 0.007	0.050 ± 0.008	0.04 ± 0.01	0.4 ± 0.6	WN8-9ha
qG23	qF344	17 46 16.67 ± 0.02	−28 49 09.24 ± 0.02	0.050 ± 0.007	0.060 ± 0.008	0.04 ± 0.01	0.8 ± 0.6	O7-8 Ia
qG24	qF278, LHO077	17 46 15.12 ± 0.02	−28 49 34.75 ± 0.02	0.050 ± 0.006	0.060 ± 0.009	0.03 ± 0.01	1.4 ± 0.7	B0-1 Ia⁺
qG25	LHO076	17 46 14.14 ± 0.02	−28 49 35.26 ± 0.02	0.050 ± 0.006	0.037 ± 0.007	0.030 ± 0.008	0.4 ± 0.6	WC9d(+OB)
qG26	WR 102ca	17 46 13.05 ± 0.02	−28 49 25.10 ± 0.02	0.044 ± 0.006	0.040 ± 0.007	0.030 ± 0.008	0.6 ± 0.6	WC9d(+OB)
qG27	qF243, LHO075	17 46 14.13 ± 0.03	−28 49 36.60 ± 0.03	0.032 ± 0.005	0.030 ± 0.007	0.020 ± 0.008	0.8 ± 0.9	WC9d(+OB)
qG28		17 46 13.09 ± 0.03	−28 49 29.42 ± 0.03	0.031 ± 0.005	0.030 ± 0.007	< 0.0132 [e]	> 1.6	
qG29		17 46 09.69 ± 0.02	−28 49 39.36 ± 0.02	0.080 ± 0.009	0.17 ± 0.02	0.15 ± 0.02	0.2 ± 0.3	

[a] Nomenclature for cluster members adopted by Lang et al. (2005).

[b] Stellar identification as listed in Clark et al. (2018b) according to Figer et al. (1999b) and Liermann et al. (2009).

[c] Units of right ascension are hours, minutes, and seconds, and units of declination are degrees, arcminutes, and arcseconds. Errors are in seconds and in arcseconds, respectively.

[d] Flux densities measured from images corrected for primary beam attenuation.

[e] Upper limit of the undetected source was fixed as 2 times the off-source rms noise level.

[f] Spectral classification by Clark et al. (2018b).

factor $f = 1$, and an electron density profile $n_e \propto r^{-2}$. In the case of non-thermal contributions our values, showed in Table 4.4, represent upper limits to the true mass-loss rates.

For most Quintuplet cluster members, we can assume that helium stays singly ionised in the radio emitting region of the stellar wind, so the number of free electrons per ion and the mean ionic charge can be set $\gamma = 1 = Z$ (Leitherer et al., 1997). However, in the case of Pistol Star and qG3 (the two LBVs) accounting for the fact that helium is predominantly neutral in the winds of these cool stars, we take $\gamma = 0.8$, and $Z = 0.9$ similarly to other LBVs studies (e.g. Leitherer et al., 1995; Agliozzo et al., 2019).

Table 4.4 also shows the estimations done by Lang et al. from their 22.5 GHz flux densities when possible, and otherwise from their 8.5 GHz flux densities (see Lang et al., 2005). They used their higher frequency observations as better tracer of the thermal component and so give more reliable mass-loss rates because contamination of the flux density by the non-thermal component can occur at the lower frequencies (according to Contreras et al. 1996). Lang et al. (2005) assumed a terminal wind velocity of 1000 Km s^{-1} and a mean molecular weight equal to 2 for all sources. Thus, in order to compare our data with their data, we have re-scaled Lang's values multiplying them by $v_\infty/1000$ and $\mu/2$, where v_∞ and μ are the values adopted in this work. We derived a significantly lower mass-loss rate for the Pistol star than Lang et al. (2005) because the latter work reports a roughly ten times higher flux density for this source. This may be explained through variability of the source (see below) or, possibly also, the lower angular resolution of the observations of Lang et al. (2005) which may have resulted in flux of the Pistol nebula, in which the Pistol Star is embedded, having contaminated their measurements. Similar factor ~ 10 discrepancies exist for the sources qG13/QR4 and qG11/QR7.

4.4. Properties of the sources

According to the spectral classification, most of detected sources in the Quintuplet cluster are young, massive, post-main sequence stars, being the majority of Wolf-Rayet spectral type (see Table 4.3). In particular, two luminous blue variable, eight WC, six WN, seven B supergiants and three sources of type O Ia have been found.

After considering the inferred spectral indices, even though the corresponding uncertainties are relatively high, we can say that qG1, qG2, qG4, qG6, qG9, qG10, qG12−15, qG17, qG18, and qG21−27 have spectral indices consistent with thermal emission from ionised stellar winds. The divergence of α from the canonical value of 0.6 can occur from a number of reasons, such as deviations in the wind conditions maybe by the presence of condensations (*clumps*) that produce a nonstandard electron density profile ($n_e \propto r^{-s}$, with $s \neq 2$) and/or changes in the run of ionisation or wind geometry with radius due to internal shocks. Leitherer et al. (1997) suggested that there is little variation in the mass-loss rates for Wolf-Rayet

Table 4.4: Radio mass-loss rates in the C-band (2018) and in the two X-band epochs (2016/2018).

Source	Spectral type [b]	v_∞ [c] (Km/s)	μ [c] (#)	$\dot{M}_{2018}$ 6.0GHz	$\dot{M}_{2016}$ 10.0GHz	$\dot{M}_{2018}$ 10.0GHz	$\dot{M}_{Lang2005}$ [d] 22.5GHz
qG1 (QR6 [a])	B1-2 Ia+	500	1.3	$(2.0 \pm 0.4) \times 10^{-5}$	$(3.8 \pm 0.8) \times 10^{-5}$	$(2.1 \pm 0.5) \times 10^{-5}$	1.2×10^{-5}
qG2 (QR5 [a])	WN11h	300	1.8	$(1.3 \pm 0.3) \times 10^{-5}$	$(1.8 \pm 0.4) \times 10^{-5}$	$(1.8 \pm 0.4) \times 10^{-5}$	3.0×10^{-5}
qG3 (QR9 [a])	LBV	170	1.9	$(5.9 \pm 1.3) \times 10^{-6}$	$(1.1 \pm 0.2) \times 10^{-5}$	$(1.3 \pm 0.3) \times 10^{-5}$	5.2×10^{-6}
Pistol Star	LBV	105	2.2	$(2.8 \pm 0.6) \times 10^{-6}$	$(5.8 \pm 1.0) \times 10^{-6}$	$(7.1 \pm 1.0) \times 10^{-6}$	3.1×10^{-5}
qG4	WN10h	400	1.8	$(9.2 \pm 2.0) \times 10^{-6}$	$(1.3 \pm 0.3) \times 10^{-5}$	$(1.2 \pm 0.3) \times 10^{-5}$	
qG5	<B0 I	500	1.3	$(1.5 \pm 0.3) \times 10^{-5}$	$(1.2 \pm 0.3) \times 10^{-5}$	$(1.0 \pm 0.2) \times 10^{-5}$	
qG6 (QR8 [a])	WN9h	700	2.78	$(2.7 \pm 0.6) \times 10^{-5}$	$(3.5 \pm 0.7) \times 10^{-5}$	$(3.5 \pm 0.7) \times 10^{-5}$	4.2×10^{-5}
qG7	O7-8 Ia+/WNLh	1500	1.3	$(3.3 \pm 0.7) \times 10^{-5}$	$(2.9 \pm 0.6) \times 10^{-5}$	$(3.0 \pm 0.7) \times 10^{-5}$	
qG8	WC8-9(d? + OB?)	1250	4.7	$(9.8 \pm 2.0) \times 10^{-5}$	$(7.9 \pm 2.0) \times 10^{-5}$	$(1.1 \pm 0.2) \times 10^{-4}$	
qG9	WC9d (+OB)	1250	4.7	$(5.4 \pm 1.0) \times 10^{-5}$	$(6.7 \pm 1.0) \times 10^{-5}$	$(5.8 \pm 1.0) \times 10^{-5}$	
qG10	WN8-9ha	900	2.0	$(1.2 \pm 0.3) \times 10^{-5}$	$(2.0 \pm 0.4) \times 10^{-5}$	$(1.7 \pm 0.4) \times 10^{-5}$	
qG11 (QR7 [a])	WC9d(+OB)	1250	4.7	$(5.4 \pm 1.0) \times 10^{-5}$	$(5.8 \pm 1.0) \times 10^{-5}$	$(4.5 \pm 1.0) \times 10^{-5}$	2.8×10^{-4}
qG12	O7-8 Ia	1500	1.3	$(1.5 \pm 0.3) \times 10^{-5}$	$(1.9 \pm 0.4) \times 10^{-5}$	$(2.3 \pm 0.5) \times 10^{-5}$	
qG13 (QR4 [a])	B1-2 Ia+/WNLh	300	1.3	$(2.6 \pm 0.6) \times 10^{-6}$	$(3.6 \pm 0.8) \times 10^{-6}$	$(3.3 \pm 0.7) \times 10^{-6}$	2.9×10^{-5}
qG14	B1-2 Ia+	500	1.3	$(4.9 \pm 1.0) \times 10^{-6}$	$(6.0 \pm 1.0) \times 10^{-6}$	$(6.0 \pm 1.0) \times 10^{-6}$	
qG15	WC8(d? +OB?)	1250	4.7	$(3.5 \pm 0.7) \times 10^{-5}$	$(4.9 \pm 1.0) \times 10^{-5}$	$(4.9 \pm 1.0) \times 10^{-5}$	

Notes. It is shown a comparison to estimations done by (Lang et al., 2005) from their 22.5 GHz and their 8.5 GHz observations, re-scaled for taking into account their assumed v_∞ = 1000 Km s^{-1} and μ = 2. All mass-loss rates, $\dot{M}$, are in units of M$_\odot$ yr^{-1}.

a. Nomenclature for cluster members adopted by Lang et al. (2005).

b. Spectral classification by Clark et al. (2018b).

c. Wind parameters for qG3 and Pistol stars from Table 1 by Najarro et al. (2009); values for qG8, qG9, qG11, qG15, qG16, qG21, qG25, and qG27 based on measurements for GSC4 star by Najarro et al. (2017); parameters for qG2, qG4, qG6, qG10, and qG22 by Liermann et al. (2010), except μ for qG2 and qG4 estimated by Najarro (private communication); for sources of spectral types WN6, B supergiants and O/a we adopted values of stars of similar type.

d. Derived from the 22.5 GHz flux density for qG1 (QR6), qG2 (QR5), qG6 (QR8) sources and Pistol Star, and from the 8.5 GHz flux density for qG13 (QR4), qG11 (QR7) and qG3 (QR9), as described in Table 4 by Lang et al. (2005). Values have been re-scaled (see above).

Table 4.4: – continued from previous page

Source	Spectral type [b]	v_∞ [c] (Km/s)	μ [c] (#)	$\dot{M}_{2018}$ 6.0 GHz	$\dot{M}_{2016}$ 10.0 GHz	$\dot{M}_{2018}$ 10.0 GHz	$\dot{M}_{Lang2005}$ 22.5 GHz [d]
qG16	WC8(d? +OB?)	1250	4.7	$(5.4 \pm 1.0) \times 10^{-5}$	$(4.9 \pm 1.0) \times 10^{-5}$	$(5.8 \pm 1.0) \times 10^{-5}$	
qG17	B0-1 Ia$^+$/WNLh	500	1.3	$(3.2 \pm 0.8) \times 10^{-6}$	$(5.1 \pm 1.0) \times 10^{-6}$	$(4.8 \pm 2.0) \times 10^{-6}$	
qG18	WN6	1600	4.1	$(2.6 \pm 0.7) \times 10^{-5}$	$(5.1 \pm 1.0) \times 10^{-5}$	$(4.8 \pm 2.0) \times 10^{-5}$	
qG19							
qG20	B2-3Ia$^+$	500	1.3	$(3.2 \pm 0.9) \times 10^{-6}$	$(4.4 \pm 1.0) \times 10^{-6}$	$(2.1 \pm 0.6) \times 10^{-6}$	
qG21	WC8-9(d? +OB?)	1250	4.7	$(2.9 \pm 0.8) \times 10^{-5}$	$(3.5 \pm 0.8) \times 10^{-5}$	$(3.5 \pm 0.8) \times 10^{-5}$	
qG22	WN8-9ha	900	2.0	$(9.0 \pm 2.0) \times 10^{-6}$	$(1.1 \pm 0.2) \times 10^{-5}$	$(1.1 \pm 0.3) \times 10^{-5}$	
qG23	O7-8 Ia	1500	1.3	$(9.7 \pm 3.0) \times 10^{-6}$	$(1.2 \pm 0.3) \times 10^{-5}$	$(1.3 \pm 0.3) \times 10^{-5}$	
qG24	B0-1 Ia$^+$	500	1.3	$(2.6 \pm 0.8) \times 10^{-6}$	$(3.8 \pm 0.9) \times 10^{-6}$	$(4.4 \pm 1.0) \times 10^{-6}$	
qG25	WC9d(+OB)	1250	4.7	$(2.4 \pm 0.7) \times 10^{-5}$	$(3.2 \pm 0.7) \times 10^{-5}$	$(2.8 \pm 0.7) \times 10^{-5}$	
qG26							
qG27	WC9d(+OB)	1250	4.7	$(1.7 \pm 0.6) \times 10^{-5}$	$(2.5 \pm 0.6) \times 10^{-5}$	$(2.4 \pm 0.6) \times 10^{-5}$	
qG28							
qG29							

Notes. It is shown a comparison to estimations done by (Lang et al., 2005) from their 22.5 GHz when possible, and otherwise from their 8.5 GHz observations, re-scaled for taking into account their assumed $v_\infty = 1000 \, Km \, s^{-1}$ and $\mu = 2$. All mass-loss rates, $\dot{M}$, are in units of $M_\odot \, yr^{-1}$.

[a] Nomenclature for cluster members adopted by Lang et al. (2005).

[b] Spectral classification by Clark et al. (2018b).

[c] Wind parameters for qG3 and Pistol stars from Table 1 by Najarro et al. (2009); values for qG8, qG9, qG11, qG15, qG16, qG21, qG25, and qG27 based on measurements for GSC4 star by Najarro et al. (2017); parameters for qG2, qG4, qG6, qG10, and qG22 by Liermann et al. (2010), except μ for qG2 and qG4 estimated by Najarro (private communication); for sources of spectral types WN6, B supergiants and OIa we adopted values of stars of similar type.

[d] Derived from the 22.5 GHz flux density for qG1 (QR6), qG2 (QR5), qG6 (QR8) sources and Pistol Star, and from the 8.5 GHz flux density for qG13 (QR4), qG11 (QR7) and qG3 (QR9), as described in Table 4 by Lang et al. (2005). Values have been re-scaled (see above).

4

stars, with an averaged value of $\sim 4 \times 10^{-5}\, M_\odot\, yr^{-1}$. The WR stars from our data set have $\dot{M}$ values ranging from 1.3×10^{-5} to $7.9 \times 10^{-5}\, M_\odot\, yr^{-1}$, which agrees well with the results of Leitherer et al. (1997), as well as for other young, massive stellar types. This conclusion lead us to choose B1−2 Ia$^+$ and B0−1 Ia$^+$ as the most probable spectral types for qG13 and qG17, respectively, as their mass-loss rates are not in that range.

On the other hand, qG5, qG7, qG11, qG19, and qG20 have flat or inverted spectral indices, which indicates the presence of non-thermal emission that may be attributed to colliding winds in binaries.

qG8, and qG16 are ambiguous cases. No measurement of α is available for the star qG28 because it is only detected in a single band.

We can probe variability because we have two epochs with X-band measurements. We contemplate the existence of flux density variability when the differences in the flux densities between the two epochs are higher than $5\,\sigma$. With this criterion we consider as variable the two LBVs, qG3 and the Pistol star, as well as the sources qG1, qG8, qG12, qG20, and qG29. For qG10, and qG11, the variability is rather small, but taking into account the possible binary nature of qG11, we speculate that the contribution from non-thermal emission may be modulated by the orbital motion of the system. Further investigation would be necessary to find a correlation between the periodicity and the orbital period. In conclusion, we find that 9 out of the 29 radio sources, approximately a 30%, display significant variability. This is a remarkably higher fraction than in the Arches cluster, where we find that $\lesssim 15\%$ of the radio stars display variability. We speculate that this may be related to the advanced evolutionary state of the older Quintuplet stars.

4.5. Analysis of the radio luminosity function

Basic assumptions

With assumptions about the age and mass of a young cluster, a comparison between the number and the observed flux of detected radio stars with predictions from theoretical stellar evolutionary models (isochrones) can help to assess the quality of those models, on the one hand, and − if the theoretical isochrones are considered sufficiently reliable − to infer basic properties of the cluster, on the other hand. In subsection 3.4.2 of previous chapter (peer-reviewed publication by Gallego-Calvente et al. (2021)), we have shown that the observed number of radio stars in the Arches cluster appears to require a top-heavy initial mass function with a power-law exponent $\alpha_{IMF} = -1.8$ (contrary to the Solar environment "Salpeter" exponent $\alpha_{IMF} = -2.35$).

In this chapter, we tentatively go a step further and use the radio luminosity function (RLF) of the stars, i.e. we use both the number of sources as well as their flux density for comparison with the models. We do this first for the Arches cluster

and then for the Quintuplet cluster. We emphasize that we cannot undertake an exhaustive study here, which would require taking into account a large number of potentially important parameters, such as, for example, the role of metallicity or the wind volume filling factor, which we neglect here. Nevertheless, we show that our simple toy modelling indicates that current theoretical models of the evolution of massive stars appear to be fairly realistic, and that we can infer constraints on the properties of the clusters by comparing radio observations with predictions from isochrones.

We use PARSEC (release v1.2S + COLIBRI S_37, http://stev.oapd.inaf.it/cmd, Bressan et al., 2012b; Chen et al., 2014b, 2015a; Tang et al., 2014b; Marigo et al., 2017b; Pastorelli et al., 2019b, 2020) and MIST (https://waps.cfa.harvard.edu/MIST/, Dotter, 2016; Choi et al., 2016; Paxton et al., 2011b, 2013, 2015) theoretical isochrones for solar metallicity. To convert the mass-loss rates from the theoretical isochrones to observable radio flux, we use the relation

$$
\left[\frac{S_v}{mJy}\right] = (5.34\times10^{-4})^{-4/3} f_{clump}^{1/2} \left[\frac{\dot{M}}{M_\odot\, yr^{-1}}\right]\left[\frac{v_\infty}{km\, s^{-1}}\right]^{-4/3}\left[\frac{d}{kpc}\right]^{-2}\left[\frac{v}{Hz}\right]^{2/3}\left[\frac{\mu^2}{Z^2\gamma g_v}\right]^{-2/3},
$$
(4.1)

which is just the inversion of equation 3.5 of previous chapter and has been reported before in similar versions (e.g. Gallego-Calvente et al., 2021; Montes et al., 2009; Leitherer et al., 1997). The observing frequency is $v = 10\,GHz$. We assume a mean molecular weight $\mu = 1.3$, a mean ion charge $Z = 1$, and a mean number of electrons per ion $\gamma = 1$. As concerns the Gaunt factor

$$
g_v = 9.77 \cdot \left(1 + 0.13 \cdot log\, \frac{T_e^{3/2}}{Zv}\right),
$$
(4.2)

we use $T_e = 10^4$ K. Any changes to these assumed values of the parameters by factors of two to a few do not significantly change the resulting radio flux. A potentially important factor, that we have not yet mentioned, is wind clumping. The volume filling factor, f_{clump}, is one for a homogeneous stellar wind and smaller than one for a clumpy wind. For simplicity, we here assume $f_{clump} = 1$.

The validity of such a rule-of-thumb approach is demonstrated in Fig. 4.5, where we compare the observed flux densities of radio stars in the Arches cluster with the ones computed from their individually determined mass-loss rates (Gallego-Calvente et al., 2021) and using the simplified assumptions. The differences appear to be small enough to justify an efficient, simplified computation of the radio flux densities. From here on we will use these simplified assumptions on the parameters that enter Equation 4.1 and only consider the observed radio flux densities, not the mass-loss rates.
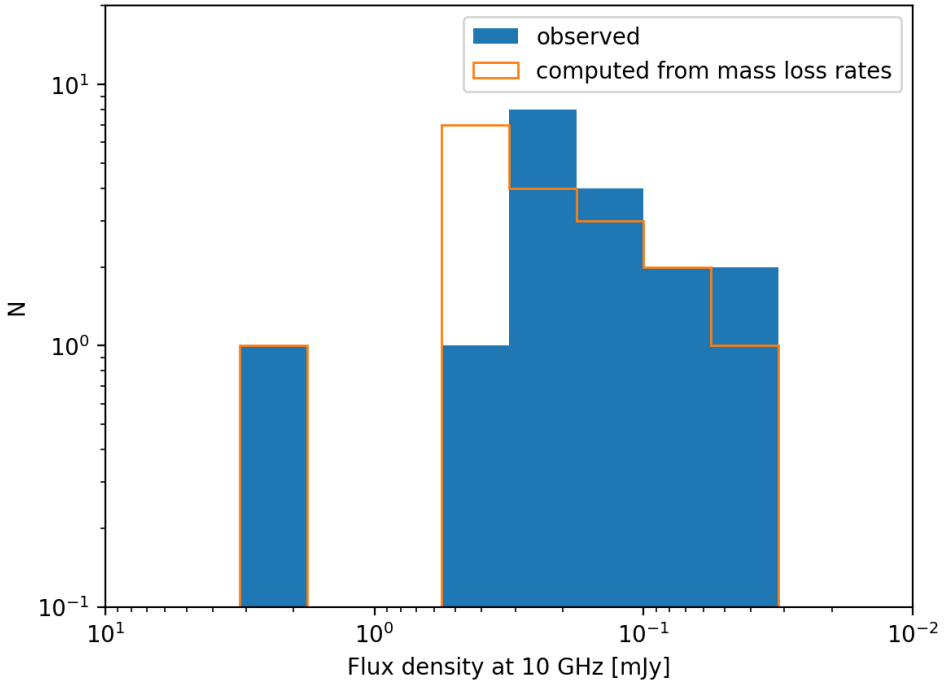
Figure 4.5: Blue, solid: Histogram of observed flux densities of radio stars in the Arches cluster (Gallego-Calvente et al., 2021). Orange, outline: Histogram of radio fluxes of the same stars, using the mass-loss rates reported by Gallego-Calvente et al. (2021) and converting to radio flux density with Equation 4.1 assuming the same parameters for all stars.

For our cluster models we always use a one-segment power-law initial mass function (IMF) with an upper mass of $150\,M_\odot$ and a lower mass of $0.8\,M_\odot$. Our results are not sensitive to reasonable changes of these parameters. Also, since our sources of interest represent only the very tip of the mass distribution, assuming a two-segment IMF does not introduce any significant changes.

We tested whether the random sampling of the high mass end of the IMF posed any serious problems by random realisations of clusters of given age, mass, and IMF. We only used MIST models for this test and assumed that we could only detect stars with a radio flux density $\gtrsim 0.04\,$mJy, the approximate detection limit here and in Gallego-Calvente et al. (2021). We found that the age of the clusters can typically be recovered well ($\pm 1\,$Myr) and that the cluster parameters could best be recovered for an age of $\sim 3\,$Myr, where the number of bright radio stars peaks. Whether the IMF was top-heavy or not could also be recovered with great reliability. However, we found a degeneracy between the RLFs for the ages of 2 and 6 Myrs. Since these values lie safely outside (or at the very extreme) of the ages reported for the Arches and Quintuplet clusters, we do not use them in our subsequent analyses.

Models

Figure 4.6 shows predictions at two different ages for a model cluster with a total initial stellar mass of $10^4\,M_\odot$ and a power-law IMF with an exponent $\alpha_{IMF} = -1.8$ (Hosek et al., 2019), using MIST isochrones. We averaged and used the $1\,\sigma$ confidence intervals of the result of 10 simulations of the cluster. The upper panel shows the present-day mass function, the middle one histograms of the predicted radio flux density, and the lower one cumulative histograms of the predicted radio flux density. Observed values in Arches and Quintuplet are overplotted in black. Finally, we show the same models, created with PARSEC isochrones, in Figure 4.7. We can see differences due to the use of different theoretical isochrones, but we can also see the overall similarity of the predictions.

Given the weak flux density of radio stars we can only observe the bright tail of the distribution. We can see that the RLF can change drastically as a function of age. This is due to the rapid development of the extremely massive stars at such young ages. The latter also means that single stellar evolution models are expected to work well because we do not expect any significant effects such as mass-transfer to occur in binaries at these time scales. Also, stellar evolution happens so fast at these young ages that the radio flux of a binary will typically be dominated by one of the two sources, except in the unlikely case that the two stellar masses are exactly equal. Of course, colliding wind binaries will be a source of uncertainty, but their numbers are small and we do not think that they will affect the observed population statistics significantly. We do not test this assumption here, however, given that this would go beyond the simple model presented here. To avoid having to deal with complex binning issues we will use cumulative luminosity functions from this point on.

A parameter of significant interest is the exponent of the power-law of the IMF, α_{IMF}, because is has a strong influence on the number of massive stars that initially form in a cluster. In previous chapter (peer-reviewed publication Gallego-Calvente et al., 2021) we showed that the observed number of radio stars in the Arches cluster favoured a top-heavy IMF, that had been found by other work on this cluster. In Fig. 4.8 we illustrate how the bright end of the RLF changes as a function of α_{IMF}. The RLF of the model cluster with a Salpeter IMF will only be similar to the one of a cluster with a top-heavy IMF ($\alpha_{IMF} = -1.8$) for an initial mass that is four to five times higher. While uncertainties up to a factor two are possible in the observational determination of a young, massive cluster's mass (for example from optical or infrared observations), higher factors can generally be ruled out safely. Therefore, the observed RLF can be help to constrain the exponent of the power-law IMF of a young massive cluster. The most important degeneracy to keep in mind is the one between cluster mass and IMF exponent. There is also some degeneracy with age, but less so, because the shape of the bright end of the RLF changes sensitively as a function of age. With reasonable constraints on the age

and mass of a cluster, one may therefore constrain its properties via the RLF.

Following the previous deliberations, we proceed to fit cluster models to the observed radio luminosity functions of the Arches and Quintuplet clusters. This is a demonstration of the principle, so we limit ourselves to a crude exploration of parameter space with simple, brute-force Monte Carlo simulations. To create the MC samples, the observed radio flux densities were varied randomly assuming for each source a Gaussian normal distribution centred on the observed radio flux density and a conservative standard deviation of 30% from the mean value (assuming the same uncertainty for all sources). The parameter space was spanned by two values of $\alpha_{IMF} = -1.8, -2.35$, ages of 2.5, 3, 3.5, 4, 4.5, 5 Myr and cluster masses of 1.0 and $1.5 \times 10^4\,M_\odot$.

Arches cluster

We determined the best fit parameters for each of the 100 MC realisations of the RLF observed by Gallego-Calvente et al. (2021). Figure 4.9 shows the resulting distribution of the parameters of the best fit models with MIST isochrones and Fig. 4.10 for Parsec isochrones. There is no clear preference for the total cluster mass, but the top-heavy IMF provides the best solution in the vast majority of cases. The cluster age is broadly distributed, but peaks at 3 to 3.5 Myr, in agreement with literature.

Quintuplet cluster

We determined the best fit parameters for each of the 100 MC realisations of the RLF observed by here. Figure 4.11 shows the resulting distribution of the parameters of the best fit models with MIST isochrones and Fig. 4.12 for Parsec isochrones. As in the case of the Arches cluster, the cluster mass does not appear to be well constrained, but again the top-heavy IMF provides the best solution in the vast majority of cases. The cluster age is broadly distributed and peaks at 3.5 to 4 Myr, in agreement with literature that assigns an older age to the Quintuplet than to the Arches.
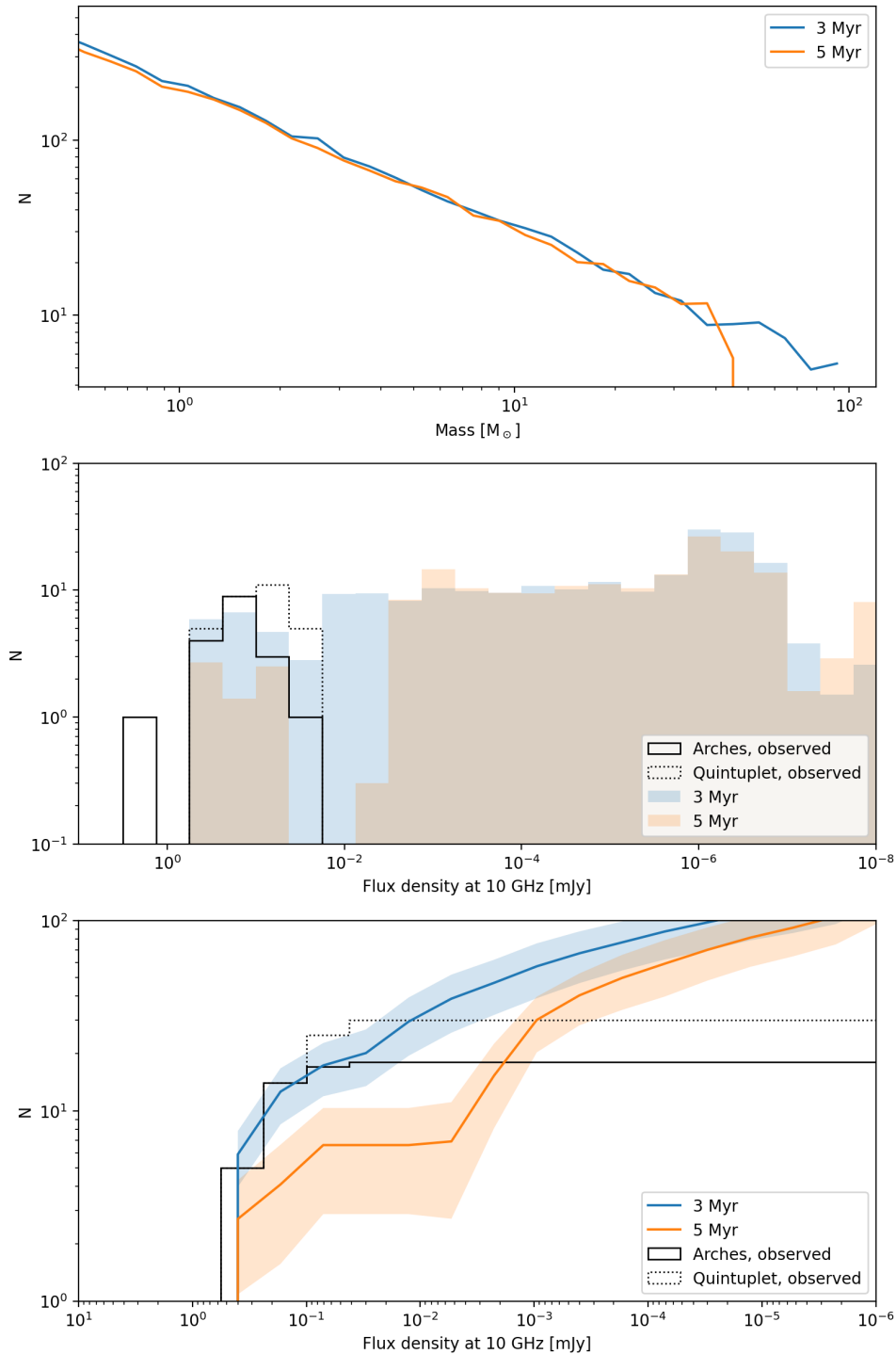
Figure 4.6: Radio flux densities of massive stars in a model cluster, using MIST isochrones. Top: Present-day mas function. Middle: Histograms of predicted radio flux densities. Bottom: Cumulative histograms of predicted radio flux densities. The black histogram are observed values for the Arches cluster (Gallego-Calvente et al., 2021, dotted) and for the Quintuplet cluster (this chapter, solid).
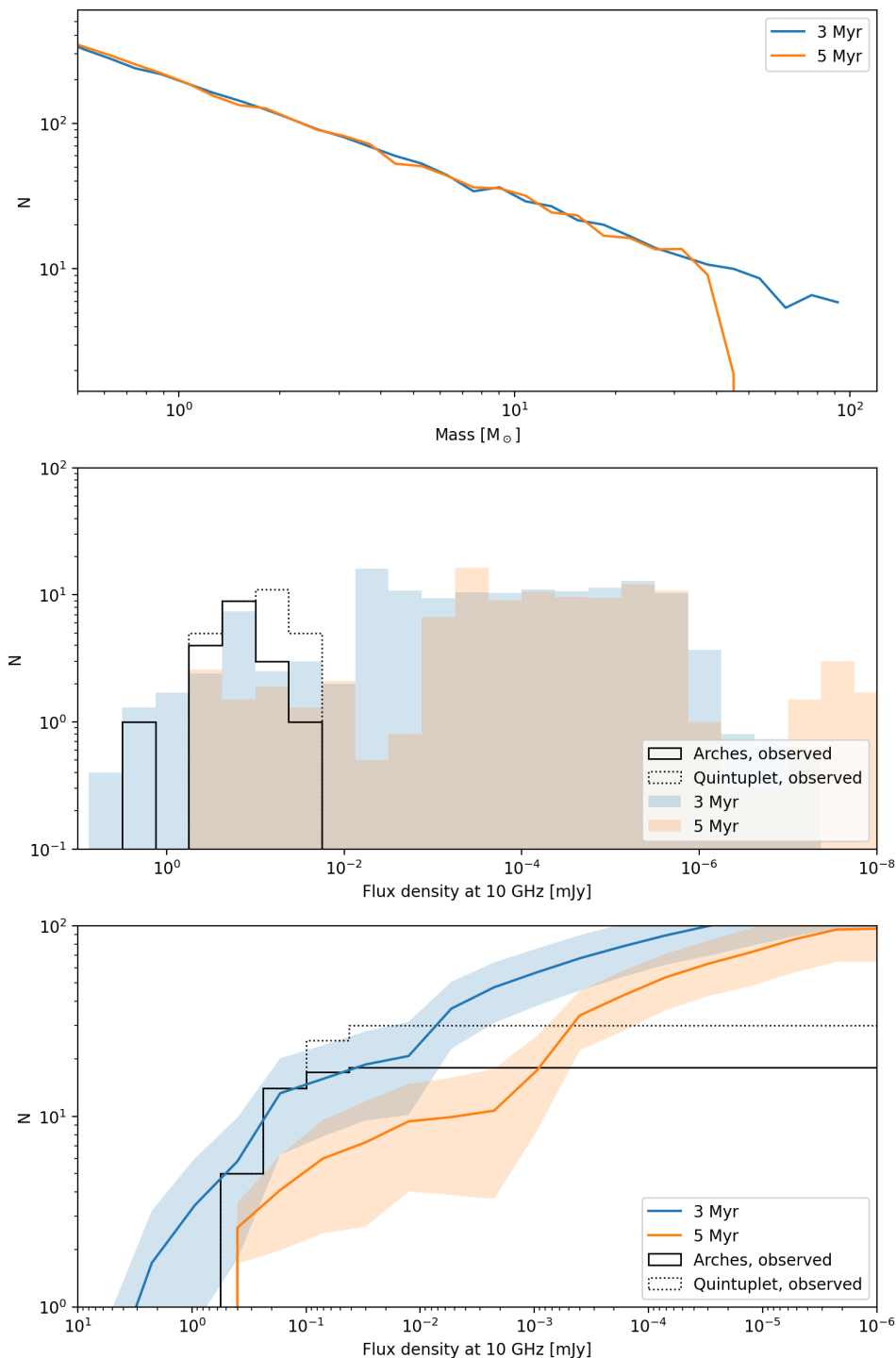
Figure 4.7: Radio flux densities of massive stars in a model cluster, using PARSEC isochrones. Top: Present-day mas function. Middle: Histograms of predicted radio flux densities. Bottom: Cumulative histograms of predicted radio flux densities. The black histogram are observed values for the Arches cluster (Gallego-Calvente et al., 2021, dotted) and for the Quintuplet cluster (this chapter, solid).
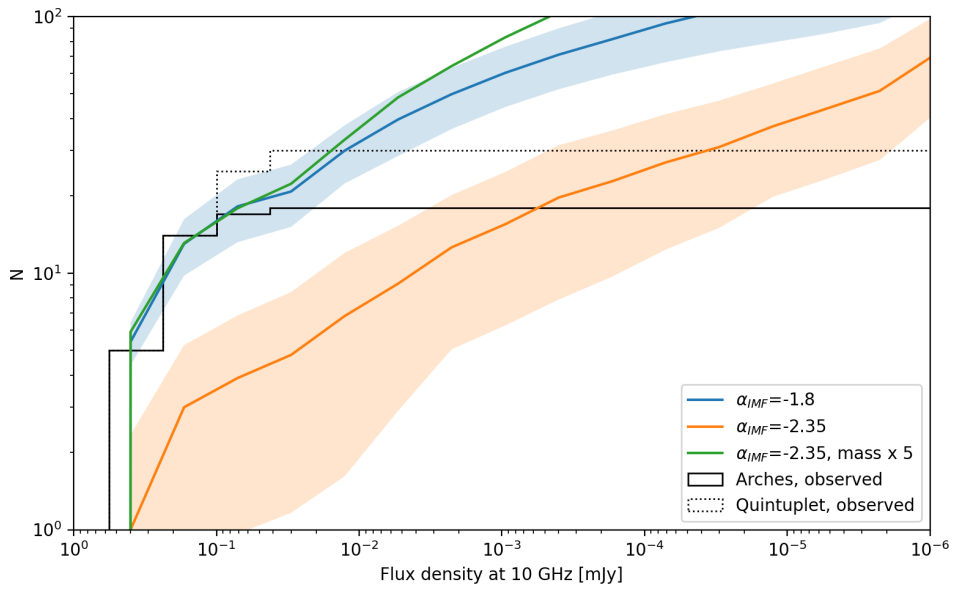
Figure 4.8: Simulated radio luminosity functions for a 3 Myr old cluster with an initial stellar mass of 10^4 M$_\odot$, using $\alpha_{IMF} = -1.8$ and the standard Salpeter value of $\alpha_{IMF} = -2.35$.
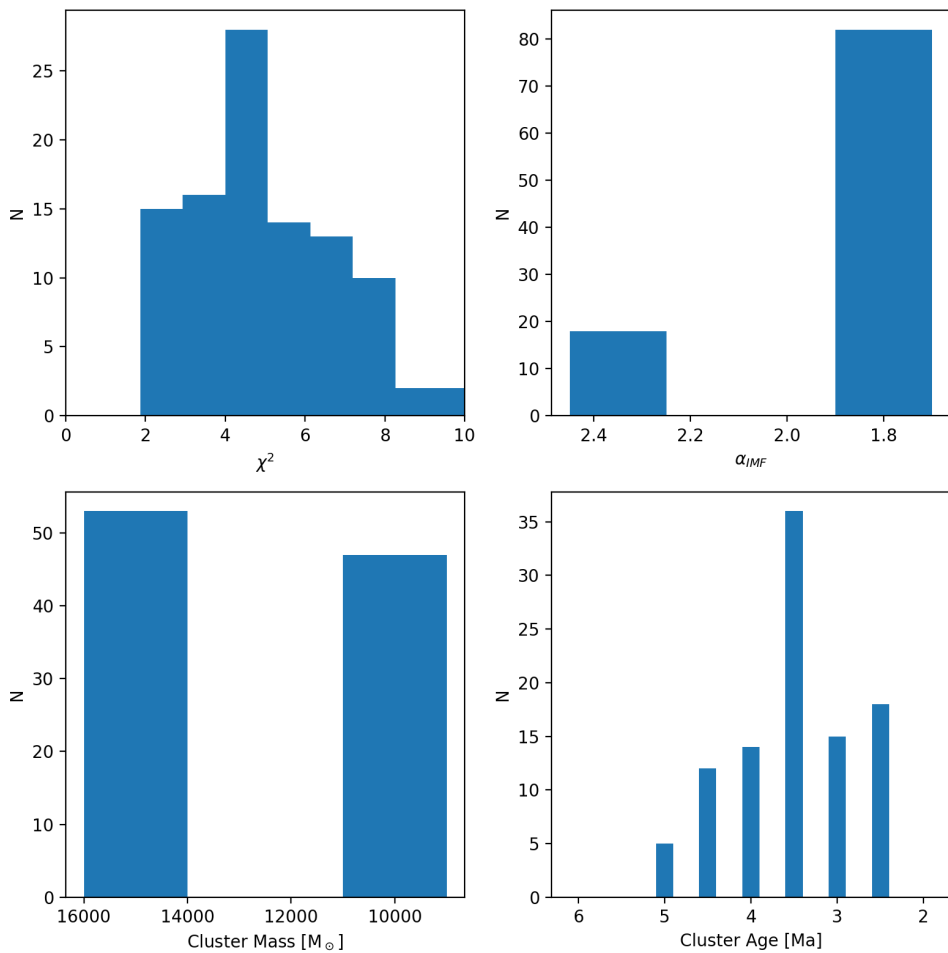
Figure 4.9: Results of MC simulations of the Arches RLF, using MIST isochrones.
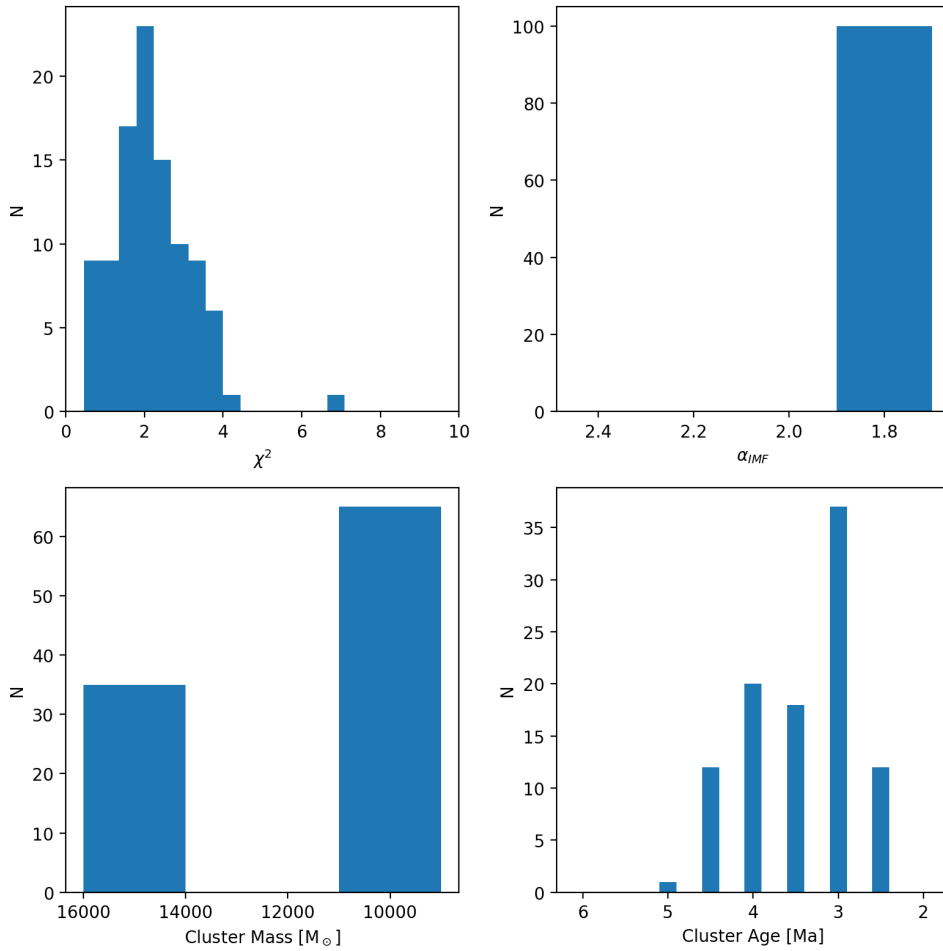
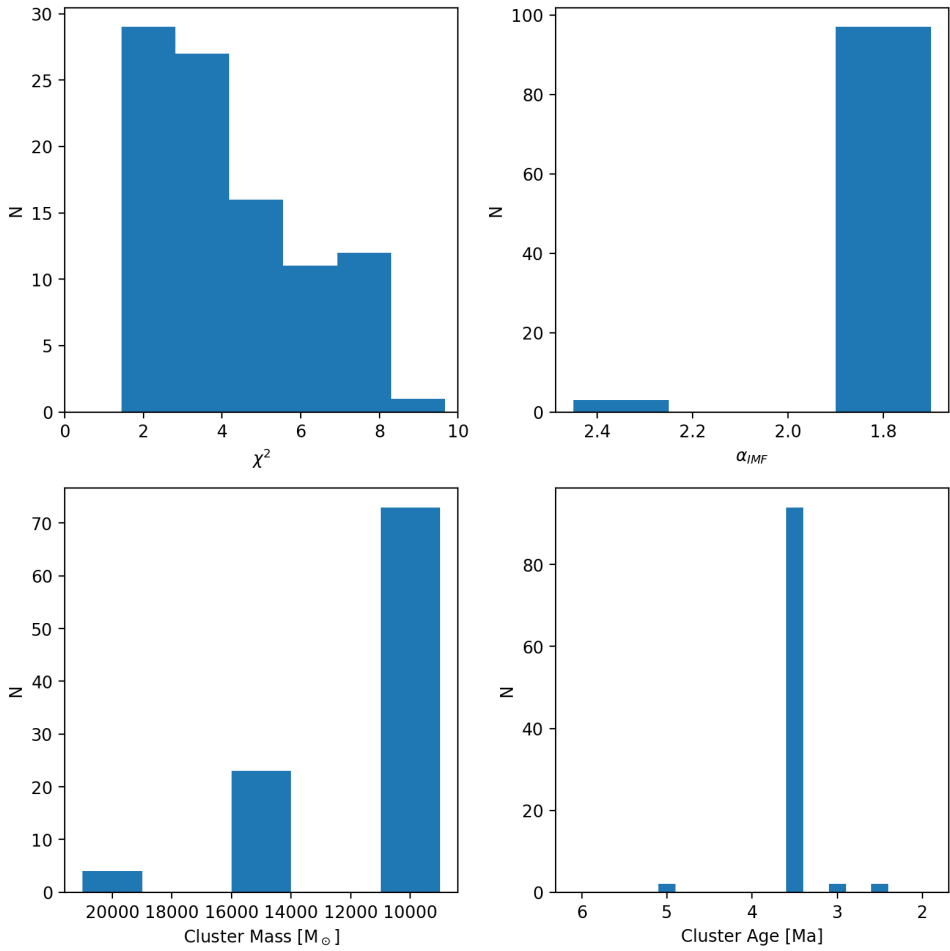Figure 4.10: Results of MC simulations of the Arches RLF, using PARSEC isochrones.

Figure 4.11: Results of MC simulations of the Quintuplet RLF, using MIST isochrones.
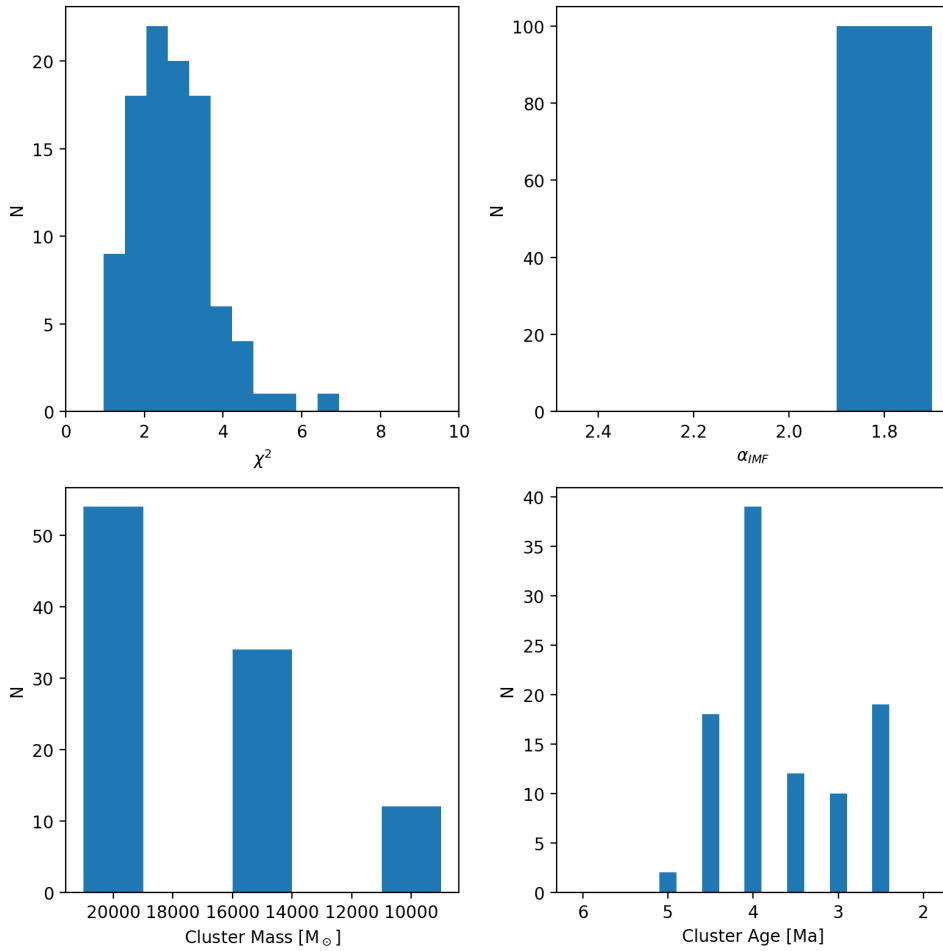
Figure 4.12: Results of MC simulations of the Quintuplet RLF, using PARSEC isochrones.

5

Conclusions

It is attempting the impossible as possible is done.

— Henri Barbusse

In this thesis, I have presented the results of my research on a joint near-infrared and sensitive radio study of massive stars of two of the most emblematic young, massive, starburst-like clusters at the Galactic centre, Arches and Quintuplet, using high-angular-resolution techniques, in particular radio interferometry. All radio interferometric data were processed and analysed interactively. As usually in science, some of the code used in the analysis was developed by myself.

In the following lines, I present the main conclusions obtained in this dissertation:

- Sensitive radio interferometric observations are a new window to study the properties of massive stars in the targeted clusters as well as to obtain constraints on the overall properties of the clusters, such as their initial mass function.

- I have presented new radio continuum data ten times more sensitive than any prior equivalent observations at 10 and 6 GHz and have been able to detect two (Arches) to four (Quintuplet) times as many radio stars as previous work.

- The comparison between theoretical isochrones and our observations shows that the mass-loss rates in the theoretical models appear to be realistic.

- The radio luminosity functions of the Arches and Quintuplet clusters that I have measured confirm that the Quintuplet cluster is older than the Arches

cluster and that both clusters can be characterised by an initial mass function that is considerably steeper than the standard Salpeter value, independent from but in agreement with the work of Hosek et al. (2019) on the Arches cluster.

- I find that most sources can be described by thermal emission in winds around single stars, but I also detect a significant number of potential binaries, some of them confirmed by independent observations, in agreement with the expectation that many massive stars reside in multiple systems.

- Some sources are identified as variable. Remarkably I find a singificantly higher fraction of variable stars in the Quintuplet cluster ($\sim 30\%$) than in the Arches cluster ($< 15\%$). I speculate that this may be due to the more instable nature of the more evolved stars in the older Quintuplet cluster.

- Finally, I have demonstrated that the radio luminosity function can be used as a tool to constrain the age and/or mass of a cluster and also its mass function.

5

I show that with the extraordinary sensitivity of the JVLA we can detect massive stars with mass-loss rates up to $1.3 \times 10^{-5} \, M_\odot \, yr^{-1}$ in Arches. With the advent of the Square Kilometre Array at mid-frequency (SKA-MID), which will cover the frequency range 350 MHz to 14 GHz, especially at the highest frequencies (Band 5) where the highest contribution from the optically thick stellar wind is expected, it will be possible to measure mass-loss rates of $\sim 10^{-7} \, M_\odot \, yr^{-1}$ at the distance of the GC in tens of minutes integration time. This would favour studies of massive stars and their associated winds at all stages of evolution, including pre-main sequence stars, luminous blue variables, and Wolf-Rayet stars, and at the same age inside the three main massive stellar clusters at the GC (the Central Cluster, Arches, and Quintuplet).

6

Future work

*One, remember to look up at the stars and not down at your feet.
Two, never give up work. Work gives you meaning and purpose
and life is empty without it.
Three, if you are lucky enough to find love,
remember it is there and do not throw it away.*

Stephen Hawking

Follow-up work on the study of massive stars presented in this thesis includes the following projects:

- **Improvement of results:** Current observations need to be improved because we are dominated by systematics. For this reason we need observations with the JVLA in multiple configurations and with longer tracks in order to fill-in UV space far more completely. In addition, I will work far more closely with the NIR data. In the present study I have been very conservative selecting the detected sources, but after considering our results, I can go more in depth even in the "old" data because a comparison with infrared images is extremely effective in eliminating spurious sources.

- **Programming CASA software add-on:** From my experience acquired with the current primary data processing software for the VLA, CASA, I found that there is a significant improvement that should be implemented to obtain all the information that CASA displays from its viewer task. This extension will radically reduce the spent time obtaining fluxes, positions, etcetera, from the final images. The selected information will be downloaded directly to a text

file in an appropriate format. The add-on is planned to be written in an open source language, like Python, to be easily integrated in CASA and make it available to the community.

- **Extending this work to other young massive clusters and to more sensitive telescopes:** The research described here can be easily extended to other massive clusters in the Milky Way such as Westerlund 1 and 2 or NGC 3603. With its extreme sensitivity the future SKA will allow us to measure the radio luminosity function in massive cluster down to significantly fainter flux densities, which will provide stringent constraints on cluster properties and excellent calibration data for mass loss rates in theoretical models.

- **From continuum to spectral lines:** Fortunately and thanks to a close collaboration with another research group, I have had the chance of having the first contact with observations and data reduction of spectral lines. This new horizon opens another possibility to study star-forming regions based on molecular line observations. I plan to continue this cooperation that will lead as immediate result to a refereed paper with me as a co-author.

6

A

Appendix

The Galactic O-Star Catalog (GOSC) is the third version of an ambitious project to include as much accurate information related to this type of objects as possible. This version includes cross-references to other catalogs, spectral classifications, astrometric information, basic photometry, and cluster/association membership.

GOSC places a special emphasis on the uniformity of the spectral classification used. In order to satisfy that requirement, the first version of the catalog was built in 2002 starting with the 350 Galactic O stars catalogued by Nolan R. Walborn over the years and adding a few stars with reliable spectral classifications. With the second version of the catalog we added 800 stars from the literature in 2006 but we soon discovered that many of those spectral types were unreliable. As a consequence, we started the Galactic O-Star Spectroscopic Survey (GOSSS) with the intention of obtaining modern blue-violet spectra with R = 2500 of all Galactic stars that had at least one previous classification as O or B0. In June 2013 GOSSS became the basis for the spectral types in the third version of GOSC. The current version lists the 611 O stars, 32 BA stars, and 12 late-type stars in GOSSS-DR2.2. Future versions will include additional Galactic O stars as well as other stars in supplements.

Jesús Maíz Apellániz

(From https://gosc.cab.inta-csic.es/)

Table A.1: Qualifiers for O stars.

((f))	Weak N III 4634−40−42 emission, strong He II 4686 absorption
(f)	Medium N III 4634−40−42 emission, neutral or weak He II 4686 absorption
f	Strong N III 4634−40−42 emission, He II 4686 emission above continuum
((f*))	N IV 4058 emission >= N III 4640 emission, strong He II 4686 absorption (O2−3)
(f*)	N IV 4058 emission >= N III 4640 emission, weaker He II 4686 absorption (O2−3.5)
f*	N IV 4058 emission >= N III 4640 emission, He II 4686 emission (O2−3.5)
((fc))	As ((f)) plus C III 4647−50−51 emission equal to N III 4634
(fc)	As (f) plus C III 4647−50−51 emission equal to N III 4634
fc	As f plus C III 4647−50−51 emission equal to N III 4634
f?p	Variable C III 4647−50−51 emission >= N III 4634−40−42 at maximum; variable sharp absorption, emission, and/or P Cygni features at H and He I lines
((f+))	As ((f)) plus Si IV 4089−4116 emission (O4−8, obsolete)
(f+)	As (f) plus Si IV 4089−4116 emission (O4−8, obsolete)
f+	As f plus Si IV 4089−4116 emission (O4−8, obsolete)
(e)	Probable H alpha emission but no red spectrogram available
e	Emission components in H lines
pe	As e with emission components in He I and/or continuum veiling
[e]	Emission spectrum including Fe forbidden lines
e+	Fe II and H emission lines (subcategories in Lesh 1968)
((n))	Broadened lines (not applied in GOSSS, marginal)
(n)	More broadened lines (v sini ∼ 200 km/s)
n	Even more broadened lines (v sin i ∼ 300 km/s)
nn	Yet even more broadened lines (v sin i ∼ 400 km/s)
[n]	H lines more broadened than He lines
nfp	He II centrally reversed emission, broadened absorption lines (Conti Oef)
N	N absorption enhanced, C and O deficient
Nstr	Moderate case of above (e.g. N III 4640 enhanced but not > C III 4650)
C	C absorption enhanced, N deficient
Nwk	Moderate case of above
var	Variation in line spectrum intensities or content
p	Peculiar spectrum
z	He II 4686 in absorption and > than both He I 4471 and He II 4542

Credits: Maíz Apellániz et al. (2013), in Massive Stars from α to Ω, publication in which the author of this thesis, Aurelia Teresa Gallego Calvente, is co-author.
Table extracted from https://gosc.cab.inta-csic.es/qualifiers-o-stars.

The Galactic O-star spectroscopic survey (GOSSS) is fully described in Maíz Apellániz et al. (2011).

References

Abbott, D. C., Bieging, J. H., and Churchwell, E. (1981). Mass loss from very luminous OB stars and the CYG superbubble. *ApJ*, 250:645–659.

Abuter, R., Amorim, A., Bauboeck, M., Berger, J. P., Bonnet, H., Brandner, W., Clenet, Y., Coude du Foresto, V., de Zeeuw, P. T., Dexter, J., Duvert, G., Eckart, A., Eisenhauer, F., Foerster Schreiber, N. M., Garcia, P., Gao, F., Gendron, E., Genzel, R., Gerhard, O., Gillessen, S., Habibi, M., Haubois, X., Henning, T., Hippler, S., Horrobin, M., Jimenez-Rosales, A., Jocou, L., Kervella, P., Lacour, S., Lapeyrere, V., Le Bouquin, J. B., Lena, P., Ott, T., Paumard, T., Perraut, K., Perrin, G., Pfuhl, O., Rabien, S., Rodriguez Coira, G., Rousset, G., Scheithauer, S., Sternberg, A., Straub, O., Straubmeier, C., Sturm, E., Tacconi, L. J., Vincent, F., von Fellenberg, S., Waisberg, I., Widmann, F., Wieprecht, E., Wiezorrek, E., Woillez, J., and Yazici, S. (2019). A geometric distance measurement to the Galactic Center black hole with 0.3% uncertainty. *arXiv e-prints*, page arXiv:1904.05721.

Agliozzo, C., Mehner, A., Phillips, N. M., Leto, P., Groh, J. H., Noriega-Crespo, A., Buemi, C., Cavallaro, F., Cerrigone, L., Ingallinera, A., Paladini, R., Pignata, G., Trigilio, C., and Umana, G. (2019). A massive nebula around the luminous blue variable star RMC 143 revealed by ALMA. *A&A*, 626:A126.

Bartko, H., Martins, F., Trippe, S., Fritz, T. K., Genzel, R., Ott, T., Eisenhauer, F., Gillessen, S., Paumard, T., Alexander, T., Dodds-Eden, K., Gerhard, O., Levin, Y., Mascetti, L., Nayakshin, S., Perets, H. B., Perrin, G., Pfuhl, O., Reid, M. J., Rouan, D., Zilka, M., and Sternberg, A. (2010). An Extremely Top-Heavy Initial Mass Function in the Galactic Center Stellar Disks. *ApJ*, 708(1):834–840.

Benaglia, P. (2010). Non-Thermal Radio Emission from OB Stars: An Observer's View. In Martí, J., Luque-Escamilla, P. L., and Combi, J. A., editors, *High Energy Phenomena in Massive Stars*, volume 422 of *Astronomical Society of the Pacific Conference Series*, page 111.

Bressan, A., Marigo, P., Girardi, L., Salasnich, B., Dal Cero, C., Rubele, S., and Nanni, A. (2012a). PARSEC: stellar tracks and isochrones with the PAdova and TRieste Stellar Evolution Code. *MNRAS*, 427(1):127–145.

Bressan, A., Marigo, P., Girardi, L., Salasnich, B., Dal Cero, C., Rubele, S., and Nanni, A. (2012b). PARSEC: stellar tracks and isochrones with the PAdova and TRieste Stellar Evolution Code. *MNRAS*, 427:127–145.

Carroll, B. W. and Ostlie, D. A. (2014). *An Introduction to Modern Astrophysics*. Pearson, Edinburgh Gate. Harlow. Essex CM20 2JE, 2nd edition.

Chen, Y., Bressan, A., Girardi, L., Marigo, P., Kong, X., and Lanza, A. (2015a). PAR-SEC evolutionary tracks of massive stars up to 350 $M_\odot$ at metallicities 0.0001 ≤ Z ≤ 0.04. *MNRAS*, 452:1068–1080.

Chen, Y., Bressan, A., Girardi, L., Marigo, P., Kong, X., and Lanza, A. (2015b). PAR-SEC evolutionary tracks of massive stars up to 350 $M_\odot$ at metallicities 0.0001 ≤ Z ≤ 0.04. *MNRAS*, 452(1):1068–1080.

Chen, Y., Girardi, L., Bressan, A., Marigo, P., Barbieri, M., and Kong, X. (2014a). Improving PARSEC models for very low mass stars. *MNRAS*, 444(3):2525–2543.

Chen, Y., Girardi, L., Bressan, A., Marigo, P., Barbieri, M., and Kong, X. (2014b). Improving PARSEC models for very low mass stars. *MNRAS*, 444:2525–2543.

Choi, J., Dotter, A., Conroy, C., Cantiello, M., Paxton, B., and Johnson, B. D. (2016). Mesa Isochrones and Stellar Tracks (MIST). I. Solar-scaled Models. *ApJ*, 823(2):102.

Clark, J. S., Lohr, M. E., Najarro, F., Dong, H., and Martins, F. (2018a). The Arches cluster revisited. I. Data presentation and stellar census. *A&A*, 617:A65.

Clark, J. S., Lohr, M. E., Patrick, L. R., and Najarro, F. (2019). The Arches cluster revisited. III. An addendum to the stellar census. *A&A*, 623:A84.

Clark, J. S., Lohr, M. E., Patrick, L. R., Najarro, F., Dong, H., and Figer, D. F. (2018b). An updated stellar census of the Quintuplet cluster. *A&A*, 618:A2.

Clarkson, W. I., Ghez, A. M., Morris, M. R., Lu, J. R., Stolte, A., McCrady, N., Do, T., and Yelda, S. (2012). Proper Motions of the Arches Cluster with Keck Laser Guide Star Adaptive Optics: The First Kinematic Mass Measurement of the Arches. *ApJ*, 751:132.

Contreras, M. E., Rodriguez, L. F., Gomez, Y., and Velazquez, A. (1996). VLA Observations of Massive Stars at 7 Millimeters. *ApJ*, 469:329.

Cotera, A. S., Erickson, E. F., Colgan, S. W. J., Simpson, J. P., Allen, D. A., and Burton, M. G. (1996). The Discovery of Hot Stars near the Galactic Center Thermal Radio Filaments. *ApJ*, 461:750.

Dong, H., Wang, Q. D., Cotera, A., Stolovy, S., Morris, M. R., Mauerhan, J., Mills, E. A., Schneider, G., Calzetti, D., and Lang, C. (2011). Hubble Space Telescope Paschen α survey of the Galactic Centre: data reduction and products. *MNRAS*, 417(1):114–135.

Dotter, A. (2016). MESA Isochrones and Stellar Tracks (MIST) 0: Methods for the Construction of Stellar Isochrones. *ApJS*, 222(1):8.

Dzib, S. A., Loinard, L., Rodríguez, L. F., Gómez, L., Forbrich, J., Menten, K. M., Kounkel, M. A., Mioduszewski, A. J., Hartmann, L., Tobin, J. J., and Rivera, J. L. (2017). Radio Measurements of the Stellar Proper Motions in the Core of the Orion Nebula Cluster. *ApJ*, 834(2):139.

Figer, D. F., Kim, S. S., Morris, M., Serabyn, E., Rich, R. M., and McLean, I. S. (1999a). Hubble Space Telescope/NICMOS Observations of Massive Stellar Clusters near the Galactic Center. *ApJ*, 525:750–758.

Figer, D. F., McLean, I. S., and Morris, M. (1999b). Massive Stars in the Quintuplet Cluster. *ApJ*, 514:202–220.

Figer, D. F., Najarro, F., Gilmore, D., Morris, M., Kim, S. S., Serabyn, E., McLean, I. S., Gilbert, A. M., Graham, J. R., Larkin, J. E., Levenson, N. A., and Teplitz, H. I. (2002). Massive Stars in the Arches Cluster. *ApJ*, 581:258–275.

Figer, D. F., Rich, R. M., Kim, S. S., Morris, M., and Serabyn, E. (2004). An Extended Star Formation History for the Galactic Center from Hubble Space Telescope NICMOS Observations. *ApJ*, 601:319–339.

Fritz, T. K., Gillessen, S., Dodds-Eden, K., Lutz, D., Genzel, R., Raab, W., Ott, T., Pfuhl, O., Eisenhauer, F., and Yusef-Zadeh, F. (2011). Line Derived Infrared Extinction toward the Galactic Center. *ApJ*, 737(2):73.

Gallego-Calvente, A. T., Schödel, R., Alberdi, A., Herrero-Illana, R., Najarro, F., Yusef-Zadeh, F., Dong, H., Sanchez-Bermudez, J., Shahzamanian, B., Nogueras-Lara, F., and Gallego-Cano, E. (2021). Radio observations of massive stars in the Galactic centre: The Arches Cluster. *A&A*, 647:A110.

Genzel, R., Eisenhauer, F., and Gillessen, S. (2010). The Galactic Center massive black hole and nuclear star cluster. *Reviews of Modern Physics*, 82:3121–3195.

Hosek, Jr., M. W., Lu, J. R., Anderson, J., Ghez, A. M., Morris, M. R., and Clarkson, W. I. (2015). The Arches Cluster: Extended Structure and Tidal Radius. *ApJ*, 813:27.

Hosek, Jr., M. W., Lu, J. R., Anderson, J., Najarro, F., Ghez, A. M., Morris, M. R., Clarkson, W. I., and Albers, S. M. (2019). The Unusual Initial Mass Function of the Arches Cluster. *ApJ*, 870:44.

Hußmann, B., Stolte, A., Brandner, W., Gennaro, M., and Liermann, A. (2012). The present-day mass function of the Quintuplet cluster based on proper motion membership. *A&A*, 540:A57.

Lang, C. C., Goss, W. M., and Morris, M. (2001). A VLA H92α Recombination Line Study of the Arched Filament H II Complex Near the Galactic Center. *AJ*, 121:2681–2705.

Lang, C. C., Johnson, K. E., Goss, W. M., and Rodríguez, L. F. (2005). Stellar Winds and Embedded Star Formation in the Galactic Center Quintuplet and Arches Clusters: Multifrequency Radio Observations. *AJ*, 130:2185–2196.

Launhardt, R., Zylka, R., and Mezger, P. G. (2002). The nuclear bulge of the Galaxy. III. Large-scale physical characteristics of stars and interstellar matter. *A&A*, 384:112–139.

Law, C. and Yusef-Zadeh, F. (2004). X-Ray Observations of Stellar Clusters Near the Galactic Center. *ApJ*, 611:858–870.

Leitherer, C., Chapman, J. M., and Koribalski, B. (1995). Radio Continuum Measurements of Southern Early-Type Stars. *ApJ*, 450:289.

Leitherer, C., Chapman, J. M., and Koribalski, B. (1997). Radio Continuum Measurements of Southern Early-Type Stars. II. A Distance-limited Sample of Wolf-Rayet Stars. *ApJ*, 481(2):898–911.

Leitherer, C. and Robert, C. (1991). Observations of Stellar Winds from Hot Stars at 1.3 Millimeters. *ApJ*, 377:629.

Liermann, A., Hamann, W. R., and Oskinova, L. M. (2009). The Quintuplet cluster. I. A K-band spectral catalog of stellar sources. *A&A*, 494(3):1137–1166.

Liermann, A., Hamann, W. R., Oskinova, L. M., Todt, H., and Butler, K. (2010). The Quintuplet cluster. II. Analysis of the WN stars. *A&A*, 524:A82.

Lohr, M. E., Clark, J. S., Najarro, F., Patrick, L. R., Crowther, P. A., and Evans, C. J. (2018). The Arches cluster revisited. II. A massive eclipsing spectroscopic binary in the Arches cluster. *A&A*, 617:A66.

Lu, J. R., Do, T., Ghez, A. M., Morris, M. R., Yelda, S., and Matthews, K. (2013). Stellar Populations in the Central 0.5 pc of the Galaxy. II. The Initial Mass Function. *ApJ*, 764(2):155.

Lucy, L. B. and Solomon, P. M. (1970). Mass Loss by Hot Stars. *ApJ*, 159:879.

Maíz Apellániz, J., Sota, A., Morrell, N. I., Barbá, R. H., Walborn, N. R., Alfaro, E. J., Gamen, R. C., Arias, J. I., and Gallego Calvente, A. T. (2013). First whole-sky results from the Galactic O-Star Spectroscopic Survey. In *Massive Stars: From alpha to Omega*, page 198.

Maíz Apellániz, J., Sota, A., Walborn, N. R., Alfaro, E. J., Barbá, R. H., Morrell, N. I., Gamen, R. C., and Arias, J. I. (2011). The Galactic O-star spectroscopic survey (GOSSS). In Zapatero Osorio, M. R., Gorgas, J., Maíz Apellániz, J., Pardo, J. R., and Gil de Paz, A., editors, *Highlights of Spanish Astrophysics VI*, pages 467–472.

Marigo, P., Girardi, L., Bressan, A., Rosenfield, P., Aringer, B., Chen, Y., Dussin, M., Nanni, A., Pastorelli, G., Rodrigues, T. S., Trabucchi, M., Bladh, S., Dalcanton, J., Groenewegen, M. A. T., Montalbán, J., and Wood, P. R. (2017a). A New Generation of PARSEC-COLIBRI Stellar Isochrones Including the TP-AGB Phase. *ApJ*, 835(1):77.

Marigo, P., Girardi, L., Bressan, A., Rosenfield, P., Aringer, B., Chen, Y., Dussin, M., Nanni, A., Pastorelli, G., Rodrigues, T. S., Trabucchi, M., Bladh, S., Dalcanton, J., Groenewegen, M. A. T., Montalbán, J., and Wood, P. R. (2017b). A New Generation of PARSEC-COLIBRI Stellar Isochrones Including the TP-AGB Phase. *ApJ*, 835(1):77.

Martins, F., Hillier, D. J., Paumard, T., Eisenhauer, F., Ott, T., and Genzel, R. (2008). The most massive stars in the Arches cluster. *A&A*, 478:219–233.

Mauerhan, J. C., Cotera, A., Dong, H., Morris, M. R., Wang, Q. D., Stolovy, S. R., and Lang, C. (2010). Isolated Wolf-Rayet Stars and O Supergiants in the Galactic Center Region Identified Via Paschen-α Excess. *ApJ*, 725:188–199.

Montes, G., Alberdi, A., Pérez-Torres, M. A., and González, R. F. (2015). The Nature of the cm-mm Emission in Close Wolf-Rayet Binaries. *Rev. Mexicana Astron. Astrofis.*, 51:209.

Montes, G., Pérez-Torres, M. A., Alberdi, A., and González, R. F. (2009). Disentangling the Nature of the Radio Emission in Wolf-Rayet Stars. *ApJ*, 705(1):899–906.

Nagata, T., Woodward, C. E., Shure, M., and Kobayashi, N. (1995). Object 17: Another Cluster of Emission-Line Stars Near the Galactic Center. *AJ*, 109:1676.

Najarro, F., Figer, D. F., Hillier, D. J., Geballe, T. R., and Kudritzki, R. P. (2009). Metallicity in the Galactic Center: The Quintuplet Cluster. *ApJ*, 691:1816–1827.

Najarro, F., Figer, D. F., Hillier, D. J., and Kudritzki, R. P. (2004). Metallicity in the Galactic Center: The Arches Cluster. *ApJ*, 611:L105–L108.

Najarro, F., Geballe, T. R., Figer, D. F., and de la Fuente, D. (2017). Emission Lines in the Near-infrared Spectra of the Infrared Quintuplet Stars in the Galactic Center. *ApJ*, 845:127.

Nandakumar, G., Schultheis, M., Feldmeier-Krause, A., Schödel, R., Neumayer, N., Matteucci, F., Ryde, N., Rojas-Arriagada, A., and Tej, A. (2018). Near-infrared spectroscopic observations of massive young stellar object candidates in the central molecular zone. *A&A*, 609:A109.

Nogueras-Lara, F., Gallego-Calvente, A. T., Dong, H., Gallego-Cano, E., Girard, J. H. V., Hilker, M., de Zeeuw, P. T., Feldmeier-Krause, A., Nishiyama, S., Najarro, F., Neumayer, N., and Schödel, R. (2018). GALACTICNUCLEUS: A high angular resolution JHK_s imaging survey of the Galactic centre. I. Methodology, performance, and near-infrared extinction towards the Galactic centre. *A&A*, 610:A83.

Nogueras-Lara, F., Schödel, R., Gallego-Calvente, A. T., Dong, H., Gallego-Cano, E., Shahzamanian, B., Girard, J. H. V., Nishiyama, S., Najarro, F., and Neumayer, N. (2019). GALACTICNUCLEUS: A high-angular-resolution JHK_s imaging survey of the Galactic centre. II. First data release of the catalogue and the most detailed CMDs of the GC. *A&A*, 631:A20.

Nogueras-Lara, F., Schödel, R., Neumayer, N., Gallego-Cano, E., Shahzamanian, B., Gallego-Calvente, A. T., and Najarro, F. (2020). GALACTICNUCLEUS: A high angular-resolution JHK_s imaging survey of the Galactic centre. III. Evidence for wavelength-dependence of the extinction curve in the near-infrared. *A&A*, 641:A141.

Panagia, N. and Felli, M. (1975). The spectrum of the free-free radiation from extended envelopes. *A&A*, 39:1–5.

Pastorelli, G., Marigo, P., Girardi, L., Aringer, B., Chen, Y., Rubele, S., Trabucchi, M., Bladh, S., Boyer, M. L., Bressan, A., Dalcanton, J. J., Groenewegen, M. A. T., Lebzelter, T., Mowlavi, N., Chubb, K. L., Cioni, M.-R. L., de Grijs, R., Ivanov, V. D., Nanni, A., van Loon, J. T., and Zaggia, S. (2020). Constraining the thermally pulsing asymptotic giant branch phase with resolved stellar populations in the Large Magellanic Cloud. *MNRAS*, 498(3):3283–3301.

Pastorelli, G., Marigo, P., Girardi, L., Chen, Y., Rubele, S., Trabucchi, M., Aringer, B., Bladh, S., Bressan, A., Montalbán, J., Boyer, M. L., Dalcanton, J. J., Eriksson, K., Groenewegen, M. A. T., Höfner, S., Lebzelter, T., Nanni, A., Rosenfield, P., Wood, P. R., and Cioni, M.-R. L. (2019a). Constraining the thermally pulsing asymptotic giant branch phase with resolved stellar populations in the Small Magellanic Cloud. *MNRAS*, 485(4):5666–5692.

Pastorelli, G., Marigo, P., Girardi, L., Chen, Y., Rubele, S., Trabucchi, M., Aringer, B., Bladh, S., Bressan, A., Montalbán, J., Boyer, M. L., Dalcanton, J. J., Eriksson, K., Groenewegen, M. A. T., Höfner, S., Lebzelter, T., Nanni, A., Rosenfield, P.,

Wood, P. R., and Cioni, M.-R. L. (2019b). Constraining the thermally pulsing asymptotic giant branch phase with resolved stellar populations in the Small Magellanic Cloud. *MNRAS*, 485(4):5666–5692.

Paumard, T., Genzel, R., Martins, F., Nayakshin, S., Beloborodov, A. M., Levin, Y., Trippe, S., Eisenhauer, F., Ott, T., Gillessen, S., Abuter, R., Cuadra, J., Alexander, T., and Sternberg, A. (2006). The Two Young Star Disks in the Central Parsec of the Galaxy: Properties, Dynamics, and Formation. *ApJ*, 643(2):1011–1035.

Paxton, B., Bildsten, L., Dotter, A., Herwig, F., Lesaffre, P., and Timmes, F. (2011a). Modules for Experiments in Stellar Astrophysics (MESA). *ApJS*, 192(1):3.

Paxton, B., Bildsten, L., Dotter, A., Herwig, F., Lesaffre, P., and Timmes, F. (2011b). Modules for Experiments in Stellar Astrophysics (MESA). *ApJS*, 192(1):3.

Paxton, B., Cantiello, M., Arras, P., Bildsten, L., Brown, E. F., Dotter, A., Mankovich, C., Montgomery, M. H., Stello, D., Timmes, F. X., and Townsend, R. (2013). Modules for Experiments in Stellar Astrophysics (MESA): Planets, Oscillations, Rotation, and Massive Stars. *ApJS*, 208(1):4.

Paxton, B., Marchant, P., Schwab, J., Bauer, E. B., Bildsten, L., Cantiello, M., Dessart, L., Farmer, R., Hu, H., Langer, N., Townsend, R. H. D., Townsley, D. M., and Timmes, F. X. (2015). Modules for Experiments in Stellar Astrophysics (MESA): Binaries, Pulsations, and Explosions. *ApJS*, 220(1):15.

Perley, R. A. and Butler, B. J. (2013). An Accurate Flux Density Scale from 1 to 50 GHz. *ApJS*, 204(2):19.

Rana, N. C. (1987). Mass function of stars in the solar neighbourhood. *A&A*, 184(1-2):104–118.

Reid, M. J., Schneps, M. H., Moran, J. M., Gwinn, C. R., Genzel, R., Downes, D., and Roennaeng, B. (1988). The Distance to the Center of the Galaxy: H 2O Maser Proper Motions in Sagittarius B2(N). *ApJ*, 330:809.

Rui, N. Z., Hosek, Matthew W., J., Lu, J. R., Clarkson, W. I., Anderson, J., Morris, M. R., and Ghez, A. M. (2019). The Quintuplet Cluster: Extended Structure and Tidal Radius. *ApJ*, 877(1):37.

Sana, H., Le Bouquin, J.-B., Lacour, S., Berger, J.-P., Duvert, G., Gauchet, L., Norris, B., Olofsson, J., Pickel, D., Zins, G., Absil, O., de Koter, A., Kratter, K., Schnurr, O., and Zinnecker, H. (2014). Southern Massive Stars at High Angular Resolution: Observational Campaign and Companion Detection. *ApJS*, 215:15.

Sanchez-Bermudez, J., Alberdi, A., Schödel, R., Brand ner, W., Galván-Madrid, R., Guirado, J. C., Herrero-Illana, R., Hummel, C. A., Marcaide, J. M., and Pérez-Torres, M. A. (2019). A VLBI study of the wind-wind collision region in the massive multiple HD 167971. *A&A*, 624:A55.

Schneider, F. (2014). *Statistical Analyses of Massive Stars and Stellar Populations*. PhD thesis, University of Bonn.

Schödel, R., Najarro, F., Muzic, K., and Eckart, A. (2010). Peering through the veil: near-infrared photometry and extinction for the Galactic nuclear star clus-ter. Accurate near infrared H, Ks, and L' photometry and the near-infrared extinction-law toward the central parsec of the Galaxy. *A&A*, 511:A18.

Scoville, N. Z., Stolovy, S. R., Rieke, M., Christopher, M., and Yusef-Zadeh, F. (2003). Hubble Space Telescope Paα and 1.9 Micron Imaging of Sagittarius A West. *ApJ*, 594:294–311.

Shahzamanian, B., Schödel, R., Nogueras-Lara, F., Dong, H., Gallego-Cano, E., Gallego-Calvente, A. T., and Gardini, A. (2019). First results from a large-scale proper motion study of the Galactic centre. *A&A*, 632:A116.

Stolte, A., Brandner, W., Grebel, E. K., Lenzen, R., and Lagrange, A.-M. (2005). The Arches Cluster: Evidence for a Truncated Mass Function? *ApJ*, 628(2):L113–L117.

Tang, J., Bressan, A., Rosenfield, P., Slemer, A., Marigo, P., Girardi, L., and Bianchi, L. (2014a). New PARSEC evolutionary tracks of massive stars at low metallic-ity: testing canonical stellar evolution in nearby star-forming dwarf galaxies. *MNRAS*, 445(4):4287–4305.

Tang, J., Bressan, A., Rosenfield, P., Slemer, A., Marigo, P., Girardi, L., and Bianchi, L. (2014b). New PARSEC evolutionary tracks of massive stars at low metallic-ity: testing canonical stellar evolution in nearby star-forming dwarf galaxies. *MNRAS*, 445:4287–4305.

Wright, A. E. and Barlow, M. J. (1975). The radio and infrared spectrum of early type stars undergoing mass loss. *MNRAS*, 170:41–51.

Yusef-Zadeh, F., Bushouse, H., Schödel, R., Wardle, M., Cotton, W., Roberts, D. A., Nogueras-Lara, F., and Gallego-Cano, E. (2015). Compact Radio Sources within 30' of Sgr A*: Proper Motions,Stellar Winds, and the Accretion Rate onto Sgr A*. *ApJ*, 809:10.

Yusef-Zadeh, F., Hewitt, J. W., Arendt, R. G., Whitney, B., Rieke, G., Wardle, M., Hinz, J. L., Stolovy, S., Lang, C. C., Burton, M. G., and Ramirez, S. (2009). Star Formation in the Central 400 pc of the Milky Way: Evidence for a Population of Massive Young Stellar Objects. *ApJ*, 702:178–225.

The silhouettes of the Y-shaped Very Large Array working hard against a gorgeous sunset in central New Mexico.
Credit: NRAO/AUI/NSF